ABSTRACT

Title of Dissertation:	CARBON MOLECULAR SIEVE HOLLOW FIBER MEMBRANE REACTORS FOR PROPANE DEHYDROGENATION
	Lu Liu, Doctor of Philosophy, 2023
Dissertation directed by:	Professor Chen Zhang, Department of Chemical and Biomolecular Engineering, University of Maryland College Park. Professor Dongxia Liu, Department of Chemical and Biomolecular Engineering, University of Delaware.

Propylene (C_3H_6) is a crucial petrochemical feedstock for a number of bulk chemicals and polymers. While steam cracking currently dominates C_3H_6 production, propane (C_3H_8) dehydrogenation (PDH) has been increasingly practiced addressing the gap between C_3H_6 demand and production. The C_3H_8 conversion of PDH reaction is challenged by thermodynamic limitation and catalyst deactivation at elevated reaction temperature. Membrane reactors can address both challenges and hence enhance the energy efficiency of PDH by achieving attractive and stable C_3H_8 conversion at low reaction temperature via selective removal of the hydrogen (H_2) product to shift the reaction equilibrium. Large-scale practice of PDH membrane reactors has not occurred due to the lack of scalable membranes that can provide attractive H_2/C_3H_8 separation performance at PDH conditions. Carbon molecular sieve (CMS) hollow fiber

membranes are a class of tunable and scalable inorganic membranes that are stable under non-oxidative high-temperature conditions, and therefore are potentially promising for PDH membrane reactors.

This PhD dissertation aims to investigate low-temperature propane dehydrogenation in novel membrane reactors comprising asymmetric CMS hollow fiber membranes. First, asymmetric polyimide-derived CMS hollow fiber membranes were fabricated and their high-temperature H_2/C_3H_8 performance was assessed. The roles of membrane pyrolysis temperature, permeation temperature, and feed composition on high-temperature H_2/C_3H_8 separation performance were systematically investigated. The effects of high-temperature H_2 and C_3H_6 exposure on CMS pore structure and transport properties were also examined. Under a continuous permeation test (~130 hours) of H_2/C_3H_8 feed mixture at 600 ºC, the asymmetric CMS hollow fiber membranes showed stable separation performance with outstanding H_2 permeance of 430 GPU and H_2/C_3H_8 separation factor of 511 exceeding those of microporous oxide membranes.

H_2-permeable CMS hollow fiber membrane reactors were created using the asymmetric CMS hollow fiber membranes and platinum-based catalysts. The effects of reactor operating conditions (i.e., reaction temperature, feed space velocity, sweep flow rate, C_3H_8 partial pressure, number of CMS hollow fibers) on PDH performance of the CMS hollow fiber membrane reactor were studied. Due to selective removal of H_2 product, the H_2-permeable CMS hollow fiber membrane reactor showed up to 300% higher C_3H_8 conversion than equilibrium conversion. Stable performance with commercially attractive C_3H_8 conversion (above 30%) and high C_3H_6 selectivity

(above 98%) were obtained in the CMS hollow fiber membrane reactor at 450 °C for over 110 hours. The CMS hollow fiber membrane reactors developed in this dissertation outperform PDH membrane reactors reported in literature by having higher conversion enhancement, lower reaction temperature, and the lowest deactivation rate.

These experimental results demonstrated the attractiveness of the novel CMS hollow fiber membrane reactors for energy efficient C_3H_6 production. One-dimensional isothermal models were further developed by material balance to understand the cooperative reaction and separation in the CMS hollow fiber membrane reactors. The modeling results of H_2-permeable CMS hollow fiber membrane reactor showed overall good agreement with experimental results. The models also demonstrated the viability of C_3H_6-permeable CMS hollow fiber membrane reactor and catalytic CMS hollow fiber membrane reactor, which provide valuable guidance to future development of CMS hollow fiber membrane reactors following this PhD research.

CARBON MOLECULAR SIEVE HOLLOW FIBER MEMBRANE REACTORS FOR PROPANE DEHYDROGENATION

by

Lu Liu

Dissertation submitted to the Faculty of the Graduate School of the
University of Maryland, College Park, in partial fulfillment
of the requirements for the degree of
Doctor of Philosophy
2023

Advisory Committee:
Professor Chen Zhang, Chair
Professor Dongxia Liu, Co-chair
Professor Kyu Yong Choi
Professor Juan Carlos Vega-Vila
Professor Mohamad Al-Sheikhly, Dean's Representative

Dedication

To my supporting and loving parents, Yangfang Chen and Hua Liu.

Acknowledgements

First and foremost, I would like to express my deepest appreciation to my advisors, Dr. Chen Zhang and Dr. Dongxia Liu. When I just entered graduate school, I knew little about membrane separation and catalytic reaction research. The completion of my dissertation would not have been possible without their unrelenting support. During the past five years, Dr. Zhang and Dr. Liu have given me numerous and valuable pieces of advice on designing experiments, solving research bottlenecks, writing scientific articles, and presenting at conferences. Their enthusiasm towards science, relentless dedication, and strong work ethic are the things I will continue to carry with me. I'd also like to extend my gratitude to my committee members: Dr. Mohamad Al-Sheikhly, Dr. Kyu Yong Choi, and Dr. Juan Carlos Vega-Vila for their valuable time and insightful suggestions. The funding support from NSF, DOE, and the Maryland Energy Innovation Institute is also greatly appreciated.

I am also grateful to all the help I received from Zhang and Liu's group members. I had the great pleasure of working with Gaurav Iyer and Ching-En Ku on membrane fabrication and characterizations. Many thanks to Dr. Ying Pan for teaching me all kinds of Swagelok connections, helping me with reaction system construction, and explaining to me the basic reactor operations. I would like to thank Antara Bhowmick for her valuable collaborations. I want to thank Dr. Junyan Zhang, Dr. Sichao Cheng and Zixiao Liu for their technical support in building lab-made furnaces, solving GC issues, and making quartz reactors. Special thanks to Dr. Emily Schulman and Dr. Wei Wu for showing me lab safety rules. I'd like to acknowledge the assistance

that I received from Dr. Jiancun Rao and Dr. Sz-Chian Liou for obtaining high quality SEM images.

I must also thank my parents and grandparents for their endless loving support. I very much appreciate my parents standing behind me when I decided to attend the graduate program in United States. They not only gave me the freedom to make life decisions but also taught me to take full responsibility for my own decisions. My grandparents, Xuqing Chen and Zhizhen Zhu, deserve lots of credit for keeping me feel unconditionally loved. Thanks should also go to my dear friends, Xiaodi Zhou and Yuyin Shi, who listened to me and encouraged me during the tough times I encountered in graduate school.

Table of Contents

List of Tables

List of Figures

List of Abbreviations

CMS - Carbon molecular sieve

PIM - Polymer of intrinsic microporosity

PBI - Polybenzimidazole

PDH - Propane dehydrogenation

FCC - Fluid catalytic cracking

SC - Steam cracking

CCR - Continuous catalyst regeneration

CVD - Chemical vapor deposition

PBR - Packed bed reactor

PBMR - Packed bed membrane reactor

CMR - Catalytic membrane reactor

SEM - Scanning electron microscopy

TGA - Thermogravimetric analysis

BET - Brunauer–Emmett–Teller

DFT - Density functional theory

NMP - N-Methyl-2-pyrrolidone

THF - Tetrahydrofuran

VTMS - Vinyltrimethoxysilane

Chapter 1: Introduction

1.1 Overview of propylene production

1.1.1 Propylene market

Propylene (C_3H_6) is the second-largest volume chemical produced after ethylene (C_2H_4) with annual global production exceeding 100 million tons.[1] C_3H_6 is the building block for a wide variety of industrial chemicals (**Figure 1.1**), including polypropylene, acrylonitrile, alcohols, propylene oxide, cumene, acrylic acid, etc.[2] The derivatives of C_3H_6 are used for manufacturing a broad range of consumer and industrial products such as plastics, resins, fibers, films, and rubber.[3] The global C_3H_6 market size was estimated at 104 billion dollars in 2022 and is expected to reach 150 billion dollars in 2032 with a compound annual growth rate of 3.76% between 2022 and 2023 (**Figure 1.2**).[4] The continuous growth of C_3H_6 market size is mainly driven by the increasing polypropylene demand worldwide since almost two-thirds of C_3H_6 is used to make polypropylene.[5] The expanding market of polypropylene is due to the increasing demand for lightweight polymers that are largely consumed by packaging, consumer goods, automotive, and construction industries.

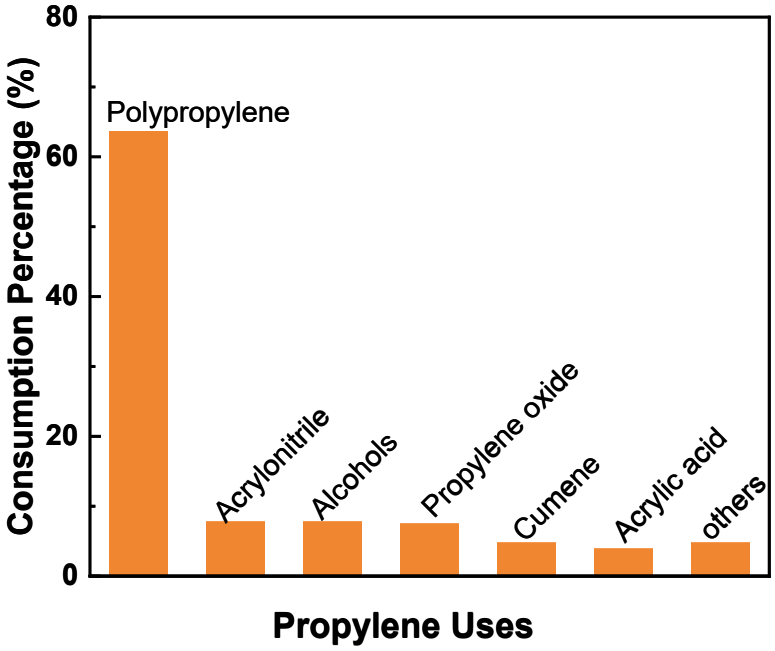

Figure 1.1. Global propylene consumption (2011) categorized by downstream chemical derivatives. (Alcohols include isopropanol, butanol, and 2-ethylhexanol.)[2]

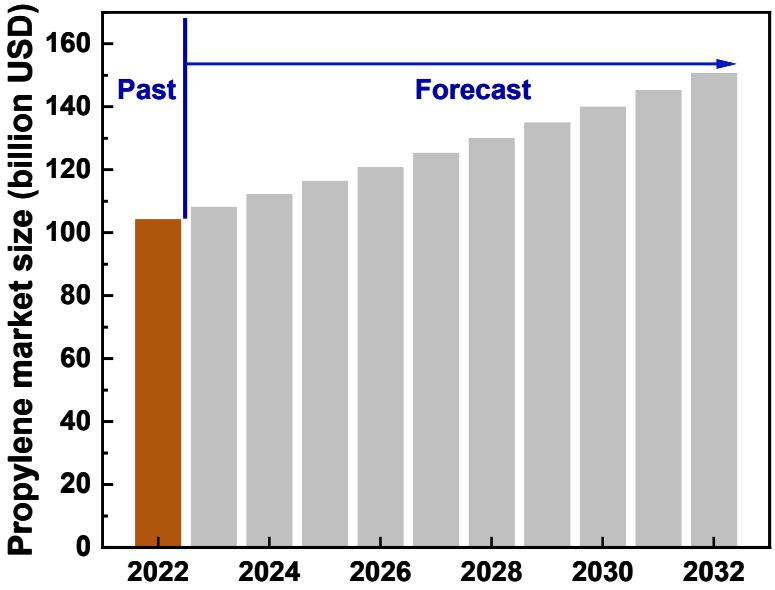

Figure 1.2. Global propylene market size estimation at 2022 with a forecast for 2023 to 2032.[4]

1.1.2 Propylene production processes

1.1.2.1 Conventional C_3H_6 production processes

C_3H_6 is traditionally produced either as a byproduct in steam crackers in C_2H_4 plants or as a coproduct from fluid catalytic cracking (FCC) units in petroleum refineries.[6] The traditional steam cracking (SC) and FCC processes account for 80% of the world C_3H_6 production (79 million tons in 2011). The steam cracking of hydrocarbons is the main industrial process for C_3H_6 production over the world. The SC process is performed in pipe furnaces (790–900°C) for short contacting time (0.1-0.5 s) with the existence of water vapor (30-80 wt%).[3] The SC units are developed for C_2H_4 production with C_3H_6 as a byproduct and the yield of C_3H_6 depends on the type of hydrocarbon raw materials (**Table 1.1**).[3]

FCC produces gasoline by upgrading low-value feedstocks with C_3H_6 as a coproduct.[7] During the FCC process, the hot catalysts are aerated with air at the bottom of a riser and then move upward to the reactor chamber. The vaporized feedstocks and fluidized catalysts enter the reactor simultaneously, where the cracking reaction takes place. The operating temperature of FCC is much lower than SC, where the temperature of the bottom riser is 550 ^oC and decreases to 500 ^oC on the top of the reactor. The C_3H_6 yield is 3~6 wt% depending on the operating conditions, feedstocks and type of catalysts used in the conventional FCC process.[7]

Table 1.1. C_3H_6 yield in steam cracking with respect to hydrocarbon raw materials.[3]

Raw materials	C_3H_6 yield (wt%)
Ethane	1.5
Propane	13.7
n-Butane	15.9
Naphtha	15.0
Straight-run gasoline	15.7
Gasoil	15.6

1.1.2.2 Propane dehydrogenation (PDH)

Since 2010, the growing gap between C_3H_6 market demand and the ability of traditional sources to produce C_3H_6 has been widening (**Figure 1.3**). On-purpose C_3H_6 production technologies have been rising to fill the gap including catalytic propane dehydrogenation (PDH), methanol to olefins (MTO), methanol to propylene (MTP), and olefins conversion technology (OCT).[8] Given the high selectivity to product C_3H_6 and the high abundance of cheap C_3H_8 from shale gas[9, 10], C_3H_8 dehydrogenation is the primary on-purpose technology in use. C_3H_8 dehydrogenation contributed to 22% of the C_3H_6 production in 2018 and the percentage is expected to grow to 32% in 2027.[8]

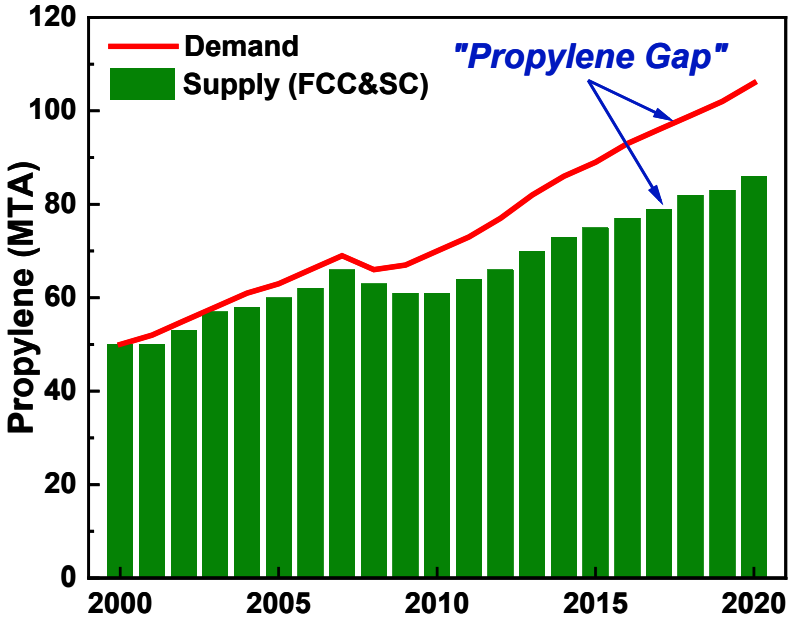

Figure 1.3. Globally growing propylene gap between conventional supply (SC and FCC) and demand. (MTA: Million Metric Tons Annually)[8]

C_3H_8 dehydrogenation converts C_3H_8 to C_3H_6 and hydrogen. The reaction is highly endothermic ($C_3H_8 \leftrightarrow C_3H_6 + H_2$, $\Delta H(298K)=124.3$ kJ/mol) and equilibrium limited, in which high temperatures and low pressures are favored (**Figure 1.4**). Typically, temperatures higher than 550 ^oC are required to reach attractive C_3H_6 yield (30-50%) in industrial processes. The high temperature favors side reactions, such as cracking and coke deposition, which not only hampers high C_3H_6 selectivity but also leads to catalyst deactivation. A regeneration step is usually required to keep the dehydrogenation process running continuously.

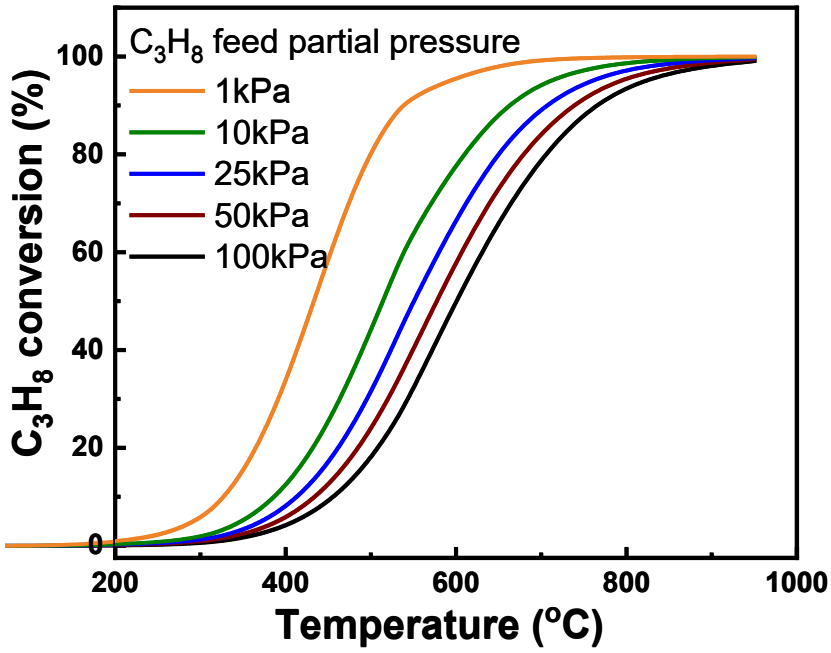

Figure 1.4. Propane equilibrium conversion as a function of reaction temperature at different feed propane partial pressures.

Two patented industrial C_3H_8 dehydrogenation processes, Catofin from CB&I Lummus and Oleflex from UOP, are currently in use for on-purpose C_3H_6 production.[11] The Catofin process, developed by Lummus Technology Company, converts C_3-C_5 paraffin to olefins by catalytic dehydrogenation. The reaction is carried out at temperatures ~560-650 °C and at pressures ~ 0.2-0.5 bar. The catalyst used in Catofin process is 18-20 wt % chromia−alumina (CrO_x/Al_2O_3) catalysts (lifetime ~2-3 years) with 1-2 wt % sodium (Na) or potassium (K) as promoters. The Catofin process typically involves 5-8 adiabatic fixed bed reactors with each reactor operating alternatively between dehydrogenation, regeneration, and purge steps. Each step lasts a few minutes with a full cycle of ~15-25 min and this continuous operation allows a constant production flow of C_3H_6.[12] The schematic representation of Catofin process is shown in **Figure 1.5 A**.[13]

The Oleflex process, developed by Honeywell UOP, is catalytic C_3H_8 dehydrogenation to produce C_3H_6 under fluidized bed reactors. The reaction runs at temperatures ~525-705 ºC and at pressures between 1-3 bar. The catalyst used in Oleflex is platinum-tin/alumina (Pt<1 wt %, 1−2 wt % Sn) with 0−1 wt % Na or K as promoters. The Oleflex process generally consists of 3-4 adiabatic radial flow reactors with catalyst loaded inside. These reactors are connected in series with preheater sit in between, where the preheaters provide the main heating source for the reaction system. The catalysts flow through the system during reaction and the last reactor is connected to the continuous catalyst regeneration (CCR) unit, where the catalysts are regenerated under chlorine-air atmosphere. The regenerated catalysts are sent back to the first reactor, completing a full cycle every 5-10 days.[12] The Oleflex process operates in a continuous mode to provide constant stream of product C_3H_6. The schematic of Oleflex installation is shown in **Figure 1.5 B**.[13] A detailed comparison between Catofin and Oleflex process is summarized in **Table 1.2**.

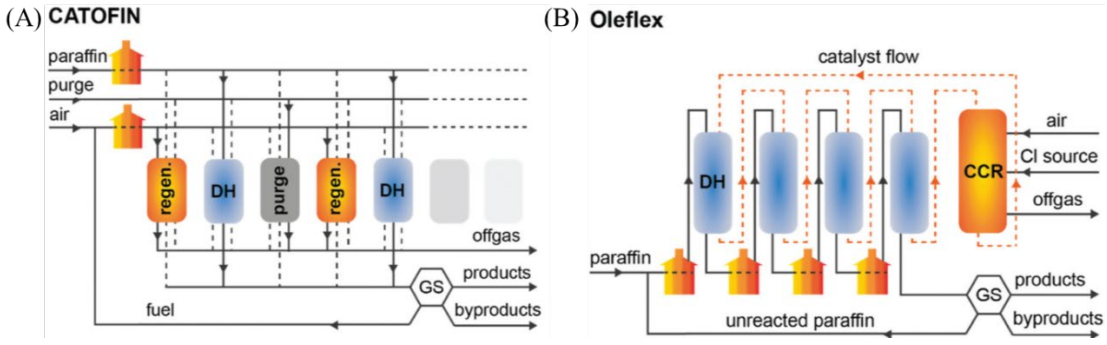

Figure 1.5. Schematic illustration of commercial PDH processes: (A) Catofin and (B) Oleflex. DH: dehydrogenation; GS: gas separation; CCR: continuous catalyst regenerator.[13]

Table 1.2. Summary of operation parameters of the Catofin and Oleflex processes.[11, 12]

Specifics	**Catofin**	**Oleflex**
License holder	CB&I Lummus	Honeywell UOP
Reactor type	Fixed bed reactor	Fluidized bed reactor
Catalyst	18−20 wt% CrO_x/Al_2O_3	<1 wt% Pt and 1−2 wt% Sn/Al_2O_3
T/°C	560-650	525−705
P/bar	0.2−0.5 bar	1−3 bar
WHSV/h^{-1}	<1	4-13
Operating period	15-25 min	5-10 days
Catalyst life/year	2-3	1-3
Conversion/%	40-45	30-40
Selectivity/%	82-87	85-88

1.2 Membrane reactors for propane dehydrogenation

1.2.1 Concept of membrane reactors

Although the PDH process has been successfully commercialized, improvements are still required to solve three major challenges in PDH technology: (1) high energy demand, (2) low single-pass conversion due to thermodynamics, and (3) rapid coking-induced catalyst deactivation. Membrane reactors can overcome the thermodynamic limit of PDH by in-situ H_2 removal, which provides increased C_3H_8 conversion, increased C_3H_6 yield, lower reaction temperatures, and higher energy efficiency. During reaction, product H_2 permeates through the membrane from the

reaction side to the sweep side. According to Le Chatelier's principle, the removal of H_2 shifts the reaction equilibrium toward C_3H_6 formation, achieving high C_3H_8 conversion at low reaction temperature (**Figure 1.6**). C_3H_8 conversion in a membrane reactor can potentially reach 100% at a mild temperature given the formed H_2 can be effectively removed from the reaction zone. The packed bed membrane reactor (PBMR) configuration has been most widely studied for PDH, which consists of C_3H_8 activation catalysts in a conventional packed bed reactor (PBR) and H_2-permeable tubular membranes surrounding the catalysts (**Figure 1.7**).

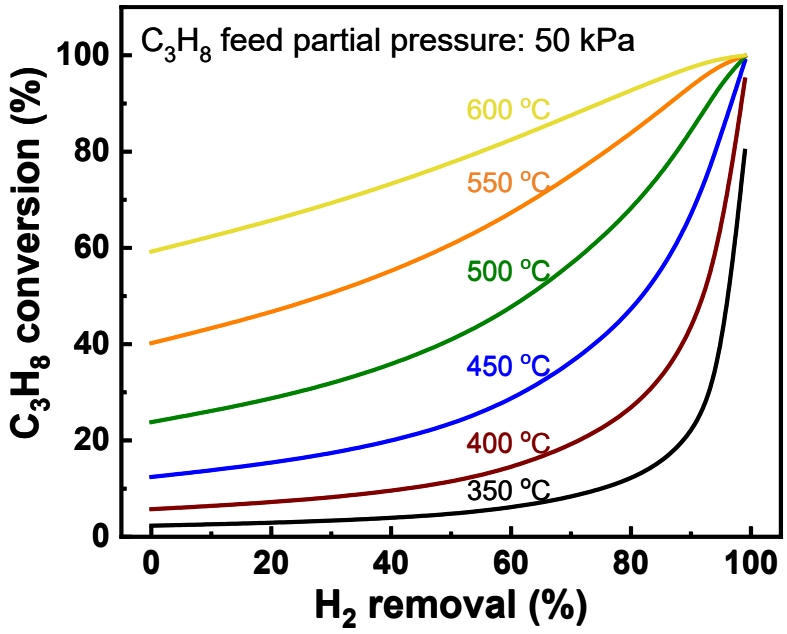

Figure 1.6. Propane conversion as a function of H_2 removal percentage at different temperatures (propane feed partial pressure is 50 kPa).

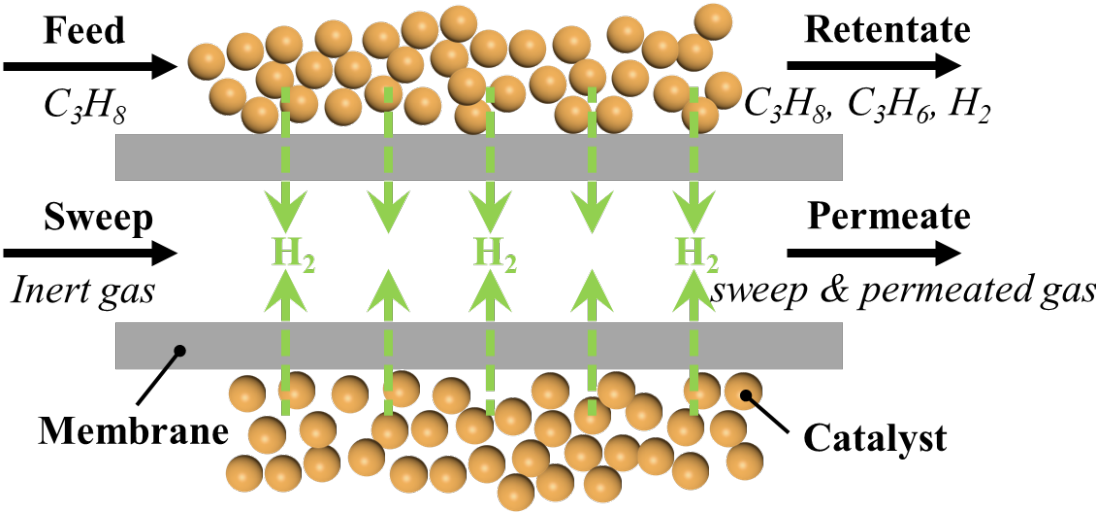

Figure 1.7. Schematic illustration of PBMR for PDH (cross-section view). The green arrows show H_2 permeation through the membrane surrounding the catalyst.

1.2.2 Membranes for PDH membrane reactor

The geometry of the membrane reactor is determined by the membrane format including disk, tubular, and hollow fiber. Notebly, tubular and hollow fiber membranes are often selected in membrane reactor studies because of their higher surface-to-volume ratio compared to disk-shaped membrane. The commercially available porous alumina or stainless-steel tubes have been widely used as the tubular membrane support materials. Hollow fiber membrane has the highest packing density and its thin separation layer enables high gas fluxes, which has attracted attention in recent membrane reactor studies.[14-16]

The membrane materials ideally are required to have high H_2 permeability, high H_2/C_3H_8 selectivity, and high-temperature stability. Given the PDH reaction temperature range, i.e.,400-650 ^oC, polymeric membranes are excluded due to their poor thermal and chemical stability. Inorganic membranes are considered as promising

candidates, where H_2-permeable membranes such as alumina, silica, zeolite, and palladium have been extensively investigated for PDH membrane reactors.[17-21]

1.2.2.1 Mesoporous alumina membrane

The pioneering work on PDH membrane reactors used mesoporous alumina as membrane materials.[18, 22, 23] The mesoporous alumina membranes were fabricated by sol-gel synthesis and deposited on a macroporous alumina tube. The gas separation in alumina membrane follows Knudsen diffusion mechanism. The mean free path of gas molecules is larger than the membrane pore size, leading to gas-wall collision dominated gas transport.[24] The selectivity of Knudsen diffusion is related to gas molecular weight

$$\alpha_{A/B} = \sqrt{M_A/M_B} \tag{1.1}$$

where $\alpha_{A/B}$ is the Knudsen selectivity of gas A over B, M_A and M_B is the molecular weight of gas A and B. The mesoporous alumina allows H_2 as well as reactant C_3H_8 and desired product C_3H_6 to to pass through the membrane. Indeed, Ziaka et al. reported their alumina membrane has high H_2 permeance ~7.6×10^4 GPU with low H_2/C_3H_8 selectivity ~3.7 at permeation temperature of 200 ºC.[23]

1.2.2.2 Microporous silica membrane

Microporous silica has been used as membrane materials in PDH membrane reactors for H_2 separation since 1996.[25-28] The microporous sillica membrane (pore size < 2 nm) can be prepared by sol-gel reaction or chemical vapor deposition (CVD). The sol-gel technique includes the synthesis of silica polymer sols, dip-coating of the substrate into the polymer sol, drying and finally calcination at high temperatures (e.g.

600 ºC) to get silica layers formed on the surface of the substrate. This process may be repeated several times to have the silica membrane with desired pore size.

Schafer et al. reported the silica membrane fabricated by sol-gel process had thin separation layers ~100 nm, giving H_2 permeance ~1.1×10^4 GPU with H_2/C_3H_8 selectivity ~55 at permeation temperature from 450-550 ºC.[27]. The CVD technique relies on the gas phase reaction between the precursor and oxidant. The silica precursor is supplied to the shell side of a tubular porous substrate while the oxidant is simultaneously supplied to the inner side of the substrate, where the amorphous silica is formed and deposited in the pores of the substrate. The CVD-derived silica membranes generally provide lower H_2 permeance but higher H_2/C_3H_8 selectivity than the sol-gel method. Ishii et al. reported CVD silica membranes had H_2 permeance ~746 GPU with H_2/C_3H_8 selectivity of 650 at 500 ºC.[26]

The gas transport mechanism in silica membranes with sub-nm pore size can be described using either solution-diffusion or modified gas-translation model.[29] The solution-diffusion model assumes that the silica membrane (i.e., selective layer) is nonporous where the gas molecules first adsorb into the membrane on upstream, then diffuse through the membrane under chemical potential gradient, and finally desorb on the downstream of the membrane. By comparison, the gas-translation model assumes rigid and cylindrical pores in silica membrane and gas molecules follow a molecular-diffusion pattern.

1.2.2.3 Microporous zeolite membrane

Three zeolites, i.e., silicoaluminophosphate (SAPO-34), Mobil-type five (MFI) and Linde type A (LTA), have been studied in PDH membrane reactors since 2016.[14,

16, 19, 20, 30] The structure of each zeolite is shown in **Figure 1.8**.[31] The zeolite membrane is typically synthesized using a seeded secondary growth method. Take SAPO-34 zeolite membrane fabrication as an example, the SAPO-34 seed nanoparticles are first synthesized, the seeds are then deposited on the surface of a porous tubular substrate by rub-coating or dip-coating, the seeded substrate is placed in autoclave with synthesis gel filled close to the top of the substrate, and the zeolite membrane is formed after the hydrothermal reaction.

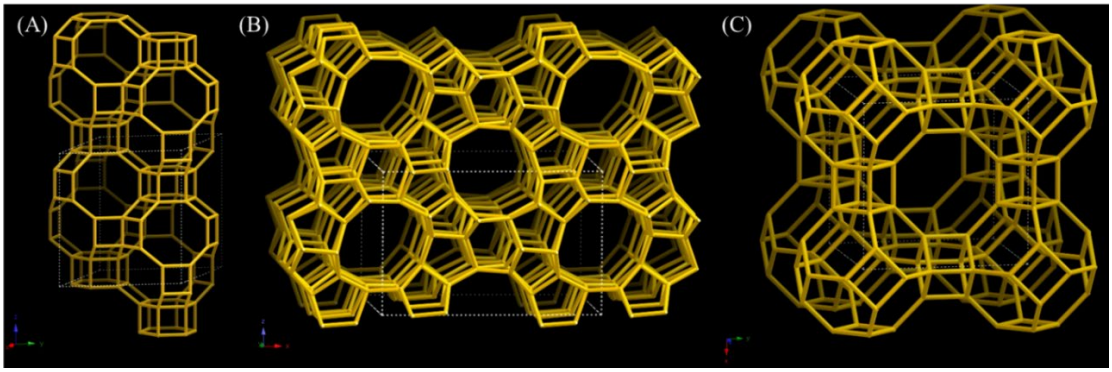

Figure 1.8. Zeolite structure of (A) SAPO-34 [001], (B) MFI [010], and (C) LTA [100].[31]

In comparison to amorphous silica membrane with pore size distribution, zeolite membrane has crystalline structure with uniform pore size. The gas permeation through zeolite membranes is considered as adsorption on the external surface, selective adsorption in zeolite pores, and size-depending diffusion through zeolite pores. The dominance of either molecular-sieving, diffusion, or adsorption is not clearly given.[32] SAPO-34 zeolite with a pore diameter of 0.38 nm provides effective H_2 (kinetic diameter 0.29 nm) separation over hydrocarbons (L-J diameter C_3H_6 0.47 nm, C_3H_8 0.51 nm). Kim et al. synthesized SAPO-34 membranes with thin separation layer ~ 1 μm, providing H_2 permeance of 686 GPU and H_2/C_3H_8 selectivity of 27 at

650 °C.[19] The MFI zeolite with a medium-pore size of 0.55 nm is typically used for xylene isomers separation.[33, 34] Kim et al. reported H_2 permeance of 537 GPU and H_2/C_3H_8 selectivity of 8 (lower than SAPO-34 due to the larger pore size) in MFI zeolite membrane at 600 °C.[19] The LTA zeolite with a pore size ~0.4 nm has been used as a protective layer for palladium (Pd) membrane in PDH membrane reactors.[14] The presence of nanoporous LTA zeolite on top of Pd membranes reduces the poisoning of Pd from hydrocarbons and offers better Pd membrane stability during PDH conditions. The Pd-LTA membrane showed stable H_2 flux (0.23 mol/m^2/s) with high purity (≥99.9%) of permeated H_2 during 72-hour permeation at 600 °C with the presence of 10% C_3H_8 and C_3H_6.

1.2.2.4 Dense palladium-based metal membrane

Pd and Pd-alloy membranes have been studied for PDH membrane reactors since 1996.[25] A variety of methods are employed for Pd or Pd-alloy membranes fabrication including electroless plating (ELP), chemical vapor deposition (CVD), electrodeposition (ELD), etc.[35] ELP is the most common method for coating Pd or Pd-alloy on porous ceramic substrate, where the metallic films are plated on the substrate surface by the reduction of metallic salt complexes with the presence of reducing agents without applying external electric field.[35]

Pd-based membranes have been extensively used in hydrogenation and dehydrogenation reactions [15, 36, 37] due to their high H_2 permeability and extremely high H_2 selectivity, which allows effective H_2 removal during reactions and enables high purity H_2 production in permeate side. Collins et al. reported Pd membrane had H_2 permeance of 7100 GPU and H_2/N_2 selectivity 1920 at permeation temperature of

450 °C.[25] Pd-alloy membranes are also widely used in PDH membrane reactors because the presence of a second metal (e.g., Ag, Cu, Ru, Fe, etc.) can prevent Pd phase transition problem and alleviate the H_2 embrittlement and unsaturated hydrocarbon or impurity poisoning issues.[38, 39] Weyten et al. reported a commercial Pd-Ag (20-25 wt% Ag) alloy membrane had H_2 permeance ~1692 GPU and H_2/Ar selectivity of 4410 at 500 °C.[40]

The H_2 permeation through Pd membranes follows the sorption-diffusion mechanism. The steps for H_2 transport through Pd membrane under pressure difference include (a) external diffusion of molecular H_2 to Pd surface on the upstream, (b) reversible H_2 dissociative adsorption on Pd surface, (c) dissolution of atomic H into the bulk Pd metal, (d) association of H atom on Pd surface, (e) desorption of molecular H_2 from Pd surface, and (f) diffusion of molecular H_2 away from Pd surface on the downstream. The H_2 permeability P_{H_2} of Pd is defined as

$$P_{H_2} = \frac{J_{H_2}}{l\left(p_{H_2,f}^{n} - p_{H_2,s}^{n}\right)} \tag{1.2}$$

where J_{H_2} is H_2 flux, l is the thickness of Pd layer, $p_{H_2,f}$ and $p_{H_2,s}$ are the H_2 partial pressures on the feed and permeate sides, respectively. The pressure exponent n varies from 0.5 to 1, depending on the rate controlling step. According to Sievert's law, when the rate determining step is the bulk diffusion through Pd (step c), n equals 0.5.[41] The value of n is greater than 0.5 when the Pd layer has defects or pinholes where a substantial portion of H_2 could pass through.

1.2.3 Catalysts for non-oxidative PDH reaction

1.2.3.1 Pt-based catalysts

Platinum (Pt)-based catalysts are commonly used for PDH since Pt is highly active in paraffinic C-H bonds scissions.[11, 12] The reaction mechanism of PDH on Pt-based catalysts is illustrated in **Figure 1.9-1.10**.[12, 42] C_3H_8 first weakly physisorbs on Pt surface sites with adsorption energy E_{ad} ranging from -0.4 eV to -0.2 eV. C_3H_6 is formed after the first and second C-H bond scissions of physisorbed C_3H_8 on the Pt sites, where E_1 and E_2 are activation barriers of each step. The as-produced C_3H_6 still chemsorbs on the Pt sites with a typical desorption energy E_{de} of -0.4 eV to -1.0 eV. However, the chemsorbed C_3H_6 could undergo a third C-H bond scission to produce C_3H_5 followed by deep dehydrogenation, cracking, and finally coke formation. The activation energy difference ($\Delta E=E_{de}-E_3$) between C_3H_6 desorption and the third C-H bond scission becomes the key determinant for C_3H_6 selectivity and catalyst stability, which is hightly dependent on the Pt geometric and electronic features.[43, 44] In addition, high temperature during PDH reaction could induce severe sintering of Pt nanoparticles, leading to reduction in catalyst activity.

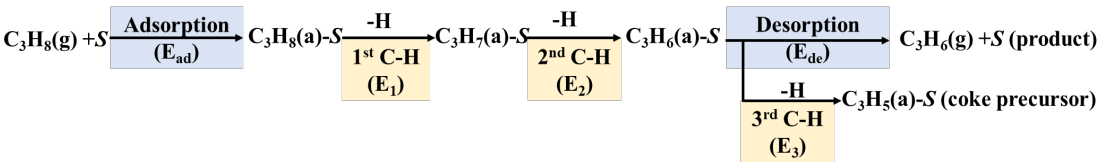

Figure 1.9. Reaction mechanism of PDH. (S represents Pt surface sites)[42]

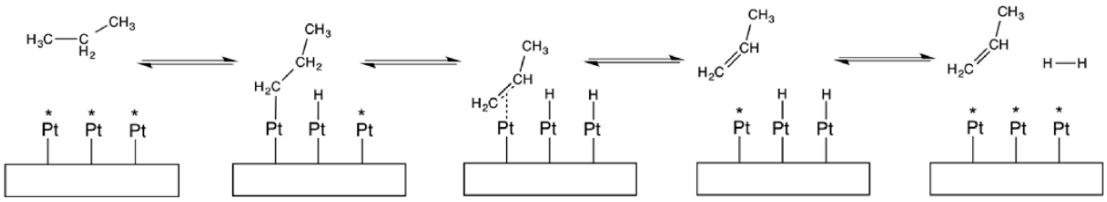

Figure 1.10. Schematic representation of PDH reaction pathways on surface Pt atoms.[12]

The effects of promoters and support have been widely explored to modify the characteristics of Pt-based catalysts.[11, 42] The addition of metal promoters (e.g. Sn, Zn, Cu, Fe, etc.) to Pt is an efficient way to enhance the catalyst activity and selectivity as well as lower down catalyst costs by reducing the Pt loading.[45, 46] Meanwhile, the textural properties of catalyst support, such as specific surface area, acid-base properties, and thermal stability, have been proved to have significant influences on Pt-based catalyst performance. Among various types of support material (e.g., Al_2O_3, SiO_2, $MgAl_2O_4$, zeolite, etc.)[47-50], Al_2O_3 is the most widely employed support because of its large surface area, strong mechanical strength, high thermal conductivity, excellent thermal stability, and competitive price.

1.2.3.2 Metal oxide-based catalysts

Metal oxide-based catalysts are also used for PDH reaction since the Lewis acid M-O sites can effectively activate the C-H bonds of C_3H_8. A variety of bulk or supported metal oxide catalysts have been investigated for PDH including chromium oxide (CrO_x), vanadium oxide (VO_x), and gallium oxide (GaO_x).[42, 49, 51-54] Although showing considerable activity and C_3H_6 selectivity in PDH, the metal oxide catalysts suffer from rapid deactivation and require frequent regeneration operations. Notably, the loss of catalyst activity due to regeneration sintering is not completely reversible.

For CrO_x-based catalysts, the PDH reaction occurs at the Cr-O sites. The reaction and deactivation mechanism of CrO_x on PDH are complex since a series of chromium ions with different valence states (Cr^{6+}, Cr^{5+}, Cr^{3+}, and Cr^{2+}) all play roles during the PDH reaction process. Sun et al. performed DFT calculations to reveal the active site center of CrO_x/SiO_2 catalysts. The PDH reaction pathways at Cr^{6+}, Cr^{5+}, and Cr^{3+} were examined and compared, where Cr^{3+} exhibited a relatively better reactivity than the other two valence states.[51] Indeed, Sattler et al. found the reduction of Cr^{6+} to Cr^{3+} at the beginning of PDH reaction using in situ X-ray absorption near edge structure (XANES) and UV-vis spectra, and Cr^{3+} was generally considered as the active site.[52] **Figure 1.11** shows a simplified reaction mechanism of Cr^{3+} species catalyzing the PDH reaction.[12]

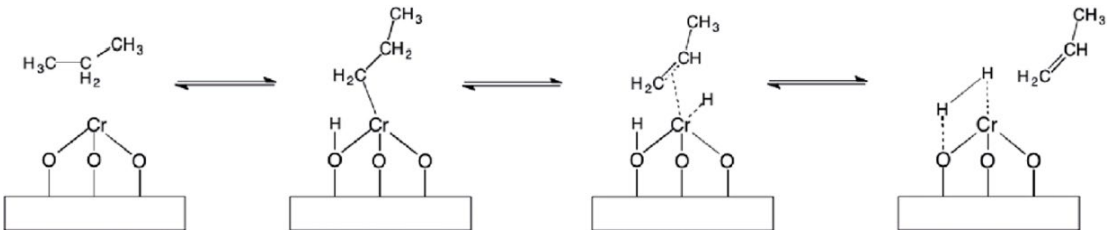

Figure 1.11. Schematic representation of PDH reaction pathways on the surface of coordinatively unsaturated Cr^{3+} species.[12]

As for VO_x-based catalysts, Liu et al. identified V^{3+} as the most active sites in PDH reaction among the V^{5+}, V^{4+} and V^{3+} ions.[53] The C_3H_8 activation and selective C_3H_6 production specific pathways are still unclear since a variety of V species (V^{5+}, V^{4+}, V^{3+}, isolated V, oligomeric V^{n+}, and crystalline V_2O_5) coexist in VO_x-based catalysts. A comparison was made between VO_x, CrO_x, and PtSn catalysts for PDH reaction, where VO_x showed better C_3H_6 selectivity and catalyst stability in continuous

regeneration cycles.[54] However, the toxicity of VO_x impedes their industrial application for PDH.

The GaO_x-based catalysts have been investigated for PDH for years. The active sites of Ga are still in debate, which are strongly affected by the support materials, synthesis methods and Ga loading amounts. Studies by Zheng and coworkers showed that β-Ga_2O_3 is the most stable polymorph and the Lewis acid sites provided by coordinatively unsaturated Ga^{3+} are the active sites for PDH reaction.[55] The activation of C_3H_8 on the surface of Ga_2O_3 starts from losing the first H atom of C_3H_8 molecule to form a propyl group and a hydroxyl group followed by the removal of β-H to form another hydroxyl group. Notably, the process of converting two hydroxyl groups to H_2O or H_2 requires high energy, and thus the desorption step of chemisorbed H_2 limits the Ga_2O_3 catalyst activity.[56] Furthermore, GaO_x-based catalysts typically show severe sintering during continuous regeneration cycles, where a desirable regeneration protocol needs to be developed to recover the catalyst reaction performance.[57]

1.2.4 PDH membrane reactors

1.2.4.1 Alumina membrane reactor

Inspired by the attractive benefits of membrane reactors, research efforts have been made on PDH membrane reactors since 1990s. Bitter and coworkers first studied PDH membrane reactor in 1986 using mesoporous Al_2O_3 membranes and Cr_2O_3/Al_2O_3 catalysts. The results showed C_3H_8 conversion of 59% with C_3H_6 selectivity of 90% were achieved in the membrane reactor at 575 ^oC, allowing 46% conversion enhancement compared with traditional packed bed reactor.[18] Later in 1993, Tsotsis

et al. reported PDH membrane reactors comprised of multi-layered mesoporous alumina membranes and Pt-Mg/γ-Al_2O_3 catalysts.[22] At 480 ºC, the membrane reactor provided 100% C_3H_8 conversion enhancement and 10% C_3H_6 selectivity improvement compared to conventional reactor. After the first few trials on alumina membrane for PDH membrane reactor, the porous alumina is more widely used as membrane support for exploring other types of PDH membrane reactors.

1.2.4.2 Silica membrane reactor

The first silica membrane reactor for PDH was reported by Collins and co-workers in 1996. The membrane reactor comprised of alumina-supported silica membranes and commercial Pt/aluminosilicate catalysts.[21] At 550 ºC, the C_3H_8 conversion of 40% and C_3H_6 selectivity of 90% was achieved in the membrane reactor, showing a 34% conversion improvement compared with packed bed reactor. The reaction performance was continuously recorded for 8 hours, where the C_3H_8 conversion decreased from 40% to 32%, showing the membrane reactor deactivation problem caused by catalyst coking. In 1997, Weyten et al. studied the PDH membrane reactor using tubular silica membrane and commercial Cr_2O_3/Al_2O_3 catalyst.[28] Notably, the membrane reactor showed stable C_3H_8 conversion of 24% (34% higher than equilibrium conversion) with C_3H_6 selectivity of 89% at 500 ºC for ~10 hours. The reaction performance was monitored for ~95 hours, where the C_3H_8 conversion started dropping after the first 10 hours and finally decreased to 5% due to the catalyst deactivation. Later in 2003, Schäfer et al. compared the silica membrane reactor performance by using different commercial PDH catalyst, i.e., Cr_2O_3/Al_2O_3 and Pt–Sn/Al_2O_3.[27] For both catalysts, faster deactivation rate was observed in membrane

reactors. For the membrane reactor with Pt–Sn/Al_2O_3 catalyst, the C_3H_8 hydrogenolysis to CH_4 and C_2 species is reduced due to the removal of H_2 by membrane in feed side, which compensates C_3H_6 selectivity drop in the membrane reactor caused by strong coking. This study suggests that coking-resistant catalysts at extended reaction time need to be developed for achieving stable membrane reactor performance.

1.2.4.3 Zeolite membrane reactor

Zeolite-based membrane reactors for PDH have not been investigated until 2016 by the Nair group. Although zeolite membranes have been widely investigated for H_2 purification [58, 59], currently five published papers discussd the zeolite membrane reactor performance for PDH [14, 16, 19, 20, 30]. The SAPO-34 zeolite membranes with Na_2O-doped Cr_2O_3/Al_2O_3 catalysts were first studied for PDH reaction. The membrane reactor achieved C_3H_8 conversion of 70% with C_3H_6 selectivity of 85% at 600 °C, giving ~58% conversion enhancement and ~35% selectivity improvement compared with packed bed reactor.[19] In the same year, Nair and coworkers developed catalytic membrane reactors (CMR) for PDH by applying MFI zeolite-Pt catalytic membranes, which eliminates the packed catalyst in previously reported PDH membrane reactors. The CMR for PDH was tested at 600 °C for 12 hours, showing stable C_3H_8 conversion of 14% with C_3H_6 selectivity of 33%. Despite the low conversion and selectivity, this work proved that the encapsulation of Pt nanoclusters in zeolite framework provides better Pt thermal stabilization and thus reduces the catalyst deactivation in PDH membrane reactor.[20] In 2021, Dangwal et al. tested PDH in a high-pressure zeolite membrane reactor. The silicalite membrane was coated on α-Al_2O_3 disk with Pt/Al_2O_3 catalyst evenly spreading over the membrane surface.

The highest C_3H_8 conversion achieved in the membrane reactor was 49% with C_3H_6 selectivity of 97% at 600 ºC and 5 atm reaction pressure. Compared to packed bed reactor, a 145% conversion enhancement and 22% selectivity improvement were observed in the membrane reactor. The principle behind the increased reaction pressure is that H_2 permeation rate increases under higher feed pressure, leading to considerable C_3H_8 conversion improvements due to fast H_2 removal rate.[30]

1.2.4.4 Pd-based membrane reactor

Dense palladium (Pd)-based membranes have been extensively studied for PDH membrane reactors due to the high H_2 permeability and selectivity of Pd membrane. The pioneering work on Pd-based membrane reactor for PDH was conducted by Gryaznov and co-worker in 1996.[17] Pd-Ru or Pd-Ag alloy tubes and supported Pt catalysts were used for the PDH reaction tests. C_3H_6 yield up to 70% was obtained in Pd-Ru membrane reactor at 550 °C compared with equilibrium yield of 32%. The Pd-Ag membrane reactor was tested at 525°C with C_3H_6 yield declining from 40% to 20% in 16 hours. The Pd-alloy tubes had wall thickness ranging from 75 μm to 250 μm.

Thinner and defect-free membrane separation layer is preferred as much higher H_2 flux can be achieved. In 1997, Yildirim et al. applied thin Pd-Ag composite membranes in PDH membrane reactor. The continuous Pd-Ag metallic layer was deposited on the surface of Vycor glass tube, giving a pinhole-free metal layer ~ 4 μm. With the dense Pd-Ag composite membranes and Pt/Al_2O_3 catalyst, the membrane reactor was tested for PDH at 400 ºC. The results showed 21% C_3H_8 conversion, corresponding to four-fold improvement on equilibrium conversion.[60]

In addition to porous tubular support, Wu et al. applied asymmetric alumina hollow fiber as the Pd-based membrane substrate. Unlike other existing Pd-Ag composite membranes, where an intermediate layer (e.g. γ-Al_2O_3) is often applied to bridge the porous substrate surface and the dense Pd/Ag layer, the Pd-Ag layer was directly coated on the outer smooth surface of the asymmetric hollow fiber substrate. A highly compact catalytic hollow fiber membrane reactor was developed in this work by loading Pt/γ-Al_2O_3 catalysts into the finger-like voids of the hollow fiber substrate. The membrane reactor was examined for PDH at 450 ^oC, showing an initial C_3H_8 conversion of 42% at 5 min and final conversion of 6% at 45 min.[15]

Considering the severe deactivation of Pd-based membrane reactor, Pati et al. reported using LTA zeolite as the protective layer for Pd-based membranes during PDH reaction. The Pd membrane was coated on the inner side of the α-Al_2O_3 hollow fiber substrate with LTA zeolite deposited on the outside of the hollow fiber. The PDH membrane reactor was tested at 600 ^oC using the triple-layered membrane (Pd/α-Al_2O_3/LTA zeolite) and Cr/Al_2O_3 catalyst, showing initial C_3H_8 conversion of 48% (15% higher than packed bed reactor) with C_3H_6 selectivity of 92%. The membrane reactor reaction performance was recorded continuously for 5 hours, where the conversion decreased from 48% to 33%. Despite the presence of LTA zeolite decreased the Pd membrane poisoning issue by hydrocarbons, deactivation was still observed in Pd membrane reactor for PDH.[14]

1.2.4.5 Challenges in PDH membrane reactor

Despite substantial efforts made on PDH membrane reactors, their industry implementation is not achieved given the presence of two major challenges. First,

catalysts and membranes experience accelerated coking and deactivation due to H_2 depletion. Second, inorganic or metallic membranes are costly to fabricate at a large scale and are often limited to flat-sheet or tubular membrane geometry with low to moderate membrane packing efficiency. To date, achieving high C_3H_8 conversion, high C_3H_6 yield, high catalyst durability, and low energy consumption in PDH membrane reactors remains as a challenge.

1.3 Carbon molecular sieve (CMS) membranes

1.3.1 Applications of CMS membranes

Carbon molecular sieve (CMS) is a type of high-performance porous carbon-based membrane prepared by pyrolyzing polymeric precursors. The unique combination of highly permeable micropores and molecular sieving ultramicropores allow CMS membranes to have high productivity and high separation efficiency, exceeding those of polymer membranes[61] and competitive with many inorganic membranes[62-64]. The separation performance of CMS membranes can be affected by preparation parameters and polymer precursor properties. Owing to their good tunability, CMS membrane have shown attractive separation performance for many economically important gas[65], vapor[66, 67], and organic solvent separations[68]. Recent advances of three industrially important gas separations, i.e., CO_2/CH_4, olefin/paraffin, and H_2/CO_2 separation by CMS membranes are reviewed below.

1.3.1.1 CO_2/CH_4 separation

The separation of CO_2/CH_4 has received extensive attention due to its significance in natural gas purification and CH_4 recovery from landfill gas.[69]

Although polymeric membranes have been widely adopted for CO_2/CH_4 separation for decades, they suffer from aging as well as severe plasticization by condensable CO_2 molecules.[70] The separation performance of polymer membranes is also limited by the trade-off between permeability and selectivity, known as polymer upper bound. CMS membranes are considered as attractive alternatives for CO_2/CH_4 separation due to their outstanding separation performance and stability.

Zhang and Koros reported the CO_2/CH_4 separation performance of CMS membranes derived from commercially available Matrimid polyimide.[71] The CMS pyrolyzed at 900 ^oC showed extremely high CO_2/CH_4 permselectivity of 3650 with CO_2 permeability of ~25 Barrer under 35 ^oC permeation at 100 psia upstream pressure. The CO_2/CH_4 separation performance of CMS membranes derived from various polyimide precursors was presented in **Figure 1.12**, surpassing 2008 Robeson's polymer upper bound for CO_2/CH_4. A recent publication by Liu et al. reported a new type of CMS membrane derived from crystalline porous hydrogen-bonded organic frameworks (HOF) for CO_2/CH_4 separation.[70] The CMS membrane pyrolyzed at 600 ^oC provided high CO_2 permeability of 157 Barrer with CO_2/CH_4 separation factor of 128 under 50%CO_2/50%CH_4 feed mixture at 25 ^oC and 20 psig. The CMS membrane also showed good stability at different temperatures and pressures as well as strong resistance to physical aging.

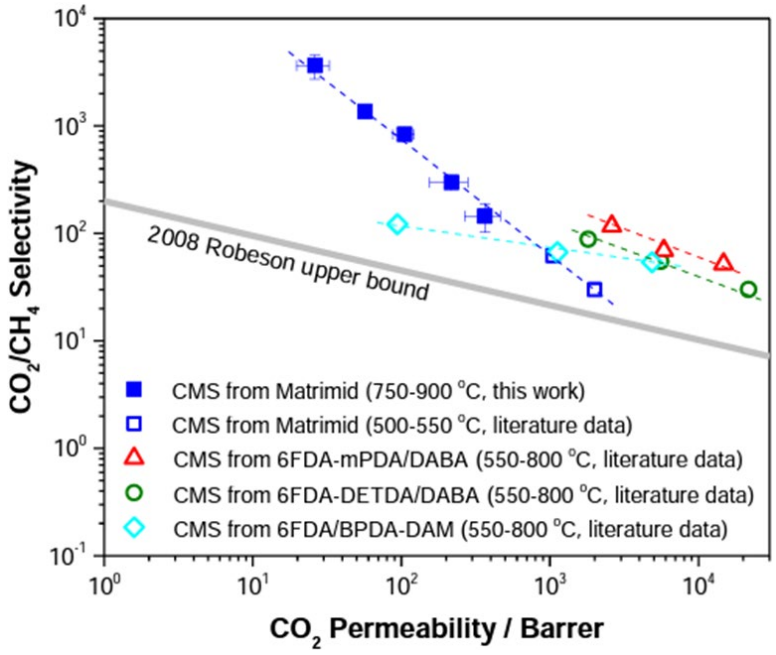

Figure 1.12. CO_2/CH_4 separation performance of CMS membranes derived from different polyimide precursors (single-gas permeation, 35 °C).[71]

1.3.1.2 olefin/paraffin separation

The olefin/paraffin separation in petrochemical industry is currently performed by energy-intensive cryogenic distillation at high pressure.[72] The similar boiling points of olefins and paraffins (C_2H_6 (−88.5 °C), C_2H_4 (−102.4 °C); C_3H_8 (−42.2 °C), C_3H_6 (−47.7 °C)) make them hard to separate, which requires harsh operating conditions with 150–200 trays and high reflux ratios.[73] The similar olefin/paraffin molecular sizes (C_2H_6 4.1 Å, C_2H_4 3.7 Å; C_3H_8 4.3 Å, C_3H_6 4.0 Å) place great challenges on membrane-based separation technologies. CMS membranes have been studied for olefin/paraffin separations due to their impressive permselectivity.[72-76] The rigid CMS pore structure also prevents membrane deterioration and deformation from hydrocarbons. Compared to other inorganic membranes (e.g., zeolite, silica, zeolitic imidazolate frameworks, etc.) for olefin/paraffin separation, CMS membranes

showed attractive separation performance (**Figure 1.13**) with much lower production cost and easier fabrication process.[73]

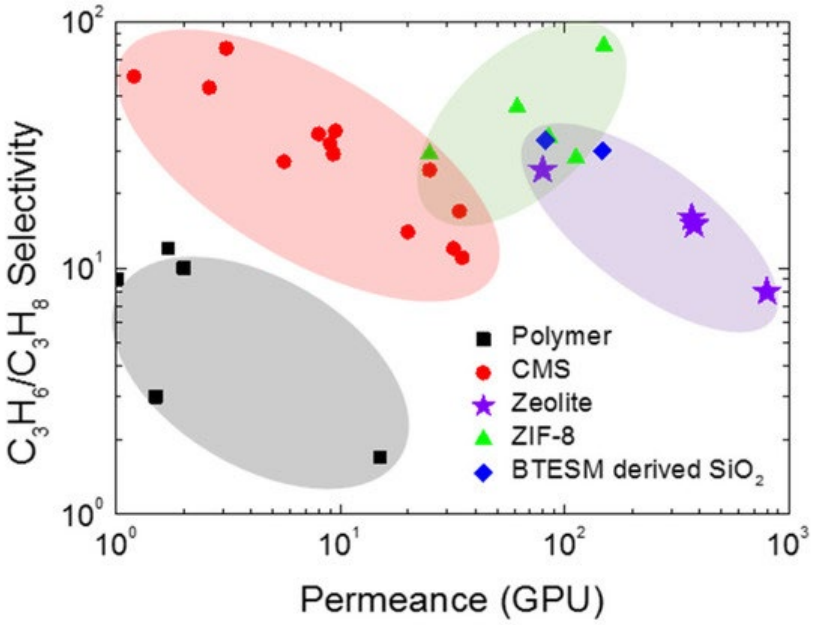

Figure 1.13. Comparison of C_3H_6/C_3H_8 separation performance in polymeric membranes and inorganic membranes.[73]

Hazazi et al. reported the C_2H_4/C_2H_6 separation performance in triptycene-derived CMS membranes.[76] By pyrolyzing the shape-persistent triptycene-based ladder polymer of intrinsic microporosity (PIM) at 900 °C, the CMS membranes showed precise molecular sieving behavior with C_2H_4/C_2H_6 separation factor of 96 and C_2H_4 permeability of 2 Barrer at 35 °C and 10 bar feed pressure (**Figure 1.14**). The long-term stability of ladder PIM-derived CMS membranes was demonstrated under equimolar C_2H_4/C_2H_6 feed mixture at varying pressures (10-20 bar), where the mixed-gas selectivity dropped from 100 to 57 after continuous 70 days permeation. Du et al. investigated the olefin/paraffin separation performance using polydopamine(PDA)-derived CMS membranes.[75] The CMS pyrolyzed at 800 °C (PDA-C800) and 900 °C

(PDA-C900) showed narrow pore size range of 4.1-4.3 Å and 3.7-4.0 Å, respectively. The PDA-C800 provided a high C_3H_6 uptake of 1.98 mmol/g with C_3H_6/C_3H_8 uptake ratio of 37 while PDA-C900 showed a high C_2H_4 uptake of 2.25 mmol/g with C_2H_4/C_2H_6 uptake ratio of 25 at 1 bar and 298 K. Their work indicated that the CMS pore structure can be finely tuned to provide precise molecular sieving of C_2H_4/C_2H_6 and C_3H_6/C_3H_8 relying on size-exclusion effects.

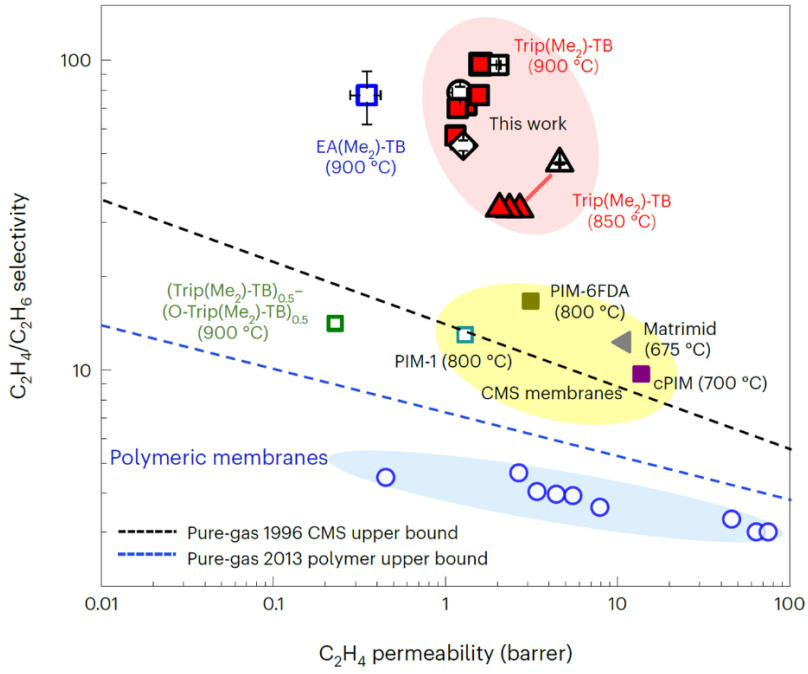

Figure 1.14. Comparison on C_2H_4/C_2H_6 separation properties of state-of-art CMS membranes derived from various polymer precursors.[76]

1.3.1.3 H_2/CO_2 separation

The recovery of H_2 and capture of CO_2 are important steps for the sustainable production of blue H_2 from steam CH_4 reforming process.[77] CO_2 is more condensable and has higher solubility than H_2 (critical temperature: CO_2 304 K, H_2 30 K) while H_2 has higher diffusivity than CO_2 (kinetic diameter: CO_2 3.3 Å , H_2 2.89 Å). Therefore, the membrane materials need to have strong molecular-sieving ability between 2.89

and 3.3 Å to maximize the H_2/CO_2 selectivity and to have enough free volumes to allow high H_2 productivity. CMS membranes derived from various polymer precursors have been investigated for H_2/CO_2 separation.[77, 78]

Hu et al. fabricated CMS membranes with sub-3.3 Å ultramicropores under low pyrolysis temperatures (500-600 ºC). By crosslinking polybenzimidazole (PBI) with pyrophosphoric acid (PPA), the PBI-PPA derived CMS membranes showed H_2 permeability of 140 Barrer with H_2/CO_2 selectivity of 58 at 150 ºC. The long-term stability of PBI-PPA-CMS was demonstrated using 50%H_2/50%CO_2 at 6 bar with periodic exposure to 0.3 mol% water vapor, where the CMS membranes showed stable H_2 permeability of 110 Barrer and H_2/CO_2 separation factor of 31 for 105 hours. Iyer and Zhang reported using aromatic polyamides derived CMS hollow fiber membranes for H_2/CO_2 separation.[77] The aramid-derived CMS membrane pyrolyzed at 925 °C showed H_2 permeability of 9 barrer with ultrahigh H_2/CO_2 ideal selectivity of 366, superior to the literature reported CMS membranes and far surpassing the 2008 Robeson polymer upper bond (**Figure 1.15**).

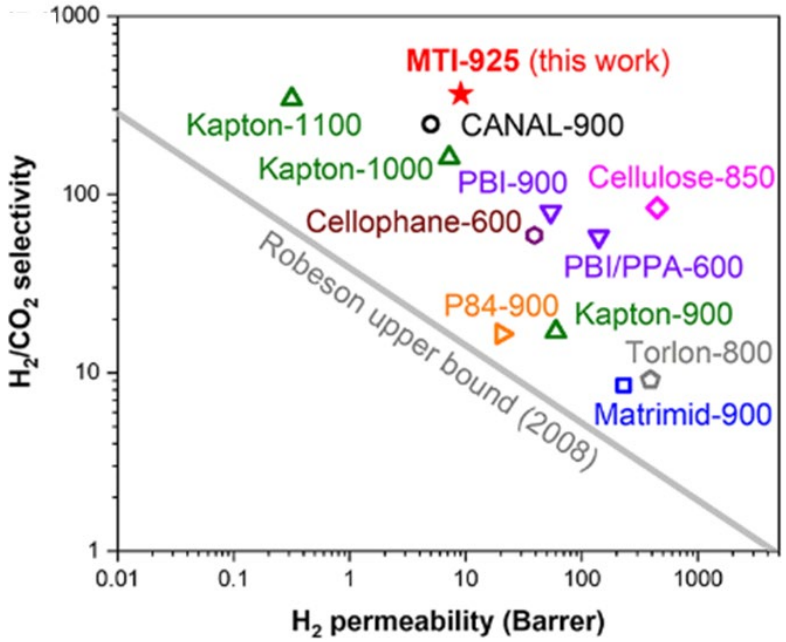

Figure 1.15. H_2/CO_2 separation performance in CMS membranes derived from different polymer precursors.[77]

1.3.2 Scalability of CMS membranes

CMS membranes can also be easily fabricated into practical hollow fiber format, providing high membrane packing density. Pilot-scale demonstration of CMS hollow fiber membranes have been reported for off-shore natural gas purification recently.[79] **Figure 1.16** shows the CMS hollow fiber membrane fabricated in this work, which has a small outer diameter of 315 μm with good mechanical flexibility. The structure and formation of CMS hollow membranes will be discussed in detail in Chapter 2. In contrast to previous membrane materials used in PDH membrane reactors (i.e., alumina, silica, zeolite, and palladium), CMS membranes are derived by carbonization of polymer precursors above their decomposition temperatures, which possess the potential to significantly reduce membrane fabrication costs at large scale.[62, 80]

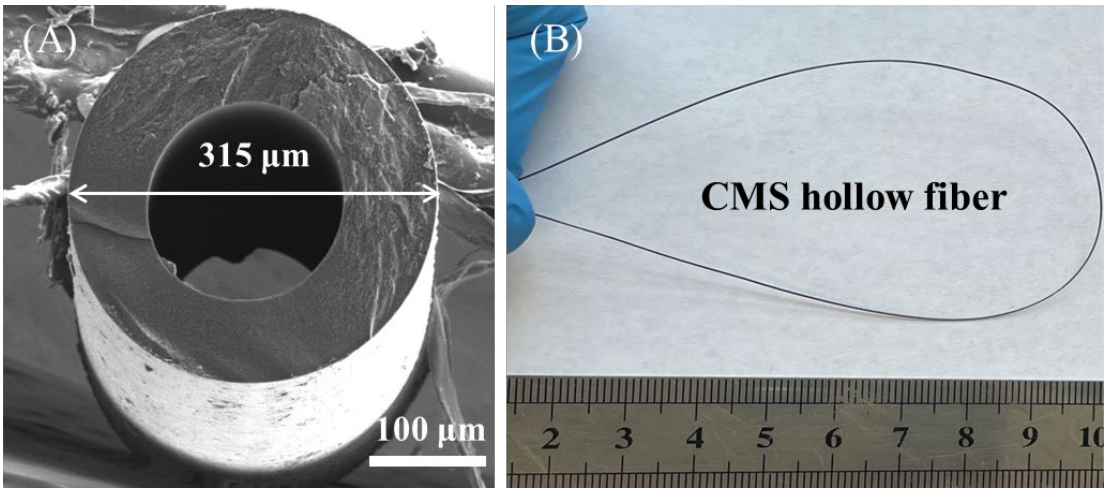

Figure 1.16. (A) SEM image of CMS hollow fiber membrane and (B) photo showing great mechanical flexibility of CMS hollow fiber.

1.3.3 CMS membrane reactors

Due to excellent thermal resistance and chemical stability, CMS membranes are also used in high-temperature gas and vapor separations. Sznejer and co-workers reported attractive hydrogen/hydrocarbon separation factors in dense-wall symmetric CMS hollow fiber membranes at temperatures up to 400 ºC.[81] Itoh and Haraya studied a hydrogen-permeable CMS membrane reactor for non-oxidative cyclohexane dehydrogenation at 195 ºC using a polyimide-derived CMS membrane.[82] The results showed cyclohexane conversion in the CMS membrane reactor exceeded the thermodynamic equilibrium conversion. Hydrogen-permeable CMS membrane reactors were also investigated for non-oxidative *iso*-butane dehydrogenation,[83] non-oxidative methyl-cyclohexane dehydrogenation,[84] water gas shift reaction,[85, 86] and methanol steam reforming,[87, 88] etc.

The above CMS membrane reactor studies use CMS membranes supported on thick (diameter 6 ~ 10 mm) ceramic tubular supports with low scalability and packing density. With much smaller diameters (~0.1-1 mm) and thin separation layers (0.5-5

μm), the recently emerged asymmetric CMS hollow fiber membranes[89] and composite CMS hollow fiber membranes[90, 91] can provide much higher membrane packing density and permeances[92, 93], which are more attractive than tubular CMS-ceramic membranes for membrane reactor applications.

1.4 Research objectives

The overarching goal of this work is to investigate low-temperature and stable propane dehydrogenation in catalytic membrane reactors (**Figure 1.17**) comprising asymmetric CMS hollow fine fiber membranes. The specific objectives of this research are listed below.

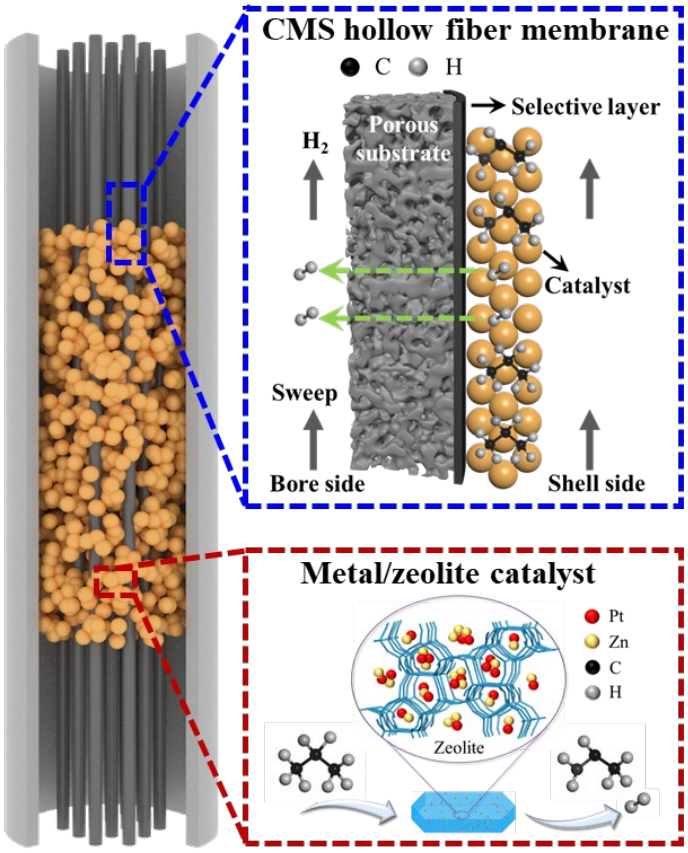

Figure 1.17. Schematic illustrating the CMS hollow fiber membrane reactor for propane dehydrogenation. Propane is converted to propylene and hydrogen over a metal/zeolite catalyst. Metal clusters are confined in siliceous zeolite activate propane without deactivation. CMS hollow fiber membranes selectively separates H_2 from the reaction mixture to drive the reaction forward.

Objective 1: Investigate high-temperature H_2/C_3H_8 separation in asymmetric CMS hollow fiber membranes

The first objective is to explore the high-temperature H_2/C_3H_8 separation performance of asymmetric CMS hollow fiber membranes in different conditions. The results allow us to evaluate the capability of asymmetric CMS hollow fiber membranes for non-oxidative propane dehydrogenation. Three key items are described below.

(1) The roles of membrane pyrolysis conditions and permeation temperature on high-temperature H_2/C_3H_8 separation performance are investigated.

(2) The effects of feed composition on the high-temperature H_2/C_3H_8 separation performance and pore structure of CMS hollow fiber membranes are studied.

(3) Long-term permeation measurements are carried out to demonstrate the stability of CMS hollow fiber membranes under high-temperature H_2/C_3H_8 permeation.

Objective 2: Investigate low-temperature and stable propane dehydrogenation in H_2-permeable CMS hollow fiber membrane reactors

The second objective is to develop and evaluate CMS hollow fiber membrane reactors for PDH. The membrane reactors are constructed using asymmetric CMS hollow fiber membranes developed in Objective 1 and platinum-zinc/silicalite-1 (Pt-Zn/S1) lab-synthesized catalysts by colleague Antara Bhowmick. The effects of the membrane reactor properties and operating conditions will be studied. The findings

demonstrate the competitiveness of CMS hollow fiber membrane reactors. Three key items are described below.

(1) High-temperature $H_2/C_3H_6/C_3H_8$ permeation performance will be studied in the CMS hollow fiber membranes.

(2) The effects of membrane area on CMS membrane reactor performance are studied.

(3) The effects of reaction conditions on CMS membrane reactor performance are investigated, which include reaction temperature, feed space velocity, feed C_3H_8 partial pressure, and sweep gas flow rate.

(4) Long-term stability of C_3H_8 conversion and C_3H_6 selectivity of the CMS hollow fiber membrane reactor for PDH is examined.

Objective 3: Modeling of CMS hollow fiber membrane reactors for propane dehydrogenation

Because no CMS hollow fiber membrane reactors have been studied prior to this PhD work, this objective develops models for the CMS hollow fiber membrane for PDH. The models allow us to predict the effects of membrane separation performance, catalyst properties, and reactor operation conditions on PDH membrane reactor performance. The modeling results also provide guidelines for experimental design of membranes and catalysts for PDH membrane reactors. Three membrane reactor models will be developed.

(1) A model is developed for H_2-permeable membrane reactor. The effects of membrane surface area, H_2 permeance, H_2/C_3H_8 selectivity, reaction temperature, feed space velocity, feed partial pressure, sweep flow rate and feed pressure on membrane

reactor performance are studied using the model and compared to the experimental results in Objective 2.

(2) A model is developed for C_3H_6-permeable membrane reactor. The roles of sweep composition, membrane separation layer thickness, and membrane C_3H_6/C_3H_8 separation factor on membrane reactor performance are studied using the model.

(3) A model for catalytic CMS hollow fiber membrane reactor is developed. The effect of membrane separation layer thickness and catalyst loading concentration on membrane reactor performance are studied using the model.

1.5 Dissertation organization

This dissertation is divided into 7 chapters including the current introduction chapter and is organized in the following manner: Chapter 2 describes the background of CMS membranes. Gas transport theory, asymmetric polymer hollow fiber membrane formation mechanism, and CMS membrane structure and formation are also provided. Chapter 3 describes the materials, experimental methods, characterization techniques, and equipment used throughout this research. Chapter 4 discusses the high-temperature H_2/C_3H_8 separations in CMS hollow fiber membranes. Chapter 5 discusses propane dehydrogenation in CMS hollow fiber membrane reactors. Chapter 6 describes modeling of CMS hollow fiber membrane reactors for propane dehydrogenation. Chapter 7 summarizes the key findings of this research and recommends several areas for future work in CMS membrane reactors.

Chapter 2: Background and theory

2.1 Overview

This chapter provides background, theory, and terminology of membrane materials studied in this dissertation. Section 2.2 provides background on the structure and formation of carbon molecular sieve (CMS) membranes. Section 2.3 describes fundamental gas transport theory in CMS membranes. Section 2.4 shows the formation mechanism and fabrication processes of asymmetric hollow fiber membranes. The impacts of skin integrity, separation layer thickness, substructure transport resistance, and macroscopic properties on asymmetric hollow fiber membrane separation performance are discussed.

2.2 Carbon molecular sieve (CMS) membranes

2.2.1 Structure of CMS membranes

CMS membranes are derived by carbonization of polymer precursors above their decomposition temperatures under controlled conditions.[94, 95] When being heated under an inert atmosphere, polymers can either form coke or char. Coke can be further heated to form crystalline graphite at temperatures between 2500 ^{o}C and 3000 ^{o}C while char remains in an amorphous form.[96, 97] Polymers that can form char formation during decomposition are typically used as CMS precursors. CMS membranes used for gas separations typically have a turbostratic structure with very little long-range order and can be considered as isotropic.[62] Over the long range, this amorphous structure contains randomly arranged, bent and twisted carbon sheets

(**Figure 2.1 A**). Over the short range, the graphene-like sheets align parallel to each other and form a somewhat ordered structure (**Figure 2.1 B**). Pores in CMS are formed from imperfect packing between these graphene-like sheets.

An idealized pore structure of CMS can be described as slit-like structure (**Figure 2.2 A**) and can be represented by a bimodal pore size distribution (**Figure 2.2 B**).[98, 99] The slit-like pores are comprised of micropore "chambers" (7-20 Å) and ultramicropore "windows" (< 7Å), where the micropores provide sorption sites and ultramicropores enable molecular-sieving behavior. This unique pore structure gives CMS membranes simultaneously high productivity and high separation efficiency exceeding those of polymer membranes and competitive with many inorganic membranes.[61, 100, 101] Owing to their good tunability, CMS membranes have shown attractive separation performance for many economically important gas, vapor, and organic solvent separations.[65, 68, 102, 103]

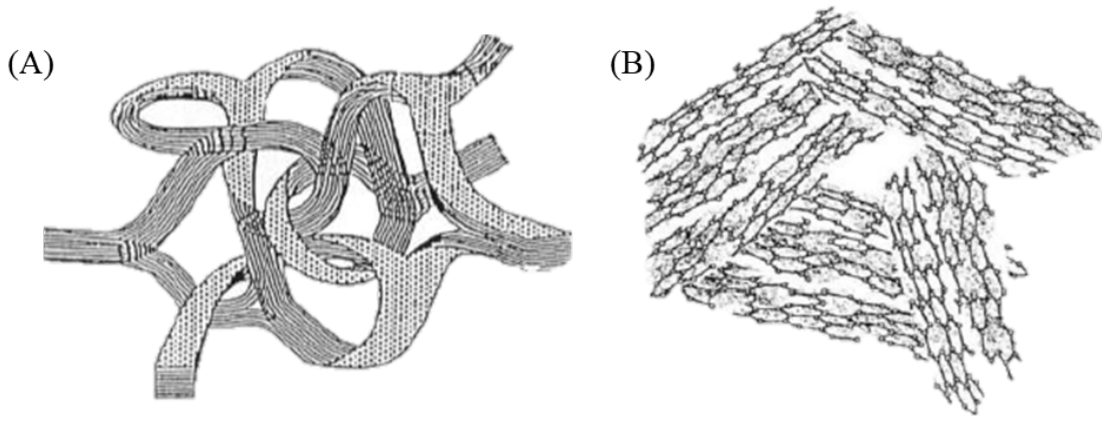

Figure 2.1. (A) Turbostratic carbon structure. (B) CMS structure over a short range: sp^2-hybridized carbon sheets.[74]

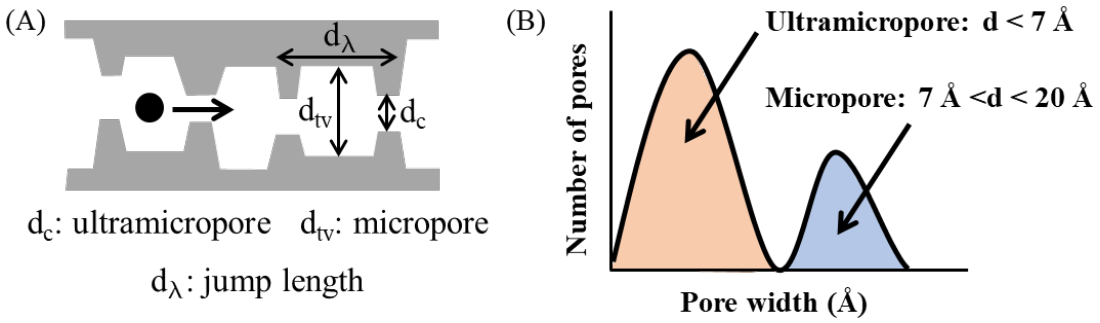

Figure 2.2. (A) Idealized slit-like pore structure in CMS membrane. (B) Bimodal pore size distribution of CMS membrane.[104]

2.2.2 Formation of CMS membranes

CMS membranes are formed by high-temperature pyrolysis of polymer precursors under controlled conditions.[105, 106] During pyrolysis, multiple reactions take place at the same time including cleavage, dehydrogenation, condensation, etc.[107, 108] In the early stages of pyrolysis, bonds cleavage occurs and forms free radicals. These free radicals further go through intermolecular crosslinking and intramolecular coupling, leading to a loose structure network. Meanwhile, small molecules (water, carbon dioxide, carbon monoxide, methane, etc.) are eliminated as volatiles, generating microporosity within the rigid macromolecular system. The pore size distribution of CMS, which determines separation performance, is largely influenced by several key parameters including polymer precursor selection, polymer pretreatment, pyrolysis conditions, and post treatment. These primary parameters are reviewed and discussed in the following sections.

2.2.2.1 CMS membrane geometry

CMS membranes can be either dense, asymmetric, or composite.[109] Dense CMS membranes are preferred to characterize membrane intrinsic permeation properties because the separation layer thickness can be unambiguously determined. Dense CMS films can be made by pyrolysis of polymer precursor dense films. Dense-walled CMS hollow fibers can be derived from asymmetric polymer precursor hollow fibers by purposefully allowing the porous substrate to collapse.[71] Asymmetric CMS hollow fiber membranes are derived from asymmetric polymer precursor hollow fibers while preventing the porous substrate from collapse. Composite CMS hollow fiber membranes are derived from dual-layer sheath-core precursor hollow fiber membranes.[91]

2.2.2.2 Polymer precursor chemistry

Polymer precursor chemistry can strongly affect CMS membrane transport properties and separation performance. A wide variety of polymers have been studied as CMS precursors, such as polyimides, polyacrylonitrile, phenolic resin, polyfurfuryl alcohol, poly(vinylidene)-based polymers, cellulose derivatives, polymers of intrinsic microporosity (PIM), polybenzimidazole (PBI), etc.[103, 110-118] Notably, polyimides have been extensively used as precursor materials due to their high glass transition temperature (T_g), outstanding solution processibility, and good mechanical strength.[119] For example, Matrimid® 5218, a commercialized polyimide, has been extensively studied as polymer precursor material for CMS membranes. Matrimid has a high T_g of 305 °C and a good carbon residue of ~50 wt% under N_2 atmosphere up to 1000 °C.[120] Besides, Matrimid is soluble in N-Methyl-2-pyrrolidone (NMP), which

can be easily fabricated into practical hollow fiber format, providing high membrane packing density. In comparison to Matrimid, polyethylene (PE) is not a good polymer precursor for CMS membrane. PE has a very low Tg of -130 ~ -125 ^{o}C and a melting point of 130 ~ 140 ^{o}C. PE is not an aromatic material, leading to low carbon residue below 5 wt% when heated up to 600 ^{o}C under N_2 atmosphere.[121] Besides, PE barely has solution processibility as PE is not soluble in water and many organic solvents.

The CMS membrane separation performance can be correlated to the intrinsic properties of polymer precursors including fractional free volume (FFV), inter-chain interactions, and chain rigidity.[122, 123] Polyimides can be synthesized from different diamines and dianhydrides, where copolymers can also be added to further tune the properties of polyimides. The role of precursor chemistry on CMS membrane formation can be illustrated by comparing CMS membranes derived from the Matrimid® polyimide and the 6FDA/BPDA-DAM polyimide (**Table 2.1**).[124] Each repeating unit of 6FDA/BPDA-DAM contains two bulky CF_3 groups, which provides higher free volume than Matrimid® by inhibiting effective chain and segmental packing. The evolution of large fluorinated compounds such as CHF_3 promotes microporosity formation in 6FDA/BPDA-DAM-derived CMS membranes, thereby giving higher gas permeability than Matrimid® derived CMS membranes under identical pyrolysis conditions.

Table 2.1. Chemical structure and properties of Matrimid® 5218 polyimide and 6FDA/BPDA-DAM polyimide.[124]

Polymer	Chemical structure
Matrimid® 5218 (BTDA-DAPI) T_g: 305 °C T_d: 425 °C FFV: 0.110	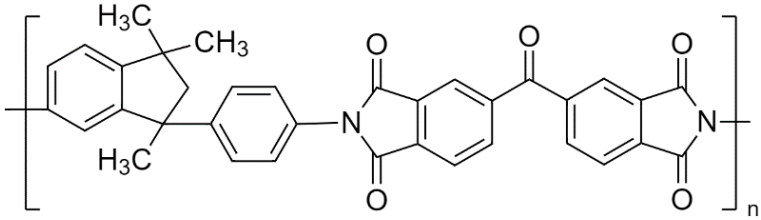
6FDA/BPDA-DAM T_g: 424 °C T_d: 450 °C FFV: 0.145	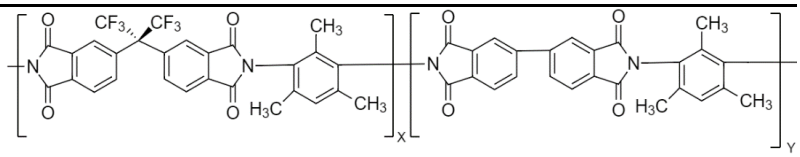 The ratio of X to Y is 1:1

T_g: glass transition temperature
T_d: decomposition temperature
FFV: fractional free volume
BTDA: 3,3′,4,4′-benzophenone tetracarboxylic dianhydride
DAPI: diamino-phenylindane
6FDA: 5,5′-[2,2,2-trifluoro-1-(trifluoromethyl)ethylidene] bis-1,3-isobenzofurandione
BPDA: 3,3′,4,4′-biphenyltetracarboxylic dianhydride
DAM: 2,4,6-trimethyl-1,3-phenylenediamine

2.2.2.3 Polymer pretreatment

The purpose of pretreatment is to stabilize polymer precursors and preserve the porous substructure during pyrolysis. Chemical modification is typically used for precursor pretreatment to tailor the separation performance of the resulting CMS membrane. Several methods such as polymer-crosslinking [125], non-solvent treatment [126] and grafting of functional groups [127-129] on polyimide precursors have been studied to improve the separation properties of CMS dense films.

For example, chemical crosslinking using p-xylenediamine solutions was performed on Matrimid® precursor.[125] The reaction mechanism is the diamine-imide reaction to open the imide rings of the polymer precursor, leading to a permeability decrease in the resulting CMS membrane. Different kinds of nonsolvent (methanol, ethanol, propanol, and butanol) have been selected to study the non-solvent soaking effects on Matrimid ® and P84 precursor.[126] The resulting CMS showed improvements in selectivity due to structural re-organization of solvent-treated precursors, leading to smaller pores in CMS during pyrolysis. The effects of bromination and sulfonation on polyimide precursors were also investigated to improve the CMS transport properties.[127, 128] Since the molecular structure of the precursor has already changed, the CMS derived from modified precursors could have very different separation properties. Two pre-pyrolysis treatment approaches were developed for asymmetric polymer precursor hollow fiber membranes and were described in detail below.

2.2.2.3.1 Silane treatment

The silane treatment method was developed by Bhuwania et al. to restrict the substructure collapse in asymmetric CMS hollow fiber membranes.[89] This technique applied a sol-gel reaction to have crosslinked silica formed on the precursor fiber porous substrate, which prevents the substructure collapse during pyrolysis. The polymer precursor fibers were first saturated with vinyltrimethoxysilane (VTMS) liquid and then exposed to moisture at room temperature. When the VTMS came into contact with the water vapor, the moisture-hydrolysis occurred followed by simultaneous condensation to form the vinyl-crosslinked silica (**Figure 2.3 A**). The

silica layer was formed on the porous substructure pore walls, which restricts the polymer precursor chain mobilization during pyrolysis (**Figure 2.3 B**). Notably, the silane treatment did not involve the chemical reaction with the precursor molecular structure, providing a simple integral way to prevent substructure collapse on any class of asymmetric CMS precursor materials.

Bhuwania and coworkers studied the impacts of silane treatment on Matrimid® 5218 and 6FDA/BPDA-DAM derived asymmetric CMS hollow fiber membranes. The CMS membrane separation layer thickness reduced 5-6 times by pyrolyzing the silane-treated asymmetric precursor hollow fibers, giving significantly improved membrane gas permeances. The Matrimid® derived asymmetric CMS hollow fiber membranes with silane treatment showed more than 3 times higher gas permeances than the untreated CMS membranes. Similar gas permeance improvements by more than 4 times were observed for silane-treated 6FDA/BPDA-DAM derived CMS membranes.

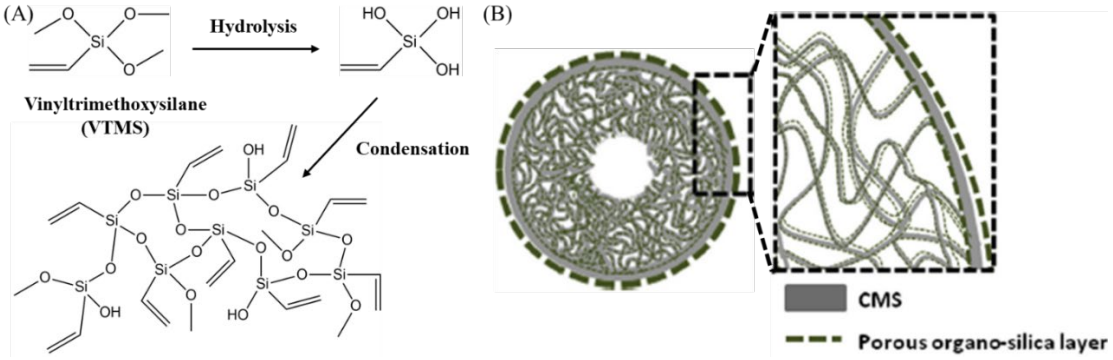

Figure 2.3. (A) Sol-gel crosslinking reaction between VTMS and moisture at room temperature. (B) Schematic illustration of silica layer distribution on silane-treated asymmetric CMS hollow fiber membranes.[89]

2.2.2.3.2 In-situ hybridization treatment

The in-situ hybridization method was developed by Zhang. et al to repair skin layer defects of ultrathin CMS hollow fiber membranes.[91] After silane treatment for

precursor hollow fibers as described in previous section, the precursor fiber skin layer was in-situ hybridized by sequentially soaking in diethyltoluenediamine (DETDA)/hexane solution and trimesoyl chloride (TMC)/hexane solution. The condensation polymerization of the two highly reactive monomers formed crosslinked polyamides that fill into the precursor fiber skin defects (**Figure 2.4**). During pyrolysis, the polyamide inside the defects were transformed into CMS and thus healing the skin defects on CMS hollow fiber membranes. By increasing the monomer concentration from 0 to 0.1wt%, the CO_2/CH_4 separation factor of the resulting ultrathin CMS membranes significantly increased from 8 to 37, indicating the high efficiency of hybridization on repairing skin defects of CMS membranes.

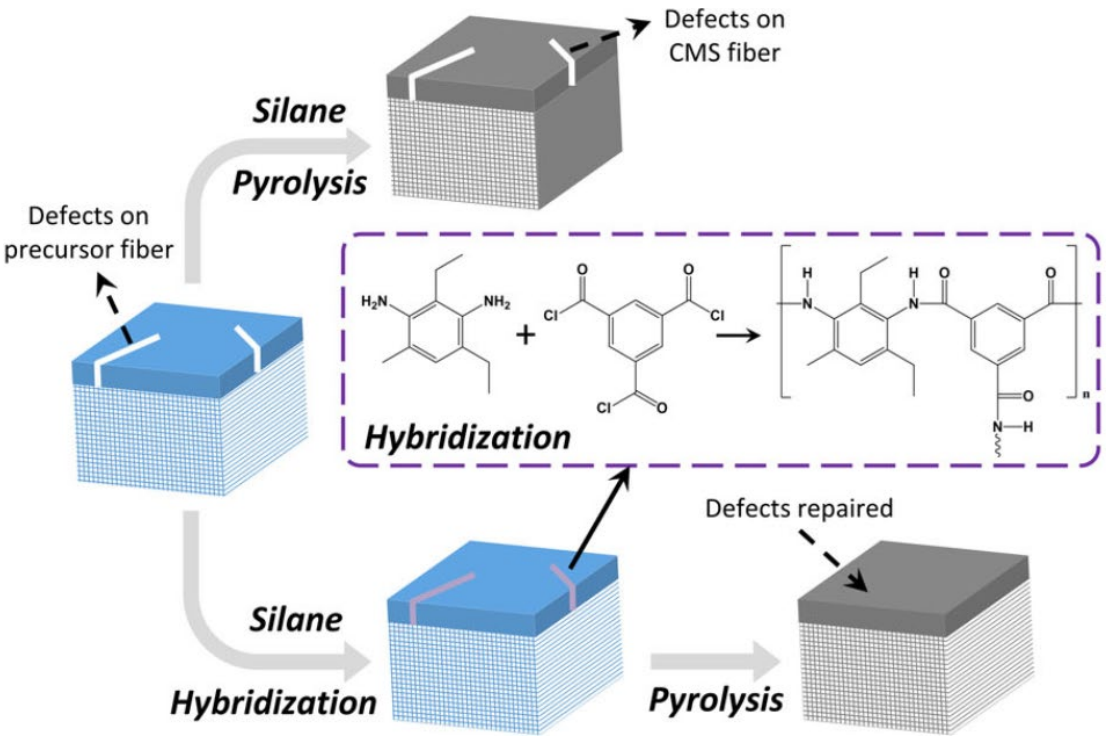

Figure 2.4. Schematic illustration of repairing ultrathin CMS hollow fiber membrane skin layer defects by in-situ hybridization. The inset picture shows the reaction between the DETDA and TMC to form the crosslinked polyamide.[91]

2.2.2.4 Pyrolysis conditions

The pyrolysis step transforms the polymer into carbon molecular sieves under controlled conditions.[130] The pore structure of CMS membranes is described as slit-like pores, where the micropores are interconnected with ultramicropores. The pore size distribution of CMS can be tuned by adjusting pyrolysis parameters including pyrolysis temperature, thermal ramp rate, thermal soak time, and pyrolysis atmosphere.

Pyrolysis temperature is the highest temperature to which the precursor is heated. The temperature should be high enough to let the polymer decompose and transform into carbon while still maintaining a porous structure.[131] A densely packed graphitic structure is not desirable. Therefore, the pyrolysis temperature is usually chosen to be above the polymer decomposition temperature but well below the graphitization temperature. In most studies, pyrolysis temperature is between 500 ºC and 1000 ºC.

The pyrolysis temperature was found to be a key factor in controlling CMS pore size distribution and thus altering the CMS membrane permeation properties.[132, 133] Generally, a higher pyrolysis temperature provides CMS membrane with a more compact structure (**Figure 2.5**), where both the micropores and ultramicropores are tightened. This usually results in a decrease in permeability and an increase in selectivity. Zhang et al. reported the pyrolysis of Matrimid polyimide precursor hollow fibers between 750 and 900 ºC.[71] The CMS membrane pyrolyzed at 900 ºC exhibited some of the highest ideal permselectivities (e.g., $\alpha[CO_2/CH_4]$=3650, $\alpha[N_2/CH_4]$=63, $\alpha[He/\ CH_4]$=16700) due to the formation of the ultraselective micropores that

selectively excluded bulkier CH_4 molecules during permeation. The optimal pyrolysis temperature depends on the polymer precursor and the specific gas pairs of interest.

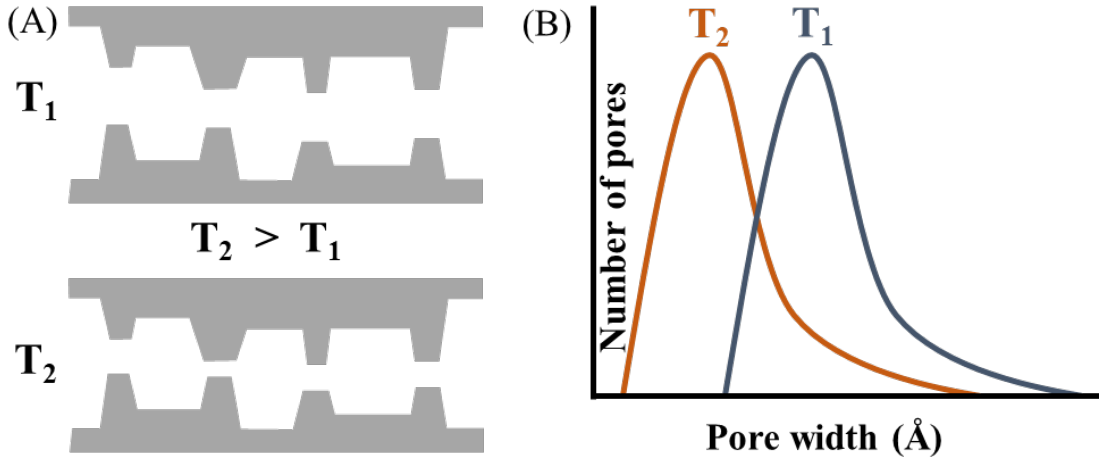

Figure 2.5. (A) Schematic illustration showing the effect of pyrolysis temperature on CMS membrane pore structure. (B) Effect of pyrolysis temperature on pore size distribution of CMS membrane.

Ramp rate is the heating rate to reach the final pyrolysis temperature. It determines the evolution rate of volatile components from the polymer precursor. A lower heating rate generally allows the formation of smaller pores and thus higher selectivity of CMS membranes.[94, 134] On the other hand, excessively high ramp rate tends to form pinholes, microscopic cracks, blisters, and distortion in CMS membranes, leading to high permeability but decreased selectivity. The ramp rate near the final pyrolysis temperature needs to be carefully controlled, where a slow "buffering" step is typically applied to prevent overheating the membranes above the final pyrolysis temperature. Soak time is the time where the membrane is held at the final pyrolysis temperature. During the thermal soaking process, the microstructure of the CMS membrane may be further tuned to obtain desired transport properties. A longer soaking time generally increases the selectivity and decreases the permeability of CMS

membranes, which is caused by compaction of the disordered graphene sheets.[98, 133] Usually, the impact of soaking time is more obvious on permeability than selectivity.[95]

CMS membranes are usually formed by pyrolysis under vacuum or inert atmosphere to avoid undesirable combustion of polymer precursors.[130] Recent studies show that inert gas purge is preferred to vacuum to provide good reproducibility in CMS membrane formation.[74] Pyrolysis atmosphere can be used as a tool to tune the pore structure of CMS membranes. For example, inert gas purge with trace amount of oxygen, known as oxygen doping, has been investigated to tailor CMS membrane transport properties.[135] The oxygen doping method relies on the chemisorption of oxygen on the edge of selective ultramicropores under high temperatures, thereby narrowing down the average ultramicropore size of CMS. The schematic illustration of oxygen doping during membrane pyrolysis is shown in **Figure 2.6**. The CMS membrane becomes less permeable and more selective as the amount of oxygen in the inert purge gas increases up to a cut-off point. When the oxygen doping amount exceeds the critical level, low gas permeability and low selectivity are observed in CMS membranes.[136]

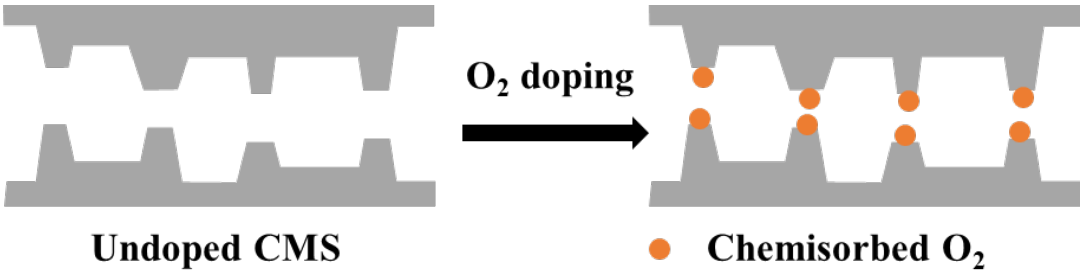

Figure 2.6. Effect of oxygen doping on CMS membrane microstructure.[135]

Ma et al. reported the introduction of H_2 to the pyrolysis atmosphere to create mid-range (5-9 Å) microstructures in CMS membrane.[103] The polymer of intrinsic microporosity (PIM-1) was selected as the polymeric precursor and was pyrolyzed under low H_2 volume fractions for CMS fabrication. The H_2-assisted CMS membrane showed 15 times higher p-xylene permeability with slightly dropped p-xylene/o-xylene selectivity when compared to CMS prepared by pyrolyzing PIM-1 under pure Ar. The existence of H_2 in the pyrolysis atmosphere suppressed the inter strand reaction, leading to larger average gaps between carbon strands as illustrated in **Figure 2.7 A**. Since the slits between strands form the ultramicropores in CMS materials, the presence of H_2 in the pyrolysis environment enlarges the ultramicropores with minor changes in micropore size of CMS (**Figure 2.7 B**).

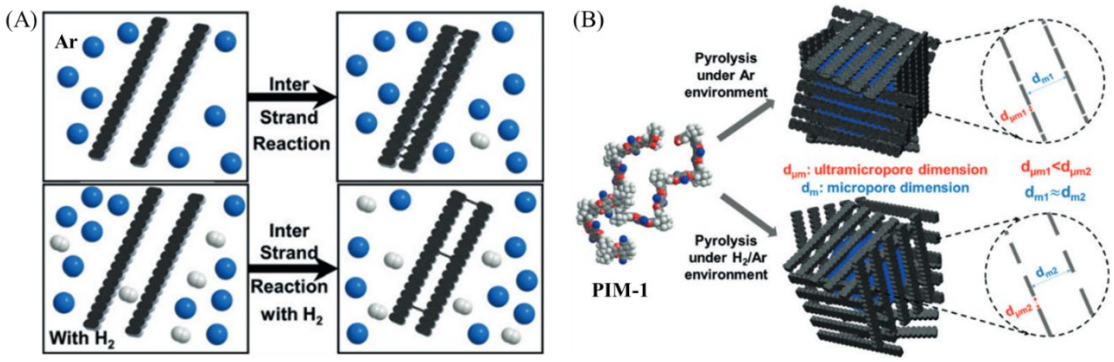

Figure 2.7. Schematics showing the effect of adding H_2 to the pyrolysis environment on the (A) inter strand reaction during pyrolysis and (B) CMS membrane pore structure. (blue=Ar, white=H_2).[103]

2.1.2.5 Post treatment

After pyrolysis, post treatments can be applied to finely tune CMS membrane pore size distribution to meet various separation needs. Chemical vapor deposition (CVD) is typically used to improve gas selectivity of carbon membranes by introducing carbonaceous species into the membrane pore network.[105, 137] The organic species

and their pyrolysis conditions need to be carefully selected to produce sufficient carbon deposition at the membrane pore apertures. Organic molecules such as ethane, ethylene, propane, propylene have been studied for CVD purposes.[138] For example, Yoshimune and Haraya reported using one-step CVD of propylene to tune the pore structure of carbon hollow fiber membranes.[139] Sulfonated poly(phenylene oxide) (SPPO) was selected as the polymer precursor material and pyrolyzed under N_2 atmosphere to obtain carbonized SPPO membranes. The CVD was performed by supplying propylene to the pyrolysis atmosphere in the latter part of thermal soaking time. The carbon membrane with CVD of 100% propylene for 5 min showed lower gas permeances but significantly improved H_2/CH_4 selectivity from 130 to 1625. By adjusting the propylene volume fraction and CVD time, the gas separation performance can be easily controlled.

The coating technique can be used to repair skin layer defects in carbon membranes.[105] Petersen et al. treated carbon membrane by immersing it into 2 wt% polydimethylsiloxane (PDMS) in heptane.[134] After drying, a thin PDMS layer was coated on the membrane surface to prevent gas flow through defects. The PDMS coated carbon membrane showed dramatically increased H_2/N_2 selectivity of 1960 as compared to uncoated carbon membrane with H_2/N_2 selectivity of 180. On the other hand, Koros and Jones coated hollow fiber carbon membranes using poly(4-methyl-1-pentene) (PMP) to protect the carbon membrane from adverse effects when exposed to water vapor.[140] Compared to O_2 flux loss of 58% in uncoated carbon membrane, the PMP coated carbon membrane showed O_2 flux loss of 11% under 83-85% relative humility (RH) for 24 hours. The polymeric coating layer is highly hydrophobic without

reducing the flux of other permeating molecules, making the coated carbon membranes much more resistant to humidity exposure.

2.3 Gas transport in membranes

2.3.1 Permeation

Membranes are selective barriers that can separate a gas mixture into a retentate stream concentrating with the slower permeating gas and a permeate stream concentrated with the faster permeating gas. Gas transport in CMS membranes follows the sorption-diffusion mechanism.[141] Gas molecules first sorb on the high-pressure upstream side of the membrane, then diffuse through the membrane along the chemical concentration gradient, and finally desorb on the low-pressure downstream side (**Figure 2.8**).

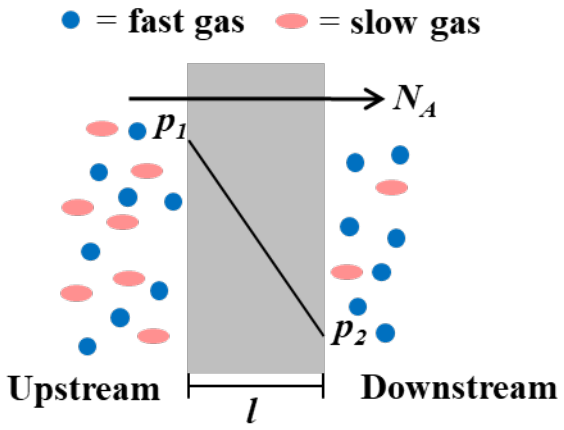

Figure 2.8. Schematic of gas permeation through CMS membranes.

Membrane intrinsic separation performance is characterized by permeability and ideal selectivity, respectively. The permeability of penetrant A (P_A, Barrer) is defined as steady-state gas flux (N_A, $\mathrm{cm^3(STP)/cm^2/s}$) normalized by transmembrane

partial pressure difference ($\Delta p_A, \mathrm{cmHg}$) and membrane separation layer thickness (l, cm)

$$P_A = \frac{N_A \cdot l}{\Delta p_A} \tag{2.1}$$

The unit for permeability is Barrer

$$1\ \mathrm{Barrer} = 1 \times 10^{-10} \frac{\mathrm{cm^3(STP)} \cdot \mathrm{cm}}{\mathrm{cm^2} \cdot \mathrm{s} \cdot \mathrm{cmHg}} \tag{2.2}$$

For symmetric dense film membrane, membrane separation layer thickness can be directly measured. However, the separation layer thickness of asymmetric hollow fiber membranes usually cannot be unambiguously determined. Permeance ($P_A/l, \mathrm{GPU}$) is thus used to describe the membrane productivity of asymmetric hollow fiber membranes, which is defined as transmembrane pressure difference normalized flux

$$\frac{P_A}{l} = \frac{N_A}{\Delta p_A} \tag{2.3}$$

The unit for permeance is gas permeation unit (GPU)

$$1\ GPU = 1 \times 10^{-6} \frac{\mathrm{cm^3(STP)}}{\mathrm{cm^2} \cdot \mathrm{s} \cdot \mathrm{cmHg}} \tag{2.4}$$

The ideal selectivity of a membrane is defined as the ratio of permeabilities or permeances

$$\alpha_{A/B} = \frac{P_A}{P_B} = \frac{P_A/l}{P_B/l} \tag{2.5}$$

With mixture feed, separation factor is often used to describe membrane separation efficiency

$$\alpha_{A/B} = \frac{y_A/y_B}{x_A/x_B} \tag{2.6}$$

where y and x are molar composition at membrane downstream side and upstream side, respectively. For sorption-diffusion permeation, permeability can further be written as the product of diffusion coefficient ($D_A, \mathrm{cm}^2/\mathrm{s}$) and sorption coefficient ($S_A, \mathrm{cm}^3[\mathrm{STP}]/\mathrm{cm}^3/\mathrm{cmHg}$)

$$P_A = D_A \cdot S_A \tag{2.7}$$

Selectivity can be partitioned into the diffusion selectivity (D_A/D_B) multiplied by the sorption selectivity (S_A/S_B)

$$\alpha_{A/B} = \frac{D_A}{D_B} \cdot \frac{S_A}{S_B} \tag{2.8}$$

The temperature dependence of diffusion coefficient and sorption coefficient can be described by the Arrhenius relationship (Eqn. 2.9) and Van't-Hoff equation (Eqn. 2.10), respectively.

$$D_A = D_{A0} \exp\left(-\frac{E_{D,A}}{RT}\right) \tag{2.9}$$

$$S_A = S_{A0} \exp\left(-\frac{\Delta H_{S,A}}{RT}\right) \tag{2.10}$$

where D_{A0} (cm^2/s) and S_{A0} ($\mathrm{cm}^3[\mathrm{STP}]/\mathrm{cm}^3/\mathrm{cmHg}$) are pre-exponential factors, R is the universal gas constant ($\mathrm{J/mol/K}$), and T is absolute temperature (K), $E_{D,A}$ is activation energy for diffusion ($\mathrm{kJ/mol}$) and $\Delta H_{S,A}$ is heat of sorption ($\mathrm{kJ/mol}$). According to Eqn. 2.7, the temperature dependence of permeability follows an Arrhenius relationship

$$P_A = P_{A0} \exp\left(-\frac{E_{P,A}}{RT}\right) \tag{2.11}$$

where P_{A0} (Barrer) is the pre-exponential factor and $E_{P,A}$ is the apparent activation energy for permeation (kJ/mol). According to Eqn. 2.9-2.11, permeation activation energy is the summation of diffusion activation energy and heat of sorption

$$E_{P,A} = E_{D,A} + \Delta H_{S,A} \tag{2.12}$$

2.3.2 Sorption and diffusion

Gas sorption is controlled by interactions between the gas molecules and membrane materials. Sorption coefficients of gases in a membrane are greatly influenced by the condensability of gas molecules. Critical temperature is a good measure of the condensability of a gas penetrant. Gases with a higher critical temperature typically are more condensable and more sorptive in membranes. Sorption coefficient can be written as the equilibrium sorption capacity $\mathrm{C_A}$ ($\mathrm{cm^3_{gas}(STP)/cm^3_{membrane}}$) divided by the gas-phase partial pressure p_A (cmHg)

$$S_A = \frac{\mathrm{C_A}}{p_A} \tag{2.13}$$

The sorption in CMS materials can be described by the dual mode model, where Langmuir sorption describes the sorption in the large volume fraction of microporous domains and Henry's law describes the sorption in the minority continuous phase.[142] The dual mode model can be written as

$$C_A = C_{C,A} + C_{L,A} = k_{C,A}p_A + \frac{\mathrm{C'_{LA}}b_A p_A}{1 + b_A p_A} \tag{2.14}$$

Where $C_{C,A}$ ($\mathrm{cm^3_{gas}(STP)/cm^3_{membrane}}$) is sorption capacity in the continuous phase, $C_{L,A}$ ($\mathrm{cm^3_{gas}(STP)/cm^3_{membrane}}$) is the Langmuir sorption capacity, $k_{C,A}$ ($\mathrm{cm^3_{gas}(STP)/cm^3_{membrane}/cmHg}$) is the continuous mode's sorption constant, $\mathrm{C'_{L,A}}$ ($\mathrm{cm^3_{gas}(STP)/}$

$cm^3_{membrane}$) is the Langmuir capacity constant, b_A ($cmHg^{-1}$) is the Langmuir affinity constant. The sorption coefficient of CMS, therefore, is given by

$$S_A = k_{C,A} + \frac{C'_{L,A} b_A}{1 + b_A p_A} \tag{2.15}$$

The diffusion coefficient measures the mobility of gas molecules permeating through the membrane. In CMS materials, gas molecules diffuse through the membrane via activated jumps from one sorptive micropore to another by passing the restrictive ultramicropores (**Figure 2.9**).[143] Gas molecules sorbed in micropores are in the normal state while those passing through the ultramicropores are in the activated state. Gas molecules need to overcome the repulsive interaction energy from the rigid carbon wall when going through the ultramicropores.

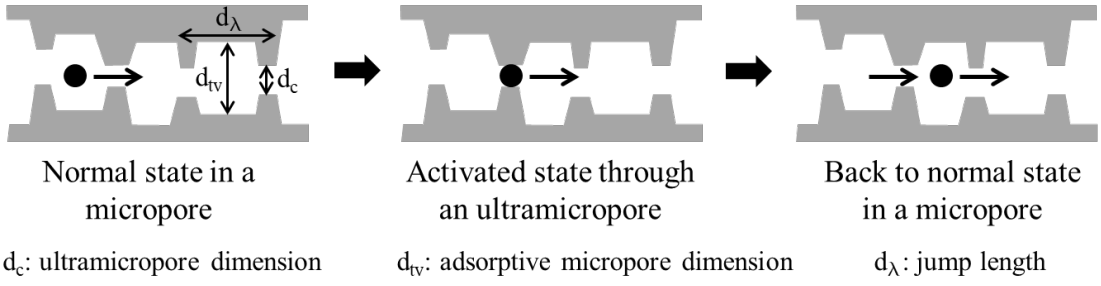

Figure 2.9. Conceptual illustration of a diffusion step in CMS membranes.[144]

According to Eyring theory of rate [145], the diffusion coefficient can be expressed as

$$D = \lambda^2 \frac{kT}{h} e^{S_D/R} e^{-H_D/RT} \tag{2.16}$$

where λ (cm) is the average diffusive jump length in the membrane, k is the Boltzmann's constant (1.38×10^{-23} J/K), h is the Planck's constant (1×10^{-34} J · s), S_D (J/mol/K) is the activation entropy of diffusion, H_D (J/mol) is the activation enthalpy of diffusion, and R (J/mol/K) is the gas constant. When the volume change in the diffusion process is negligible,

$$H_D = E_D + PV \approx E_D + RT \tag{2.17}$$

Substitute Eqn. 2.17 into Eqn. 2.16,

$$D = e\lambda^2 \frac{kT}{h} e^{S_D/R} e^{-E_D/RT} \tag{2.18}$$

λ can be considered identical for different penetrants since the average distance between equilibrium micropores are assumed to be the same. Then the diffusion selectivity can be written as

$$\frac{D_A}{D_B} = \underbrace{\left[\exp\left(\frac{S_{D,A} - S_{D,B}}{R}\right)\right]}_{\text{Entropic selectivity}} \underbrace{\left[\exp\left(-\frac{E_{D,A} - E_{D,B}}{R}\right)\right]}_{\text{Energetic selectivity}} \tag{2.19}$$

The diffusion selectivity can thus be deconvoluted into the "Entropic selectivity" and "Energetic selectivity". The capability of ultramicropores to discriminate sizes and shapes of different gas molecules is known as "Entropic selectivity". The difference in the diffusion activation energies required to make jumps provides "Energetic selectivity".[146] In polymeric membranes, the entropic selectivity is close to unity while a much higher entropic selectivity is observed in CMS membranes. The high entropic selectivity stems from the rigid CMS pore structures absent in polymer membranes. The much higher entropic selectivity is responsible for the outstanding selectivities of CMS membranes.

2.4 Asymmetric hollow fiber membranes

2.4.1 Formation of asymmetric polymer hollow fiber membranes

Asymmetric polymer hollow fiber membranes comprise a thin and dense skin layer supported by a porous substructure, which is formed by the dry-jet/wet-quench spinning process (**Figure 2.10**).[147] During hollow fiber spinning, the polymer solution (also known as "dope") and bore fluid are coextruded through a spinneret into an air gap ("dry-jet") and then the dope line is immersed into a water bath ("wet-quench"). The dry-jet step forms the dense skin layer, and the "wet-quench" step produces the porous substrate by phase separation. The hollow fiber bore is provided by the bore fluid, which is a neutral solution occupying the fiber inner space and can be removed by solvent-exchange and drying steps. Several key spinning parameters for fabricating defect-free polymer hollow fiber membranes are listed in **Table 2.2**.[148]

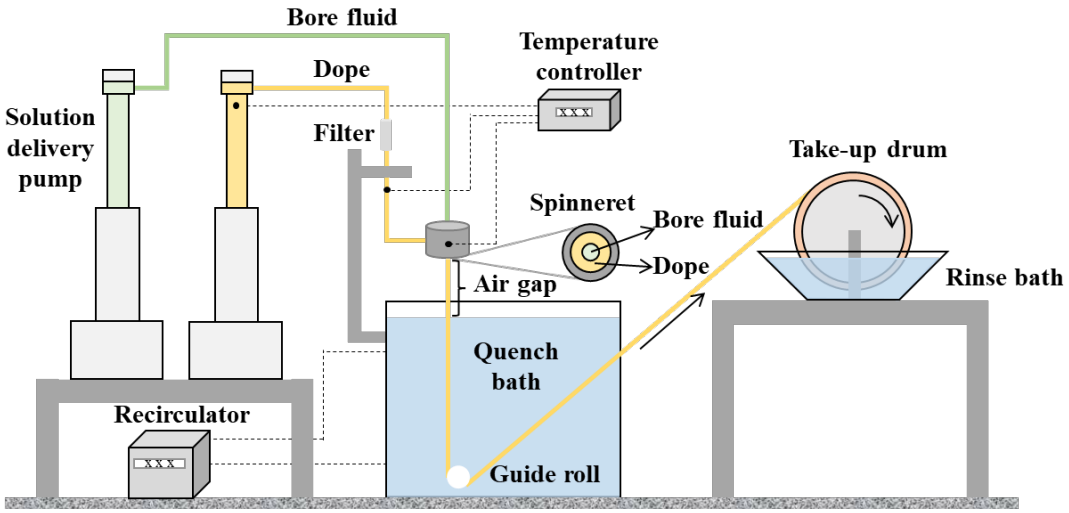

Figure 2.10. Schematic of dry-jet/wet-quench spinning process for asymmetric hollow fiber fabrication.[149]

Table 2.2. Spinning parameters in a dry-jet/wet-quench hollow fiber spinning process.[74]

Dope composition	Air gap height	Quench bath temperature
Bore fluid composition	Fiber take-up rate	Quench bath composition
Dope/bore fluid flow rate	Spinning temperature	Humidity

A good dope composition means both spinnability and the potential for defect-free skin layer formation. Sufficient viscosity is the first important factor for successful spinning.[150] Polymer molecular weight and polymer concentration are the dominant factors for sufficient viscosity. A ternary phase diagram (**Figure 2.11**) with a bimodal line provides guidance for finding a good dope composition. The bimodal line is constructed by cloud point technique.[151] At a fixed polymer concentration, a series of dope samples with increasing non-solvent to solvent ratio were made. The dope becomes cloudy with the increase of non-solvent concentration, changing from one-phase into two-phase. The dope composition on the phase boundary line is referred to "cloud point". The bimodal line is formed by connecting cloud points under different polymer concentrations. A good dope composition should sit in the one-phase region and be close to the bimodal line. To find the optimized dope composition for a specific polymer, the dope formulation step may be iterated based on the morphology and separation performance of the polymer hollow fiber membranes.

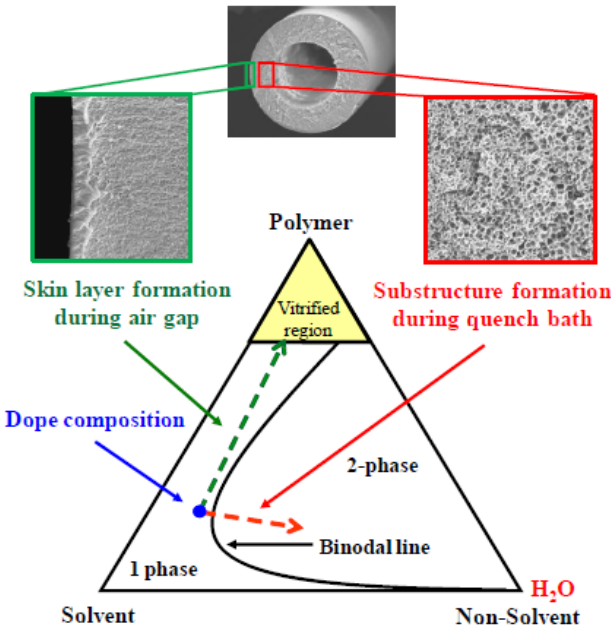

Figure 2.11. Ternary phase diagram demonstrating the asymmetric hollow fiber membrane formation process.[74]

Changes in polymer hollow fiber composition during spinning can also be illustrated using the ternary phase diagram (**Figure 2.11**).[152] The initial dope composition sits in the one-phase region and stays close to the bimodal line for rapid phase separation in the water bath. In the air gap, the evaporation of volatile components in the dope drives the outer surface of the extruded dope to the vitrified region, thereby forming the dense skin layer. As the extruded polymer dope reaches the quench bath, water (non-solvent) diffuses into the polymer solution and drives the dope composition across the bimodal line to enter the two-phase region. The porous support is formed by demixing and phase separation of polymer solution in the water bath. Therefore, a desirable asymmetric morphology is formed, comprising a dense selective layer giving good membrane separation performance and a porous support structure providing mechanical support and good pressure resistance.

After phase-separation in the water quench bath, the fibers gain mechanical strength and are collected by a take-up drum before water soaking and solvent-exchange. Water soaking removes residual organic solvents (e.g., NMP and THF) from the polymer hollow fiber. The solvent exchange conditions must be carefully chosen to maintain the hollow fiber porous substructure.[153] Water evaporation (surface tension ~ 72 mN/m) from small pores in the porous substructure could produce high capillary force[154], leading to partial densification of the porous substructure and reduced membrane permeance. Hence, water inside the pores of nascent hollow fibers is typically removed by exchange with solvent with lower surface tension (methanol followed by hexane) prior to drying.

2.4.2 Controlling properties of asymmetric precursor and CMS hollow fiber membranes

The separation performance of asymmetric hollow fiber membranes are largely affected by their skin integrity, selective skin layer thickness, substructure transport resistance, and macroscopic properties.[74] Skin integrity is among the most important property of asymmetric hollow fiber membranes. The thin selective layer is responsible for the separation, while the porous substructure is non-selective and serves as the support to provide mechanical strength. Therefore, defect-free skin layer is critical in asymmetric hollow fiber membranes. Defect-free membranes are usually defined as membranes that show at least 90% of the intrinsic selectivity obtained in the dense film membranes.[155] Previous studies showed that fabricating defect-free precursor polymer hollow fiber membranes is very important for producing high-performance asymmetric CMS hollow fiber membranes.[74]

According to equation 2.3, separation layer thickness affects the membrane permeance. For the same membrane material, a defect-free thin separation layer is always desirable because it can provide high permeance. As the separation layer becomes thinner, defects are more likely to form. Commercial membrane manufacturers can produce nearly defect-free membranes with skin layer less than 100 nm.[156] However, formation of sub-100nm defect-free separation layers in academic lab conditions is usually more difficult.

The substructure resistance in asymmetric gas separation membranes needs to be characterized in addition to skin integrity and separation layer thickness.[156] Gas permeation is ideally dominated by the dense skin layer with negligible resistance from the membrane substructure. With the reducing skin layer thickness of asymmetric hollow fiber membranes, the substructure resistance becomes an increasingly significant factor in contributing to the overall gas permeation flow rate. The substructure resistance in asymmetric carbon hollow fiber membranes could originate from porous substrate densification during pyrolysis, leading to significant gas permeance reduction. To obtain negligible substructure resistance as well as thin separation layers in asymmetric carbon hollow fiber membranes, substructure collapse must be prevented during the intense heat treatment.

Finally, the macroscopic properties of asymmetric membranes are also considered. Hollow fibers with smaller diameters are preferred due to their higher surface area to volume ratio and higher pressure tolerance.[148] Previous work showed CMS hollow fibers exhibited pressure resistance up to 1500 psi.[65] The outer diameter of hollow fibers determines the packing density of hollow fiber module. The inner

diameter of the hollow fiber is usually designed to be half of the outer diameter. Several undesirable macroscopic morphologies can negatively affect the mechanical strength of the hollow fiber membrane, including non-concentric bore, oval shape, and macrovoids. The non-concentric bore is caused by spinneret channel misalignment. The oval shape is formed due to insufficient phase separation rate in the water quench bath. The formation of macrovoids is a complicated process and is mainly related to phase separation kinetics. Macrovoids could be avoided by using increasing polymer concentration or draw ratio.[148, 151]

Chapter 3: Materials and experimental methods

3.1 Overview

This chapter describes the materials and experimental methods used in this PhD work. Section 3.1 presents the chemicals and gases used for membrane preparation, permeation measurement, and reaction measurement. Section 3.2 discusses the fabrication processes of polymer and CMS membranes including both dense film and hollow fiber format. Section 3.3 presents hollow fiber membrane module construction process. Section 3.4 shows the gas permeation systems as well as characterization techniques for membrane and catalyst. The last Section 3.5 discusses the reaction systems for packed bed reactor and membrane reactor measurements. The catalyst stability analysis and PDH equilibrium conversion calculation are also provided.

3.2 Materials

3.2.1 Chemicals

Matrimid® 5218 polyimide was provided by Huntsman Corporation (Salt Lake City, UT) and used as the polymer precursor material for CMS membrane formation. N-Methyl-2-pyrrolidone (NMP, anhydrous, 99.5%), tetrahydrofuran (THF, anhydrous, 99.5%), ethanol (anhydrous, 99.5%) were obtained from Sigma Aldrich (St. Louis, MO), which were used as solvents and non-solvents for polymer solution preparation. Methanol (99.8% ACS, VWR Chemicals BDH®) and hexane (98.5% ACS, Fisher Chemical) were used for polymer precursor hollow fiber solvent exchange. Vinyltrimethoxysilane (VTMS, 97%) and hexane (mixture of isomers, anhydrous,

99%) were obtained from Sigma Aldrich (St. Louis, MO), which were used for precursor hollow fiber silane treatment. All chemicals were used as received. The PDH catalyst, platinum-zinc supported on silicalite-1 (Pt-Zn/S1), was synthesized by Antara Bhowmick from Dr. Dongxia Liu's group.

3.2.2 Gases

Gases are mainly used for sorption, permeation, and reaction tests. The gases He, H_2, CO_2, Ar, N_2, and C_3H_6 were obtained from Airgas. C_3H_8 was purchased from Praxair. The purity of each gas is listed in **Table 3.1**. The molecular size of a gas molecule is usually represented by kinetic diameter (based on minimum cross-sectional diameter) or collision diameter (calculated from Lennard-Jones potential). Kinetic diameters are often used for light gases such as He, H_2, CO_2, Ar, and N_2, while Lennard-Jones diameters are provided for hydrocarbons [157]. The molecular size and critical temperature are also summarized in **Table 3.1.**

Table 3.1. Purity, molecular size, and critical temperature of gases used in this work.

Gases	Purity (%)	Diameter (Å)	Critical temperature (K)
He	99.999	2.6	5
H_2	99.999	2.89	33
CO_2	99.999	3.30	304
Ar	99.999	3.40	151
N_2	99.999	3.64	126
C_3H_6	99.5	4.68	365
C_3H_8	≥99.99	5.06	370

3.3 Membrane formation

3.3.1 Formation of polymer membranes

3.3.1.1 Formation of polymer dense films

Polymer dense films were formed by solution casting as reported in previous work.[72, 158] The Matrimid® powder was first dried at 110 ºC under vacuum for 12 hours to remove moisture. Dried Matrimid® powders were dissolved in THF to prepare a 20 wt% polymer solution in a 40 mL ICHEM vial (Fisher Scientific), which was placed on a roller overnight to become homogenous. A glass plate with Siliclad® (Geleste Inc.) treated surface was used as the film casting support. The glass surface after Siliclad® treatment has higher hydrophobicity, making the removal of nascent polymer dense film much easier. The casting was carried out inside a glove bag (Glas-Col, Terre Haute, IN), which contained the polymer solution vial, a leveled glass plate, a casting knife (BYK, 20 mil), and two jars of THF. The glove bag was sealed and purged with nitrogen three times. After the glove bag was saturated by THF in three hours, the polymer solution was poured across the front edge of the casting knife. A nascent polymer film was obtained by pulling the casting knife downward (**Figure 3.1**). Following overnight solvent evaporation, the polymer film was removed from the glass plate and dried under vacuum at 110 ºC for 12 hours to remove any residual solvent.

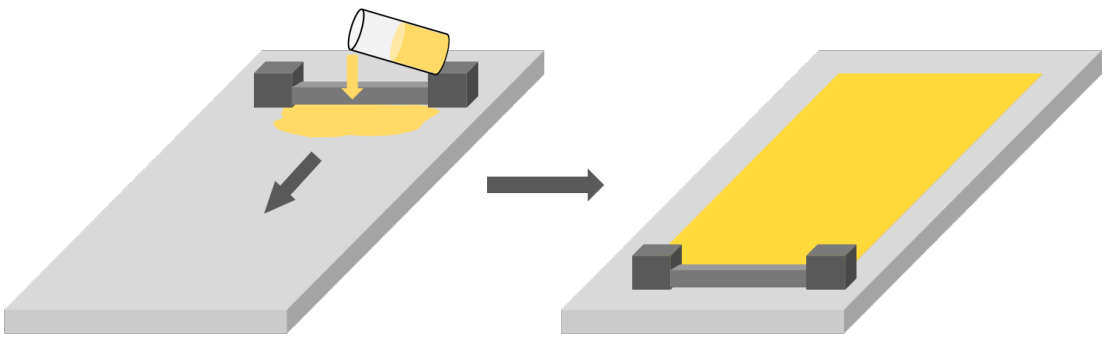

Figure 3.1. Schematic drawing of the solution casting method for polymer dense film preparation.

3.2.1.2 Formation of asymmetric polymer hollow fiber membranes

Spinning dope composition is crucial to fabrication of defect-free hollow fiber membranes.[155, 159] The dope typically consists of polymer, solvents, and non-solvents. The ratio of solvents to non-solvents should be adjusted to keep the dope in the one-phase region while staying close to the bimodal line for fast phase separation in the water bath. The ternary phase diagram provided in Chapter 2 Section 2.3 shows the dope composition trajectory during spinning. As water is the preferred quench bath medium, the solvents and non-solvents in the dope are selected with good water miscibility.

The polymer dope composition used in this work is shown in **Table 3.2**.[147] N-Methyl-2-pyrrolidone (NMP) was chosen as the non-volatile solvent due to its strong interaction with the polymer Matrimid® 5218, good water miscibility, and ecofriendliness. Tetrahydrofuran (THF) was chosen as the volatile solvent to assist the dense skin layer formation in the air gap. Ethanol was used as a non-solvent to bring the dope composition close to the bimodal line for rapid phase separation in water. Compared to other strong non-solvents like water, ethanol is a weak non-solvent that enables a wide window for tuning dope formulation. Additionally, the high volatility of ethanol promotes dense skin layer formation during the air gap. Additives such lithium nitrate ($LiNO_3$) were sometimes added to the dope to build up solution viscosity, assist phase separation, and promote pore formation.

Table 3.2. Spinning dope compositions of Matrimid® precursor hollow fiber membranes.[147]

Component	wt%
Matrimid® 5218	26.2
N-Methyl-2-pyrrolidone	53
Tetrahydrofuran	5.9
Ethanol	14.9

Monolithic Matrimid® precursor hollow fiber membranes were fabricated using the dry-jet/wet-quench fiber spinning technique with a custom-built hollow fiber spinning system.[160] Matrimid® 5218 polyimide powder was dried under vacuum at 110 ºC for 15 hours for moisture removal. The spinning dope (**Table 3.2**), contained in a Qorpak® glass bottle sealed with Teflon® cap, was placed on a roller until a homogenous dope was obtained. The polymer dissolving process may take 1-2 weeks and sometimes heat was applied to accelerate the dissolving process for highly viscous dopes.

The homogenous dope was loaded into a 1000-mL syringe pump (ISCO Inc., Lincoln, NE) and degassed at spinning temperature (60 ºC) overnight. The bore fluid was loaded into a separate 500-mL syringe pump. The dope and bore fluid were co-extruded through a spinneret with in-line filters (60 microns) between the syringe pump and spinneret. The temperatures of the dope pump, dope line, and spinneret were controlled by separate heating tapes and thermocouples. The extruded dope along with the bore fluid went through the air gap and entered the water quench bath. The phase-separated fibers passed through a Teflon® guide and were finally collected on a 0.32 m

diameter rotating polyethylene drum. The rotating speed of the take-up drum can be adjusted to control the fiber dimension. The spinning parameters were summarized in **Table 3.3**.

After cutting from the take-up drum, the as-spun precursor hollow fiber membranes were soaked in three separate deionized water baths over the course of 72 hours and solvent exchanged with three separate 20 min methanol baths followed by three 20 min hexane baths. After being dried in a fume hood overnight, the polymer precursor hollow fibers were dried under vacuum at 75 ^{o}C for 12 hours to remove any residue solvent.

Table 3.3. Spinning parameters of Matrimid® precursor hollow fiber membranes.[104]

Spinning parameter	Value
Spinning temperature (^{o}C)	60
Quench bath temperature (^{o}C)	50
Dope flow rate (cc/hr)	180
Bore fluid* flow rate (cc/hr)	60
Air gap height (cm)	10
Fiber take-up rate (m/min)	20

*Bore fluid: 90% NMP/10% water

3.3.2 Silane pretreatment of polymer precursor hollow fiber membranes

The polymer precursor hollow fibers were treated by vinyltrimethoxysilane (VTMS) to resist membrane porous substrate collapse during pyrolysis.[89] The precursor hollow fibers were soaked in a 10 wt% VTMS/hexane solution for 24 hours and then exposed to water-vapor saturated air for another 24 hours at room temperature. The VTMS-treated precursor hollow fibers were vacuum dried at 150 ^{o}C for 12 hours prior to pyrolysis. The sol-gel crosslinking reaction between VTMS and moisture forms vinyl crosslinked silica on the precursor fiber pore walls. The formed silica network can effectively prevent membrane substrate collapse during pyrolysis, thereby providing a thin separation layer (usually < 10 μm) in CMS hollow fiber membranes.

3.3.3 Formation of CMS membranes

3.3.3.1 Pyrolysis set-up

The pyrolysis set-up was similar to a configuration reported in literature (**Figure 3.2**).[61, 149] A three-zone tube furnace (MTI Corporation, Richmond, CA) was used to provide external heating for pyrolysis. The tube furnace temperature was controlled by a multi-channel temperature controller, where three thermocouples were independently connected to three channels of controller, providing a uniform temperature distribution inside the quartz tube. The assembly of a metal flange with silicon O-rings was used to provide sealing on both ends of the quartz tube. A mass flow controller (MTI Corporation, Richmond, CA) was used to accurately control the inert purge gas flow rate. The oxygen level in the pyrolysis system was monitored by an oxygen analyzer (Cambridge Sensotec, Rapidox 2100 series, Saint Ives, UK).

The fabrication of CMS dense films, straight or U-shape CMS hollow fibers shares the same pyrolysis set-up. A quartz plate [144] with 2 mm deep and 2 mm slots (United Silica Products, Franklin, NJ) was used as the support for CMS dense film pyrolysis (**Figure 3.3 A**). A stainless-steel wired mesh plate (McMaster Carr, Robbinsville, NJ) was used as the support for straight CMS hollow fiber pyrolysis. The stainless-steel wires were loosely threaded through the holes to secure the fiber position along the plate (**Figure 3.3 B**). A 1/4-inch U-shape quartz tube was used to hold the polymer precursor fibers for the fabrication of U-shape CMS hollow fibers (**Figure 3.3 C**).

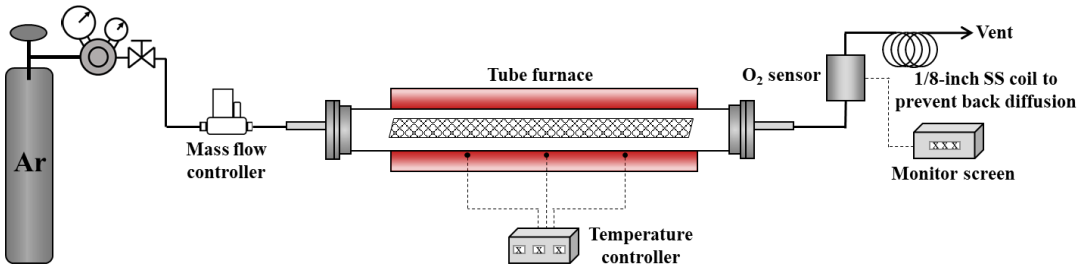

Figure 3.2. Schematic drawing of the pyrolysis set-up for CMS membranes formation.

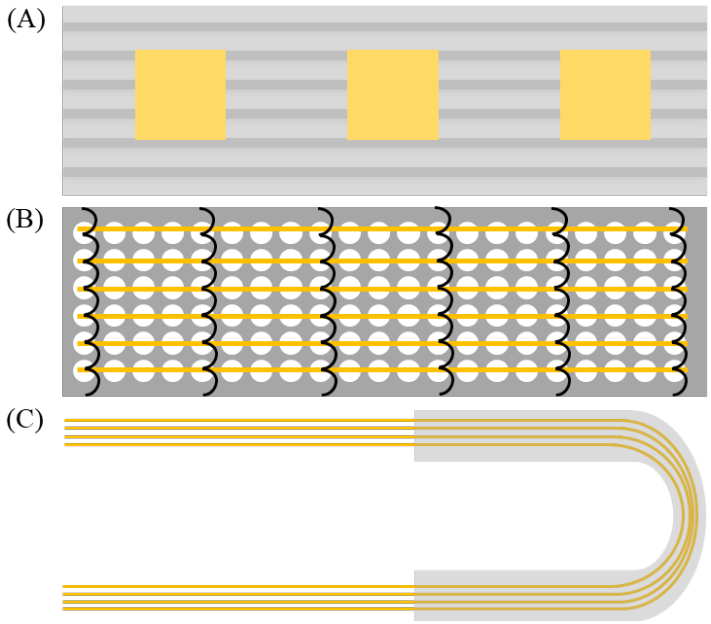

Figure 3.3. Schematic representation of (A) a quartz plate used as dense films support, (B) a wired stainless-steel mesh plate used as straight hollow fibers support, and (C) U-shape 1/4-inch quartz tube with polymer hollow fibers inserted to produce U-shape CMS hollow fibers.

3.3.3.2 Pyrolysis protocol

The asymmetric CMS hollow fiber membranes were formed by pyrolyzing VTMS-treated precursor hollow fibers in the three-zone tube furnace. The precursor hollow fibers were placed on the stainless-steel wire mesh in a quartz tube and then loaded into the furnace. Heating was started after the oxygen level in the system drops to below 5 ppm prior after overnight purging with ultra-high purity (UHP) argon at 200 cc/min. The heating protocol below was used for pyrolysis:

1) Room temperature to 250 ^{o}C, 13.3 ^{o}C/min

2) 250 to T_{final}-15, 3.85 ^{o}C/min (T_{final}= 550, 675, or 800 ^{o}C)

3) T_{final}-15 to T_{final}, 0.25 ^{o}C/min

4) Isothermal soaking at T_{final} for 2 hours

5) Cooling down naturally to room temperature

After the heating cycle was finished, the tube furnace cooled down naturally while maintaining the UHP argon purging. The CMS samples were removed once the temperature drops to below 50 ^{o}C. After each pyrolysis, the quartz tube and stainless-steel plate were rinsed with acetone followed by baking in the air at 800 ^{o}C for 2 hours. This cleaning protocol was to remove deposited residues so that the next pyrolysis

would not be affected. The preparation of CMS dense films shares the same heating protocol.

3.4 Hollow fiber membrane module construction

Asymmetric CMS hollow fiber membranes were potted into lab-scale membrane modules for permeation test. The hollow fiber membrane module was constructed following a similar procedure described in literature.[95] In this work, quartz tube (Quartz Scientific Inc. Fairport Harbor, OH) and stainless steel ultratorr fittings (Swagelok, Solon, OH) were used for the module construction. Epoxy (3M^{TM} Scotch-Weld^{TM} DP-100) was used as sealing materials.

Depending on the quartz tube format, either a straight (**Figure 3.4**) or a U-shape hollow fiber membrane module (**Figure 3.5**) was constructed. The straight membrane module was used for most permeation tests while the U-shape membrane module was used in the membrane reactor tests with catalysts loaded to the fiber shell side. The Epoxy-sealed module connections were kept outside the furnace and exposed to ambient conditions during high-temperature permeation or reaction and the temperature of the module Epoxy portion was below 50 ^{o}C.

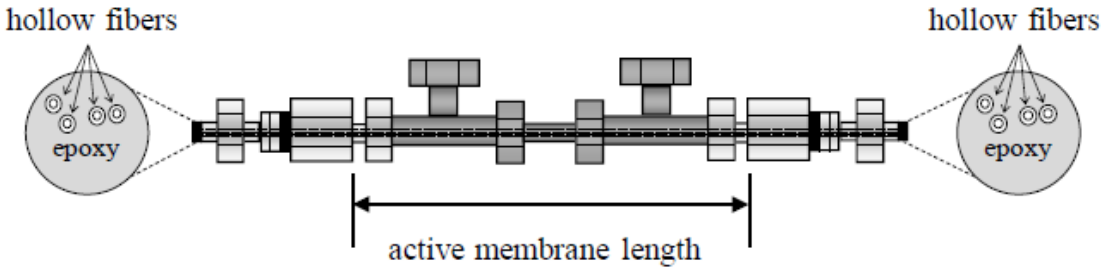

Figure 3.4. Schematic drawing of a lab-scale straight hollow fiber membrane module.[74]

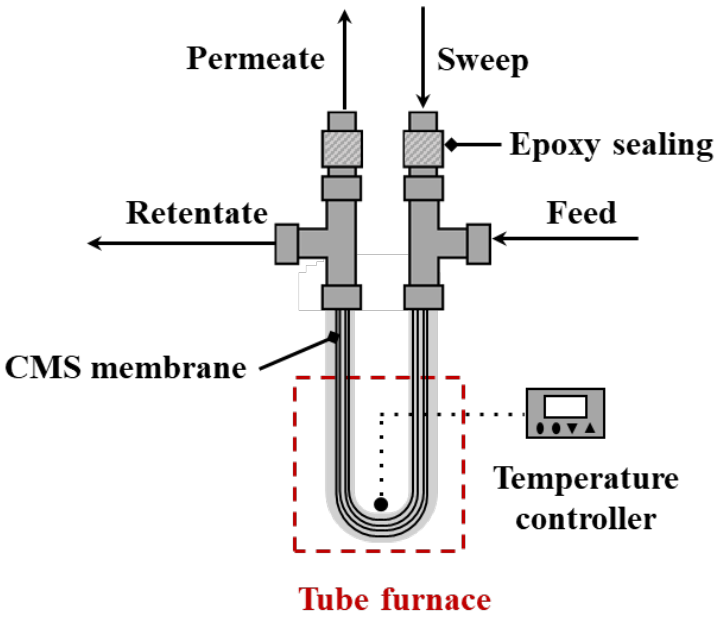

Figure 3.5. Schematic drawing of a lab-scale U-shape hollow fiber membrane module.

3.5 Membrane and catalyst characterization

3.5.1 Membrane pure gas permeation measurements at ambient temperature

Pure gas permeation measurements of CMS hollow fiber membrane modules were carried out using a constant-pressure permeation system following procedures described in literature (**Figure 3.6**).[147, 155] The measurements were taken at room temperature using bore-side feed at 14.5 psig with permeate (shell side) at atmospheric pressure. Ater 20 mins stabilization, the gas permeation rate was measured using a soap film flowmeter (Hewlett Packard, 100 mL). The CMS hollow fiber membrane performance was then quantified by ideal selectivity and gas permeance.

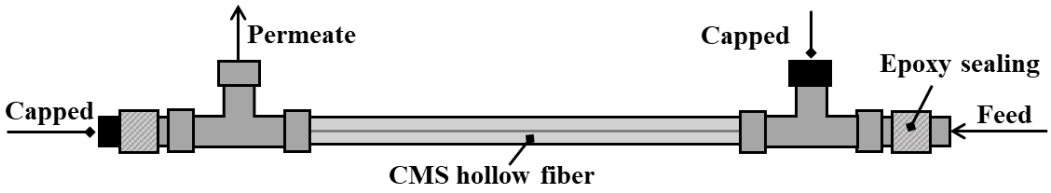

Figure 3.6. Schematics showing the constant-pressure permeation setup.

3.5.2 Membrane mixed-gas permeation measurements at high temperature

To evaluate practical H_2/C_3H_8 separation performance of CMS hollow fiber membranes under PDH reaction temperature, a custom high-temperature permeation system (**Figure 3.7**) was designed and constructed in this research.[149] The desired permeation temperature was achieved by heating up the quartz tube portion of the hollow fiber module by a 14-cm single-zone tube furnace (DS Fibertech Corporation, Santee, CA). During the temperature ramping, N_2 was introduced to hollow fiber shell and bore sides to prevent membrane decomposition. Once the temperature reached the target value, a H_2/C_3H_8 feed mixture (1 bar, 30 cc/min) was introduced to the hollow fiber shell side while N_2 sweep gas (10 cc/min) was introduced to the hollow fiber bore side. Permeate flow rate was measured using a bubble flow meter and permeate compositions were analyzed by an Agilent-6890 gas chromatograph (GC). A thermal conductivity detector (TCD) and a packed column (HayeSep DB, Agilent) were used for H_2 detection. A flame ionization detector (FID) and a capillary column (GS-GasPro, Agilent) were used for C_3H_8 detection. Permeation data were continuously collected until the GC readings became stabilized for at least three hours. Each permeation measurement was run for a minimum of 24 hours.

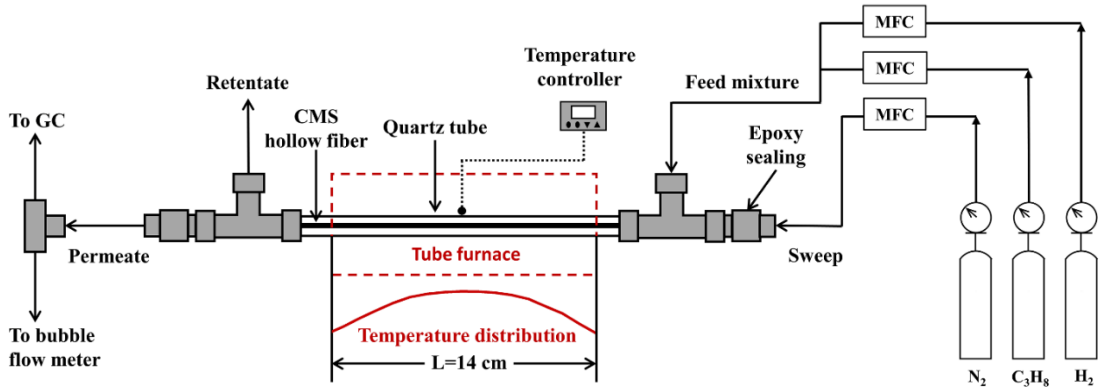

Figure 3.7. Schematic illustration of the high-temperature H_2/C_3H_8 permeation system. (MFC: mass flow controller).

Since heating provided by the single-zone furnace was not uniform (**Figure 3.7**), average permeances and average separation factors were obtained by the permeation measurements. As the module temperature dramatically drops outside the furnace and membrane permeance drops exponentially with temperature (Eqn. 3.1), only permeation from the hollow fiber module inside the furnace was considered for permeance calculations. The measured average permeances were used to calculate apparent permeation activation energies.

$$P_{i,average} = \frac{1}{L}\int_{-\frac{L}{2}}^{\frac{L}{2}} P_{0i}\exp\left(\frac{E_{P,i}}{RT(z)}\right)dz \tag{3.1}$$

where $P_{i,average}$ is the measured average permeance of component i, $T(z)$ is the measured temperature distribution profile, L is furnace length ($L = 14$ cm) and z is location ($z = 0$ cm at the center of furnace). With the average permeances and temperature distribution profiles measured at different furnace set temperatures, the apparent permeation activation energies can be calculated by the least squares method.

3.5.3 Morphology and structure characterizations

3.5.3.1 Scanning electron microscopy (SEM)

SEM was used to characterize the morphology of asymmetric polymer precursor hollow fibers and the CMS hollow fiber membranes. XEIA3 TESCAN scanning electron microscope at the University of Maryland NanoCenter AIM Lab with an operating voltage of 10 kV was used. All hollow fiber samples were coated with Au particles before SEM.

3.5.3.2 CO_2 physisorption

CO_2 physisorption isotherms (273.15 K) in CMS dense films were measured using an ASAP 2020PLUS physisorption analyzer (Micromeritics, Norcross, GA). MicroActive (Micromeritics, Norcross, GA) was used to analyze the collected CO_2 isotherms. A density functional theory (DFT) model (CO_2, 273.15K, slit pores) was applied to calculate the pore size distribution, pore surface area, and pore volume.

3.5.3.3 Thermogravimetric analysis (TGA)

Thermogravimetric analysis (TGA) was performed on fresh and spent catalysts to determine the coke formation rate during PDH membrane reactor tests. A thermogravimetric analyzer (Shimazu, TGA 50) was used. A heating rate of 5 ^oC/min was used to reach target temperature 800 ^oC and the samples were kept at 800 ^oC for 30 minutes under 50 ml/min air purge.

3.6 Reaction measurements

3.6.1 Propane dehydrogenation in packed bed reactor

Non-oxidative dehydrogenation of propane was performed over the Pt-Zn/S1 catalyst in a packed bed reactor (PBR) shown in **Figure 3.8.** A U-shape quartz tube and two ultratorr tees were used for PBR construction in this work to keep the reactor design consistent. Prior to the reaction tests, the catalyst was pretreated in a H_2/N_2 mixture gas (20 mL min^{-1}, H_2/N_2 =1:5) at 500 °C (0.0167 °C s^{-1}) for 3 h. After that, the system was flushed with argon (20 mL min^{-1}, 1 hour) to get rid of H_2 in the reactor. When the temperature reached the target reaction temperature, the feed gas flow was switched to propane mixed with the Ar internal standard to start the dehydrogenation reaction test. The propane conversion ($\chi_{C_3H_8}$), propylene product selectivity ($S_{C_3H_6}$) and yield ($Y_{C_3H_6}$) were calculated by the following equations,

$$\chi_{C_3H_8}(\%) = \frac{F_{C_3H_8}^{in} - F_{C_3H_8}^{out}}{F_{C_3H_8}^{in}} \times 100\% \quad (3.2)$$

$$S_{C_3H_6}(\%) = \frac{F_{C_3H_6}}{F_{C_3H_8}^{in} - F_{C_3H_8}^{out}} \times 100\% \quad (3.3)$$

$$Y_{C_3H_6}(\%) = \frac{\chi_{C_3H_8} \times S_{C_3H_6}}{100} \quad (3.4)$$

where $F_{C_3H_8}^{in}$, $F_{C_3H_8}^{out}$, and $F_{C_3H_6}$ are the propane flow rates at the inlet and outlet of the reactor, and propylene product flow rate at the reactor outlet, respectively. The dehydrogenation reaction in the PBR in the absence of catalyst was tested at the same conditions. The reaction due to gas phase chemistry was negligible at the studied reaction conditions.

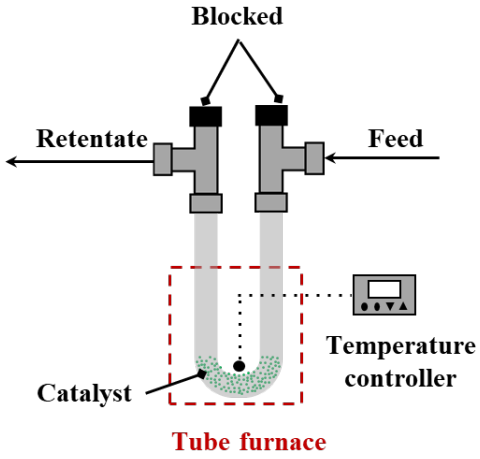

Figure 3.8. Schematics of packed bed reactor for PDH tests.

3.6.2 Propane dehydrogenation in CMS membrane reactor

The CMS hollow fiber membrane reactor was assembled by packing Pt-Zn/S1 catalyst particles on the shell side (outside) of CMS hollow fiber membranes. Prior to the reaction test, the membrane reactor system (**Figure 3.9**) was flushed with argon (20 mL min^{-1}) overnight. Then the argon gas flow in the shell side was switched to the H_2/N_2 mixture gas (20 mL min^{-1}, H_2/N_2 =1:5) to pretreat the catalyst at 500 °C (0.0167 °C s^{-1}) for 3 h. After that, the H_2/N_2 gas flow in the shell side was switched back to argon flow to flush out the residue H_2 gas in the membrane reactor system. When the temperature reached target reaction temperature, the argon flow was switched to propane (C_3H_8) mixed with argon internal standard to start the dehydrogenation reaction. The bore side of the membrane reactor was kept with argon flow in all these catalyst pretreatment and catalysis testing steps.

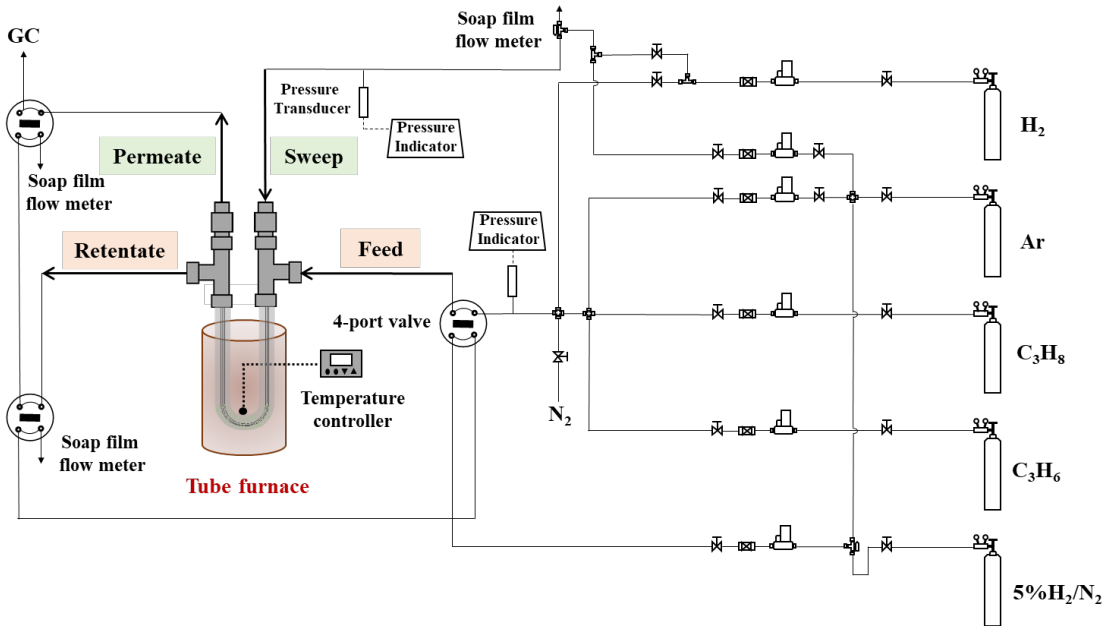

Figure 3.9. Schematic drawing of membrane reactor system for PDH tests.

The propane conversion and propylene selectivity in membrane reactor were calculated using the following equations,

$$\chi_{C_3H_8}(\%) = \frac{F^{in}_{C_3H_8} - \left(F^{out}_{C_3H_{8,shell}} + F^{out}_{C_3H_{8,bore}}\right)}{F^{in}_{C_3H_8}} \times 100\% \quad (3.5)$$

$$S_{C_3H_6}(\%) = \frac{\left(F_{C_3H_{6,shell}} + F_{C_3H_{6,bore}}\right)}{F^{in}_{C_3H_8} - \left(F^{out}_{C_3H_{8,shell}} + F^{out}_{C_3H_{8,bore}}\right)} \times 100\% \quad (3.6)$$

where $F^{out}_{C_3H_{8,shell}}$, $F^{out}_{C_3H_{8,bore}}$, $F_{C_3H_{6,shell}}$, and $F_{C_3H_{6,bore}}$ are the propane flow rates at the outlet of the shell and bore sides as well as propylene product flow rates at the outlet of the shell and bore sides of the reactor, respectively. The propylene yield in the MR was calculated using Eqn. 3.4. The dehydrogenation reaction in the MR in the absence of catalyst was tested at the same conditions. The reaction due to gas phase reactions was negligible at the studied reaction conditions.

3.6.3 Catalyst stability analysis in propane dehydrogenation

To quantify the stability (or deactivation behavior) of the catalyst in either PBR or MR conditions, the first-order deactivation kinetics was assumed to evaluate the deactivation coefficient of the catalyst in propane dehydrogenation. This method has been used to analyze the catalytic reactions on supported metal catalysts in the past.[12] The equation for calculating the deactivation coefficient (k_d) [161] has been reported previously, and is shown below,

$$k_d = \frac{ln\left(\frac{1-\chi_{C_3H_8}}{\chi_{C_3H_8}}\right) - ln\left(\frac{1-\chi^o_{C_3H_8}}{\chi^o_{C_3H_8}}\right)}{t} \quad (3.7)$$

where $\chi^o_{C_3H_8}$ is the initial (i.e., the moment that reaction reached steady state) propane conversion and $\chi_{C_3H_8}$ is the final propane conversion at time-on-stream (TOS) tests for a period of t (h).

3.6.4 Equilibrium conversion of propane dehydrogenation

The thermodynamic equilibrium conversion for propane dehydrogenation reaction ($C_3H_8 = C_3H_6 + H_2$) at the experimental testing conditions was calculated using the van't Hoff equation,

$$\frac{dlnK_{eq}}{dT} = \frac{\Delta H_r}{RT^2} \quad (3.8)$$

where K_{eq} is the equilibrium constant, T is the reaction temperature (K), ΔH_r is the enthalpy of reaction (kJ·mol^{-1}), and R is the gas constant (J·mol^{-1}·K^{-1}), respectively. ΔH_r depends on the reaction temperature as shown by the equations below,

$$\Delta H_r(T) = \Delta H_r^0 + \int_{T_0}^{T} \Delta C_{r,p}\, dT \tag{3.9}$$

$$C_p = A + BT + CT^2 + DT^3 \tag{3.10}$$

$$\Delta C_{r,p} = \Delta A + \Delta BT + \Delta CT^2 + \Delta DT^3 \tag{3.11}$$

in which ΔH_r^0 is the enthalpy of reaction at STP condition, T_0 is the ambient temperature (25 ºC), C_p is the constant pressure heat capacity ($J \cdot mol^{-1} \cdot K^{-1}$), A, B, C, and D are the coefficients in the calculation equation for C_p at different temperatures, and $\Delta C_{r,p}$ is the change of heat capacity due to a reaction. Substituting Eqn. 3.9 and Eqn. 3.11 into Eqn. 3.10,

$$\begin{aligned} &K_{eq}(T) \\ &= K_{eq}^0 \exp\left\{ \frac{\Delta H_r^0 - \left(\Delta A \cdot T_0 + \frac{\Delta B}{2} \cdot T_0^2 + \frac{\Delta C}{3} \cdot T_0^3 + \frac{\Delta D}{4} \cdot T_0^4\right)}{R} \cdot \left(\frac{1}{T_0} - \frac{1}{T}\right) \right. \\ &\left. + \frac{\Delta A \cdot \ln\left(\frac{T}{T_0}\right) + \frac{\Delta B}{2} \cdot (T - T_0) + \frac{\Delta C}{6} \cdot (T^2 - T_0^2) + \frac{\Delta D}{12} \cdot (T^3 - T_0^3)}{R} \right\} \end{aligned} \tag{3.12}$$

where K_{eq}^0 is the equilibrium constant at STP condition. The calculation for K_{eq}^0 is shown by the Eqn. 3.13-3.16 below,

$$K_{eq}^0 = \exp\left(-\frac{\Delta G_r^0}{RT_0}\right) \tag{3.13}$$

$$\Delta G_r^0 = \Delta H_r^0 - T_0 \Delta S_r^0 \tag{3.14}$$

$$\Delta H_r^0 = \sum_i \nu_i\, \Delta H_{i,f}^0 \tag{3.15}$$

$$\Delta S_r^0 = \sum_i \nu_i\, S_{i,f}^0 \tag{3.16}$$

where ΔG_r^0 is the standard Gibbs free energy of reaction, T_0 is standard temperature (298.15 K), ΔS_r^0 is the standard entropy of reaction, ν_i is the stoichiometric coefficient of species i. $\Delta H_{i,f}^0$ and $S_{i,f}^0$ stands for standard enthalpy of formation and standard entropy of formation of compound i, respectively. **Table 3.4** lists the corresponding thermodynamic data used for the equilibrium conversion calculations for propane dehydration reaction.[162]

Table 3.4. Thermodynamic data at STP condition for equilibrium conversion calculations for propane dehydrogenation reaction.

Gas	$\mathbf{\Delta H_f^0}$ $(\frac{\text{kJ}}{\text{mol}})$	$\mathbf{S_f^0}$ $(\frac{\text{J}}{\text{mol·K}})$	**A** $(\frac{\text{J}}{\text{mol·K}})$	**B** $(\frac{\text{J}}{\text{mol·K}^2})$	**C** $(\frac{\text{J}}{\text{mol·K}^3})$	**D** $(\frac{\text{J}}{\text{mol·K}^4})$
C_3H_8	-104.68	269.91	-4.22	0.31	-1.59×10^{-4}	3.22×10^{-8}
C_3H_6	19.71	266.90	3.71	0.23	-1.16×10^{-4}	2.21×10^{-8}
H_2	0.00	131.00	27.14	0.01	-1.38×10^{-5}	7.65×10^{-9}

The reaction equilibrium constant (K_{eq}) at a fixed reaction equilibrium condition can also be expressed from the reaction compositions,

$$K_{eq} = \prod_i \left(\frac{p_i}{p^0}\right)^{\nu_i} = \frac{a\chi_{C_3H_8}^{eqbm^2}}{\left(1-\chi_{C_3H_8}^{eqbm}\right)\left(1+a\chi_{C_3H_8}^{eqbm}\right)} \tag{3.17}$$

where p_i is the partial pressure of gas species i, p^0 is the standard pressure (1 atm), a is the propane fraction in the feed stream (balanced by Ar internal standard), $\chi_{C_3H_8}^{eqbm}$ is

the thermodynamic equilibrium conversion. Then, $\chi_{C_3H_8}^{eqbm}$ can be calculated using the following equation,

$$\chi_{C_3H_8}^{eqbm} = \frac{K_{eq}(a-1) + \sqrt{\left(K_{eq}(1-a)\right)^2 + 4a\left(1+K_{eq}\right)K_{eq}}}{2a(1+K_{eq})} \times 100\% \quad (3.18)$$

H_2 removal ratio (y) is introduced to calculate the thermodynamic conversion with H_2 elimination from the shell side of the MR:

$$\chi_{C_3H_8}^{eqbm} = \frac{K_{eq}(a(1-y)-1) + \sqrt{\left(K_{eq}(1-a(1-y))\right)^2 + 4a(1-y)\left(1+K_{eq}\right)K_{eq}}}{2a(1+K_{eq})(1-y)} \times 100\% \quad (3.19)$$

When *y* equals 0, it is equilibrium conversion in PBR. Take T=450 ºC, 50 kPa C_3H_8/50 kPa Ar (*a*=0.5) as an example, **Table 3.5** shows the effect of H_2 removal percentage on equilibrium conversion.

Table 3.5. Corresponding PDH equilibrium conversion with different H_2 removal percentages.

H_2 removal percentage (%)	0	20	40	60	80	90	95	99
PDH equilibrium conversion (%)	12.4	14.1	16.0	19.0	25.5	33.7	43.7	70.4

The conversion in propane dehydrogenation in the MR condition was compared to the equilibrium conversion by calculating the conversion enhancement using,

$$Conversion/Eqbm.Conversion = \frac{\chi_{C_3H_8}}{\chi_{C_3H_8}^{eqbm}} \times 100\% \quad (3.20)$$

Chapter 4: Investigation of high-temperature H_2/C_3H_8 separation in CMS hollow fiber membranes

4.1 Overview

Catalytic propane dehydrogenation membrane reactors require membranes with highly attractive high-temperature H_2/C_3H_8 separation performance. In this chapter, polyimide-derived asymmetric carbon molecular sieve (CMS) hollow fiber membranes with thin (~5 μm) separation layers were studied for high-temperature (up to 600 ºC) H_2/C_3H_8 separation. Section 4.2 describes the roles of CMS membrane pyrolysis conditions on H_2/C_3H_8 separation performance. Section 4.3 discusses the effects of permeation temperature on high-temperature H_2/C_3H_8 separation. The Arrhenius equation was used to calculate CMS membrane intrinsic permeation properties using measured average permeances. Section 4.4 studies the impacts of feed composition on high-temperature H_2/C_3H_8 separation performance. The effects of high-temperature H_2 and C_3H_6 exposure on CMS pore structure and transport properties were investigated. Section 4.5 demonstrates the stability of CMS membrane under a continuous ~130-hour high-temperature (600 ºC) permeation test. Section 4.6 studies high-temperature $H_2/C_3H_6/C_3H_8$ ternary mixture permeation in CMS hollow fiber membranes. Section 4.7 summarizes the main findings of this chapter.

4.2 Effects of pyrolysis temperature on CMS membrane performance

Membrane reactors require membranes with a balance of attractive permeance and separation factor. While high permeances are useful to provide enhanced conversion, good separation factors are needed to minimize reactant loss. The effects of pyrolysis temperature on controlling high-temperature H_2/C_3H_8 separation performance of CMS hollow fiber membranes were investigated. Monolithic Matrimid® precursor hollow fibers were fabricated using dry-jet/wet-quench fiber spinning as described in Section 3.2.1.2 of Chapter 3. The separation properties of polymer precursor hollow fiber membranes were evaluated by single-gas permeation test. The precursor membrane showed helium (He) permeance ~45 GPU with He/N_2 selectivity of 72, indicating the precursor hollow fibers were defect-free.

Following the silane treatment (Section 3.3.2) of Matrimid® precursor hollow fibers, asymmetric CMS hollow fiber membranes were formed by pyrolysis at 550, 675, and 800 ^oC, respectively. The asymmetric polymer hollow fiber membrane had an outer diameter of 415 μm and a sub-micron dense separation layer on top of a porous substrate (**Figure 4.1**). After pyrolysis, the outer diameter of the asymmetric CMS hollow fiber membranes decreased to 265 μm with a ~ 5 μm dense separation layer on top of the porous substrate (**Figure 4.2**).

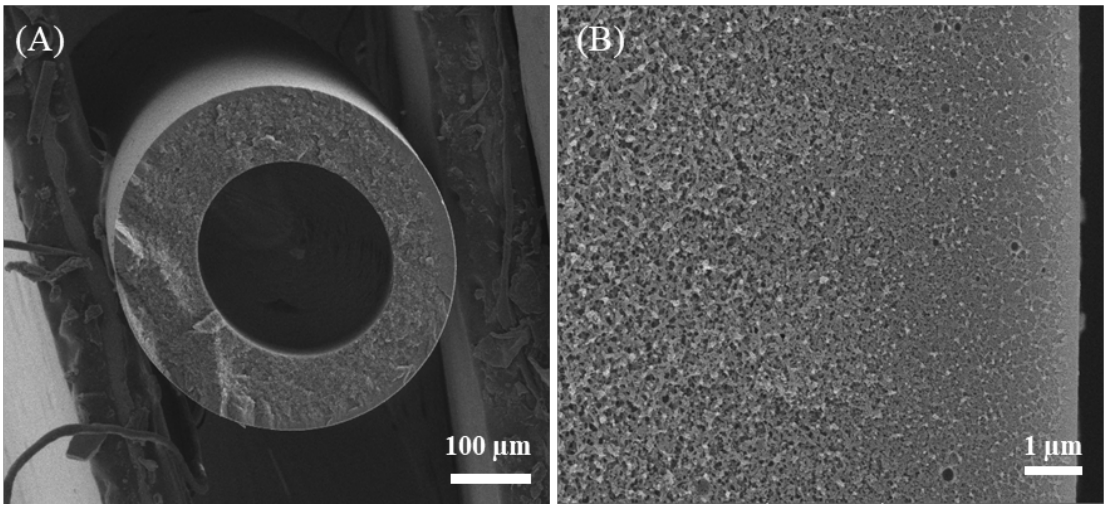

Figure 4.1. SEM images of Matrimid® precursor hollow fiber membranes. (A) hollow fiber overview and (B) cross-section near shell side.

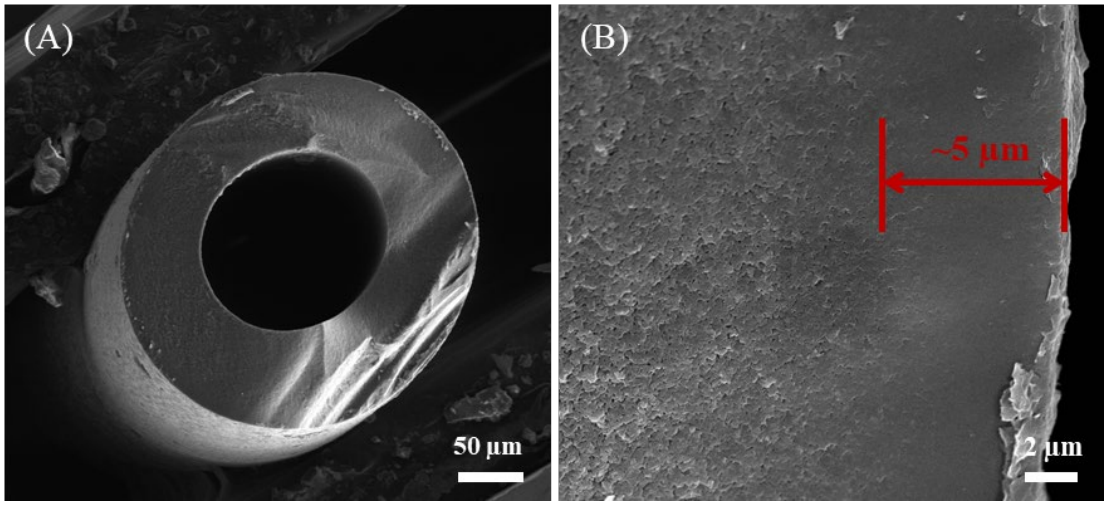

Figure 4.2. SEM images of Matrimid®-derived asymmetric CMS hollow fiber membranes. (A) hollow fiber overview and (B) cross-section near shell side.

The H_2/C_3H_8 separation performance (**Figure 4.3**) of CMS hollow fiber membranes was measured at 600 °C (furnace set temperature) using a 50%/50% H_2/C_3H_8 feed mixture at 1 bar. As the pyrolysis temperature increased from 550 to 800 °C, the H_2/C_3H_8 separation factor increased by more than two orders of magnitude from 130 to 35177 with only ~68% drop in H_2 permeance (**Figure 4.3 D**). Previous studies show that CMS ultramicropores are refined as the pyrolysis temperature increases[61], which is presumably responsible for the dramatically increased H_2/C_3H_8 separation factor. The refined ultramicropores can increase diffusion selectivity via enhancing molecule size discrimination (C_3H_8 kinetic diameter~4.3 Å vs H_2 kinetic diameter~2.9 Å). In addition, finer ultramicropores can increase sorption selectivity by exclusion of bulkier C_3H_8 molecules.[71] While diffusion selectivity normally reduces with increasing permeation temperature,[163] such exclusion-mediated sorption selectivity is presumed to be independent of permeation temperature, and is possibly responsible for the ultra-high separation factors at 600 °C.

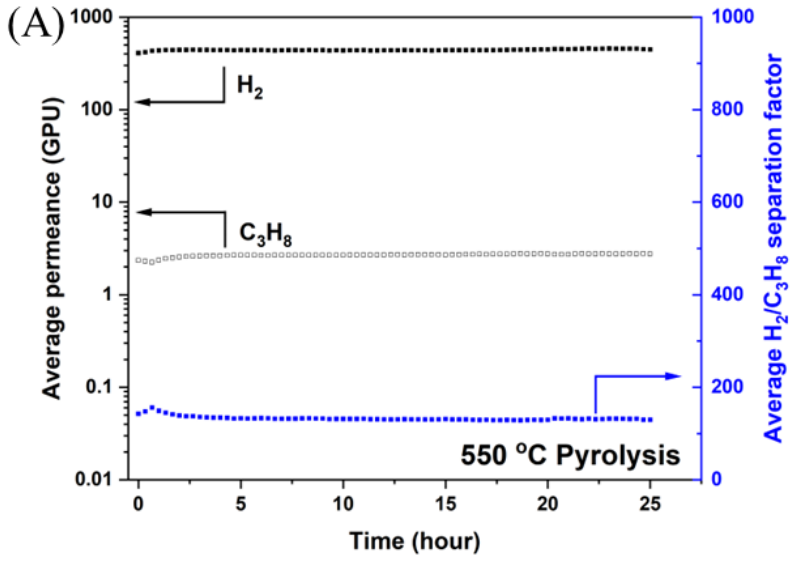

(B)

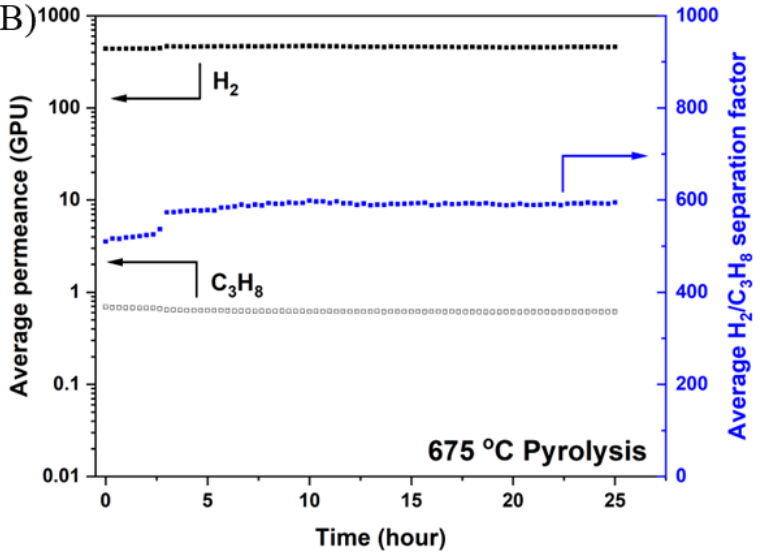
Average permeance (GPU)
Average H_2/C_3H_8 separation factor
H_2
C_3H_8
675 °C Pyrolysis
Time (hour)

(C)

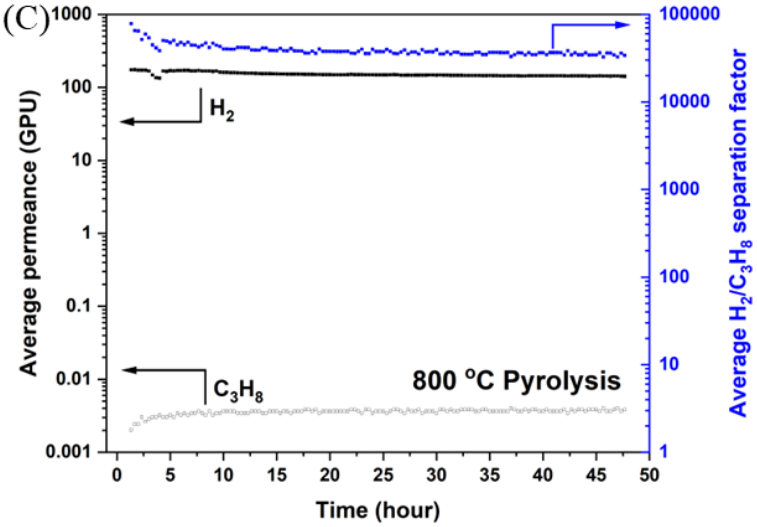
Average permeance (GPU)
Average H_2/C_3H_8 separation factor
H_2
C_3H_8
800 °C Pyrolysis
Time (hour)

(D)

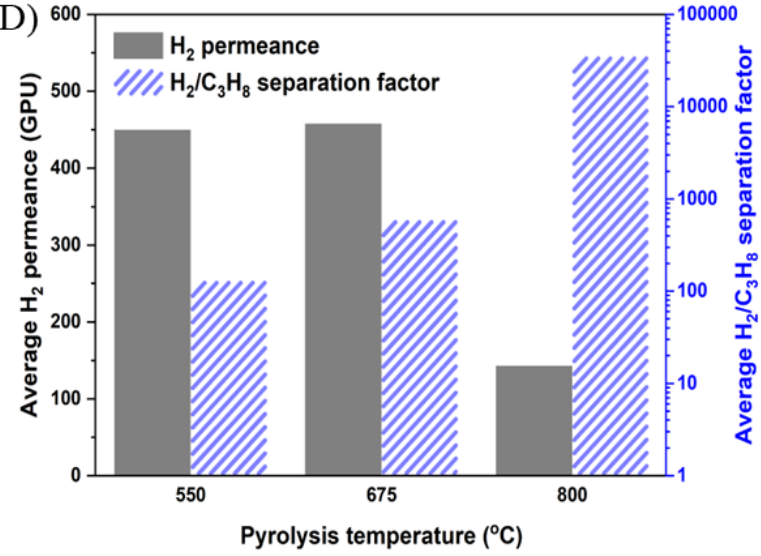
H_2 permeance
H_2/C_3H_8 separation factor
Average H_2 permeance (GPU)
Average H_2/C_3H_8 separation factor
Pyrolysis temperature (°C)

Figure 4.3. H_2/C_3H_8 separation performance of CMS hollow fiber membranes pyrolyzed at (A) 550 ^oC, (B) 675 ^oC, and (C) 800 ^oC; (D) Stabilized average permeances and separation factors. The permeation measurements were performed at 600 ^oC (furnace set temperature) using a 50%H_2/50%C_3H_8 feed mixture (1 bar).

C_3H_8 is much more condensable than H_2 (critical temperature: 369.5 K vs 32.9 K), and competition effects are expected to compromise H_2/C_3H_8 separation factors under mixture permeation. The competition effects were likely suppressed due to reduced sorption under high-temperature permeation at 600 ^oC, which enabled the attractive H_2/C_3H_8 separation factors shown in **Figure 4.3**. Notably, the CMS hollow fiber membranes pyrolyzed at 550 and 675 ^oC had almost identical H_2 permeances. This is possibly because the smaller H_2 molecules are in a highly activated state under 600 ^oC permeation and do not respond strongly to refining of the ultramicropores. Overall, the CMS hollow fiber membrane pyrolyzed at 675 ^oC provides a good balance between average H_2 permeance and average H_2/C_3H_8 separation factor and was chosen for more detailed studies on the effects of permeation temperature (Section 4.3) and feed composition (Section 4.4).

4.3 Effects of permeation temperature on CMS membrane performance

Temperatures of membrane reactors are often chosen to maximize catalyst selectivity and product yield. It is important to understand the effects of permeation temperature on membrane high-temperature separation performance. The CMS hollow fiber membrane pyrolyzed at 675 ^oC was studied for H_2/C_3H_8 mixture (50%/50%) permeation at furnace set temperatures of 400, 500, and 600 ^oC (**Figure 4.4**). As the temperature increased from 400 to 600 ^oC, the average H_2 permeance increased from 331 to 458 GPU while the average H_2/C_3H_8 separation factor decreased from 2127 to

591. It should be noted that the permeation test at 400 ºC (**Figure 4.4 A**) required longer time (~27 hours) to reach steady state possibly due to lower diffusivity at lower permeation temperature.

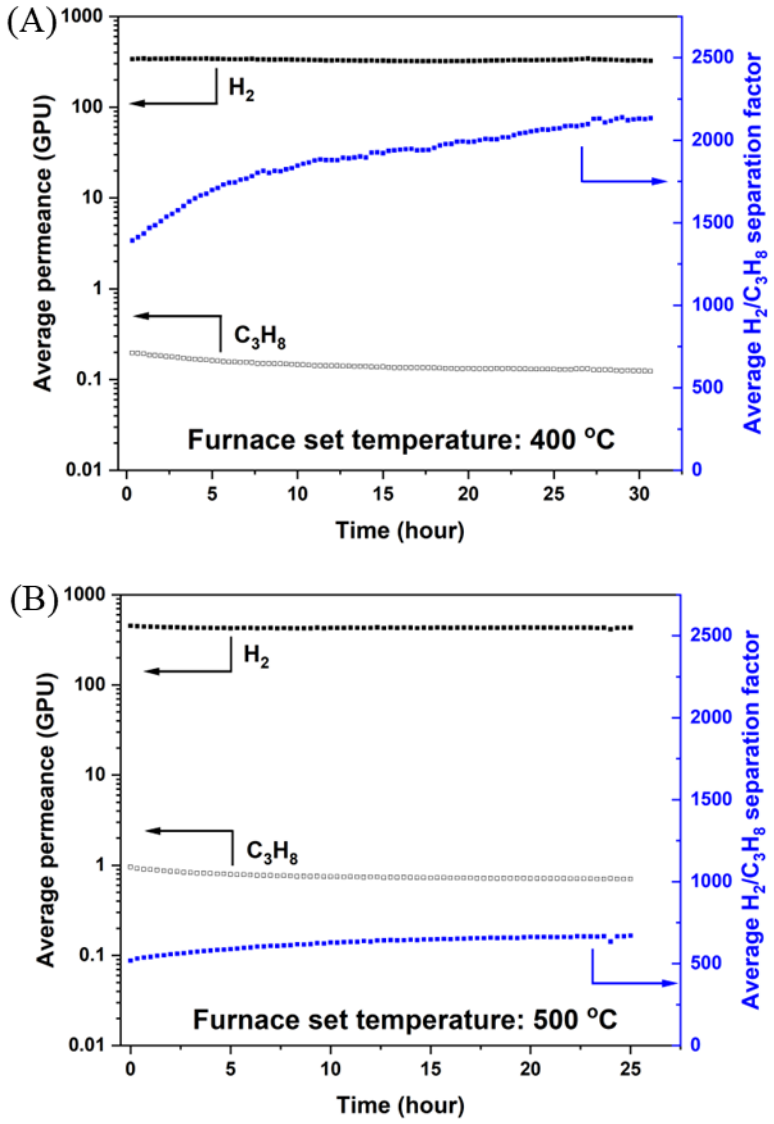

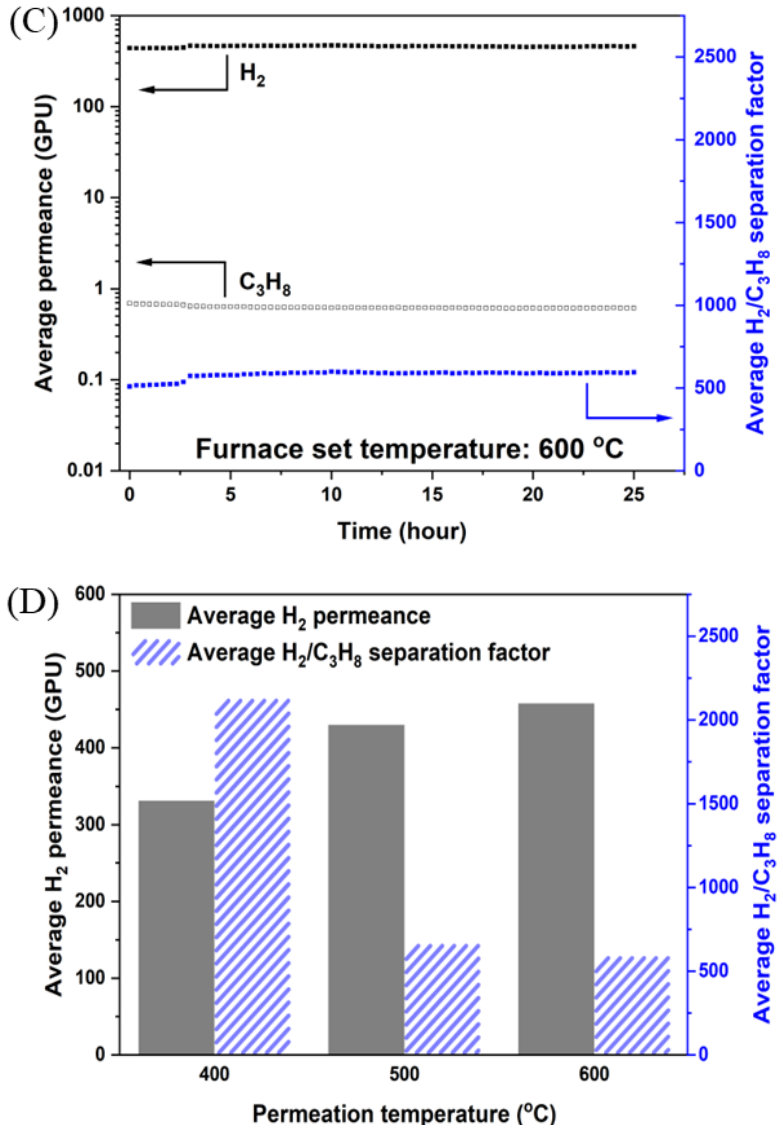

Figure 4.4 H_2/C_3H_8 separation performance in CMS hollow fiber membranes measured at different furnace set temperatures (A) 400 °C, (B) 500 °C, and (C) 600 °C; (D) Stabilized average permeances and separation factors. The measurements were carried out using the CMS hollow fiber membrane pyrolyzed at 675 °C with a 50%H_2/50%C_3H_8 feed mixture (1 bar).

Since heating provided by the single-zone furnace was not uniform, average permeances and separation factors were obtained from the permeation measurements. To predict permeances and separation factors at a given temperature, temperature distribution profiles (**Figure 4.5**) inside the furnace were obtained at each furnace set

temperature. The temperature at furnace center was equal to the furnace set temperature and reduced towards the edge of the furnace. The measured average permeances and temperature distribution profiles allowed us to calculate H_2 and C_3H_8 apparent permeation activation energies using the least squares method, which are 12.2 kJ/mol and 24.2 kJ/mol, respectively. The positive apparent permeation activation energies suggest high-temperature permeation of H_2 and C_3H_8 in the CMS membrane is dominated by diffusion. The apparent activation permeation energy of C_3H_8 is higher than that of C_2H_6 (19.0 kJ/mol), which was obtained from ambient-temperature (25-50 ^oC) C_2H_6 permeation data measured in Matrimid®-derived CMS dense films pyrolyzed at 675 ^oC.[163] Using the calculated apparent permeation activation energies and pre-exponential factors, H_2 and C_3H_8 permeances and H_2/C_3H_8 separation factors at 0-1000 ^oC (**Figure 4.6**) were calculated using the Arrhenius equation (Eqn 2.11).

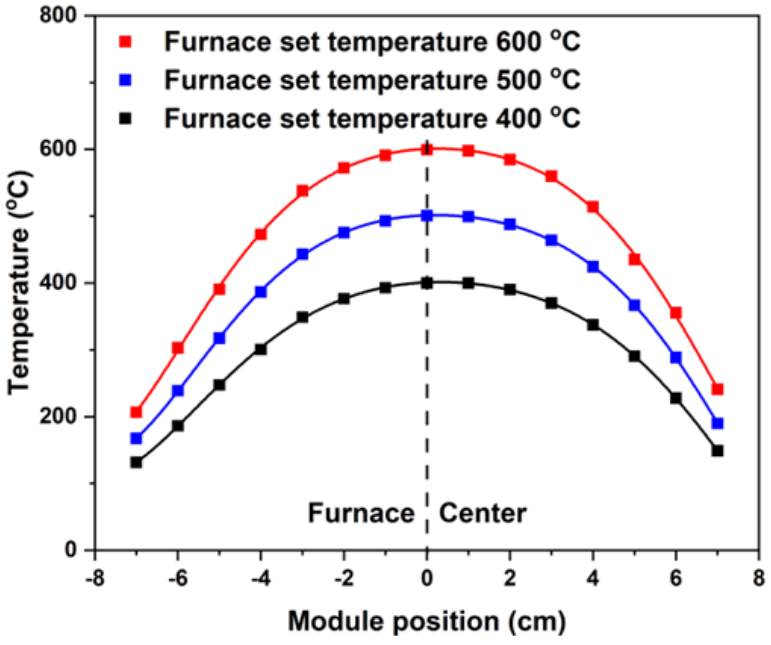

Figure 4.5. Furnace temperature distribution profiles (furnace length = 14 cm).

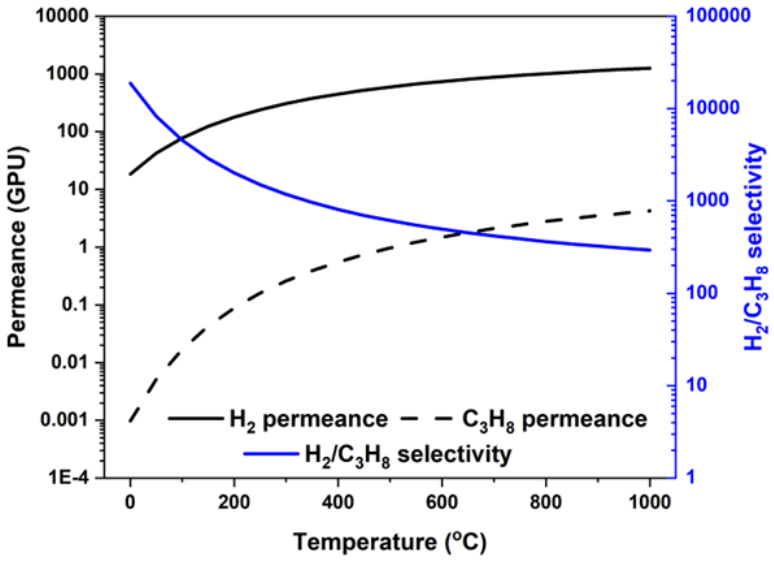

Figure 4.6. Calculated H_2 and C_3H_8 permeances and H_2/C_3H_8 selectivity at 0-1000 °C using the Arrhenius equation.

4.4 Effects of feed composition on CMS membrane performance

The effects of feed composition (H_2 and C_3H_8 molar ratio) on H_2/C_3H_8 separation performance of asymmetric CMS hollow fiber membranes were studied at furnace set temperature of 600 °C (**Figure 4.7**). The CMS hollow fiber membranes pyrolyzed at 675 °C were used for the permeation measurements. Five H_2/C_3H_8 feed mixtures were used: (A) 15%/85% H_2/C_3H_8; (B) 25%/75% H_2/C_3H_8; (C) 50%/50% H_2/C_3H_8; (D) 60%/40% H_2/C_3H_8; (E) 75%/25% H_2/C_3H_8.

With feed A (15%/85% H_2/C_3H_8), the CMS hollow fiber membrane showed reduced average H_2 and C_3H_8 permeances and increased average H_2/C_3H_8 separation factor over time and a stable H_2/C_3H_8 separation factor cannot be obtained following 25 hours (**Figure 4.7 A**). With feed E (75%/25% H_2/C_3H_8), the CMS hollow fiber membrane showed increased H_2 and C_3H_8 permeances and reduced H_2/C_3H_8 separation

factor over time (**Figure 4.7 E**). With feed B, C, and D, stable high-temperature H_2/C_3H_8 separation performance was obtained in the CMS hollow fiber membranes (**Figure 4.7 B-D**).

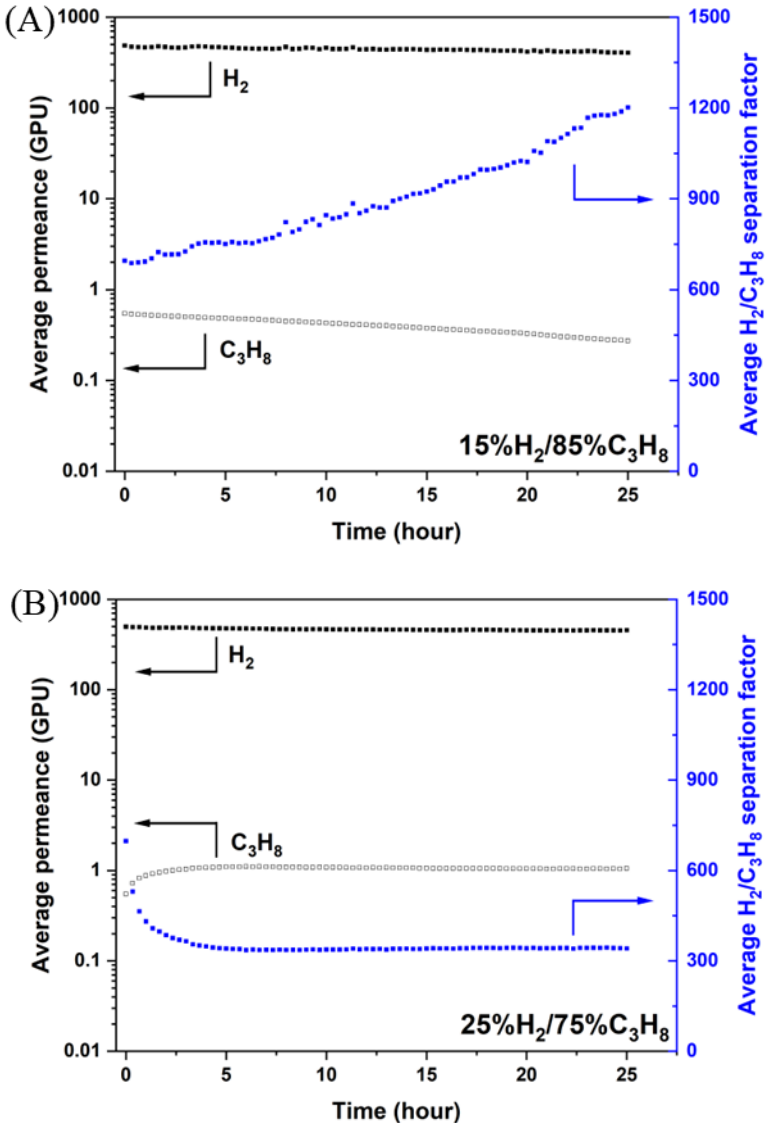

(C)

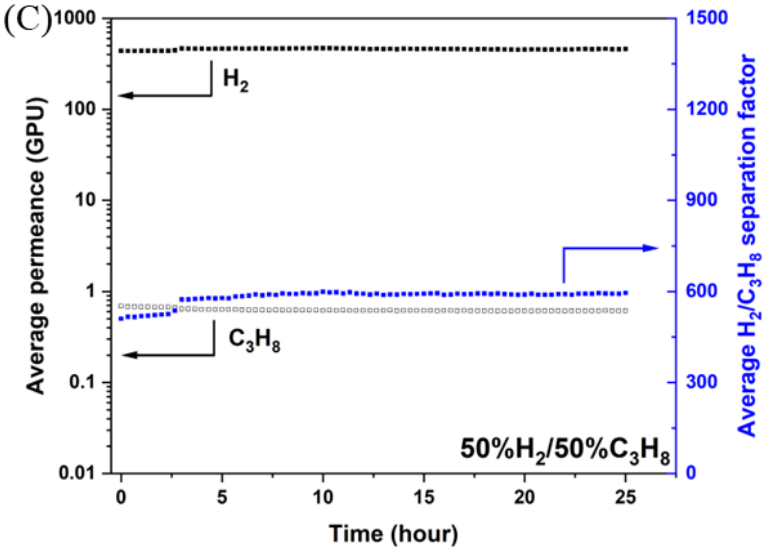
Average permeance (GPU)
Average H2/C3H8 separation factor
Time (hour)
H2
C3H8
50%H2/50%C3H8
1000
100
10
1
0.1
0.01
1500
1200
900
600
300
0
0
5
10
15
20
25

(D)

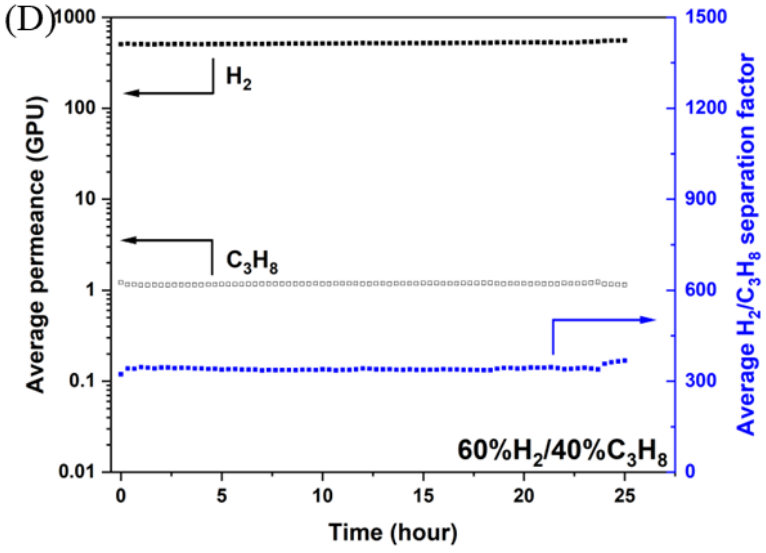
Average permeance (GPU)
Average H2/C3H8 separation factor
Time (hour)
H2
C3H8
60%H2/40%C3H8
1000
100
10
1
0.1
0.01
1500
1200
900
600
300
0
0
5
10
15
20
25

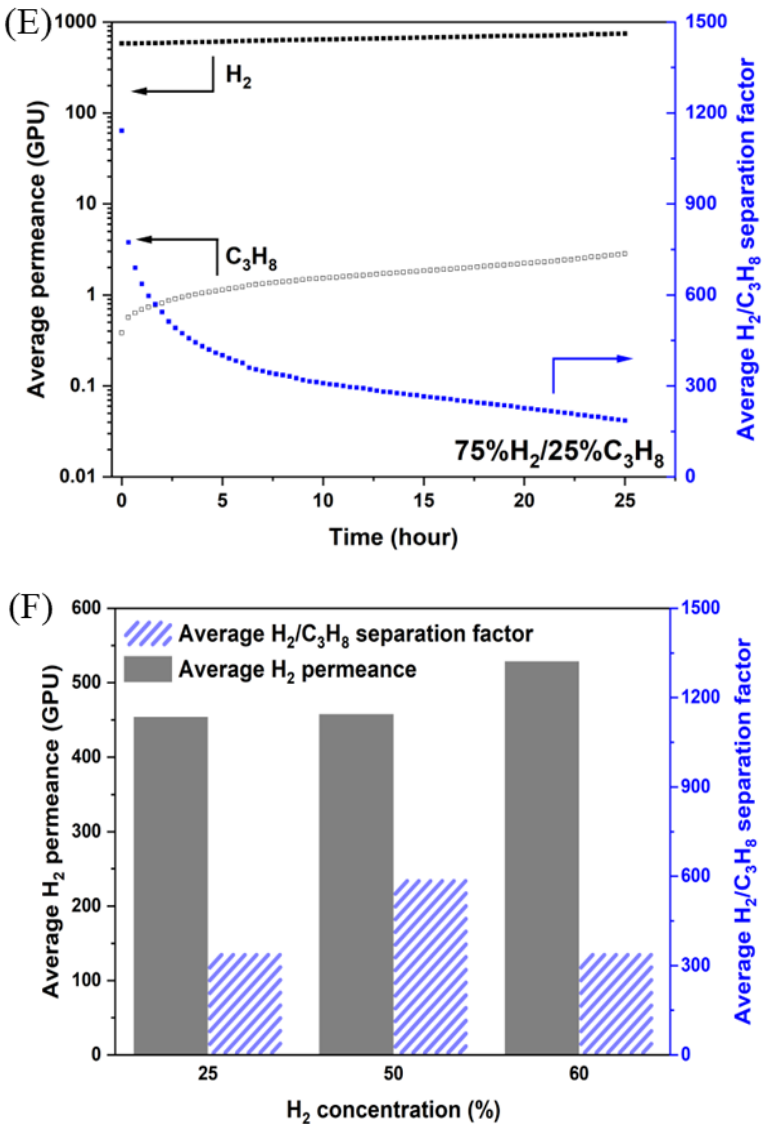

Figure 4.7. H_2/C_3H_8 separation performance in CMS hollow fiber membranes using feed mixture (1 bar) comprising (A) 15%/85% H_2/C_3H_8, (B) 25%/75% H_2/C_3H_8, (C) 50%/50% H_2/C_3H_8, (D) 60%/40% H_2/C_3H_8, and (E) 75%/25% H_2/C_3H_8; (F) Stabilized average permeances and separation factors under feed (B), (C), and (D). The measurements were performed at 600 ºC using the CMS hollow fiber membrane pyrolyzed at 675 ºC.

To understand the time-dependent permeation properties, we prepared CMS dense films using Matrimid® precursor dense films pyrolyzed at 675 ºC. The stability of the CMS dense films was first tested under inert atmosphere at high temperatures,

where the CMS dense films were heated at 600 °C in continuous Ar gas flow for 15 hours. The effluent gas was sent to the mass spectrometer for composition analysis. **Figure 4.8** showed the recorded MS data of the effluent gas at the sampling time of 0, 3, 9 and 15 h, respectively. It should be noted that 0 h means that the CMS film material has been pre-treated at room temperature for 3 h, right before the temperature ramping. The most significant m/z peak was from Ar (m/z=20). The Ar major signal (m/z=40) was excluded from the measurement because its intensity exceeded the equipment detection maximum limit. The other two groups of peaks were from the water (m/z=18) and hydrocarbon (m/z=36) impurities in the system. All these signals did not change with the testing time, indicating that CMS film sample was stable under high temperature inert atmosphere.

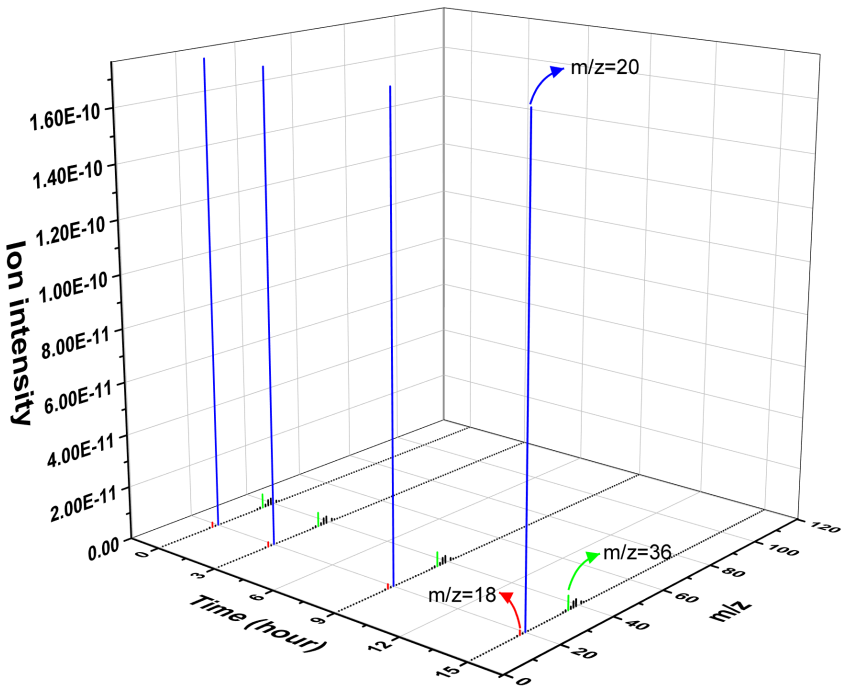

Figure 4.8. Mass spectra of effluent gas from thermal treatment of CMS dense films under high temperature inert atmosphere. (The temperature increased from room temperature to 600 °C and kept at 600 °C for 15 hours. Constant Ar flow of 60 mL/min was used during the analysis.)

We hypothesize gas-phase propane dehydrogenation reaction occurred in the CMS hollow fiber module feed side and produced C_3H_6 at high temperatures. C_3H_6 decomposition occurs with C-C bond scission, forming C_2H_5 and CH_3 radicals, which can react with each other and form olefins.[164] The produced olefins react with each other and form alkynes, i.e., acetylene and propyne. Acetylene can directly form pyrocarbon or convert to benzene through intermediate steps and finally form polycyclic aromatic hydrocarbons, such as naphthalene, anthrathene, and cyclopentapyrene. **Figure 4.9 A** shows the simplified reaction scheme for pyrocarbon deposition from C_3H_6.[164] The deposition of pyrocarbon on CMS membrane pore network (**Figure 4.9 B)** alters membrane pore structure, thereby changing membrane permeation properties over time. Indeed, chemical vapor deposition of C_3H_6 and other hydrocarbons was used as a post-treatment tool to refine the pore size of CMS membranes and adsorbents.[139, 165] The effect of C_3H_6 on CMS membrane pore structure was studied by exposing fresh CMS dense films to pure C_3H_6 at 600 ^oC for 12 hours. Following the C_3H_6 exposure, both DFT pore surface area and pore volume of the CMS dense film dramatically dropped (**Table 4.1**).

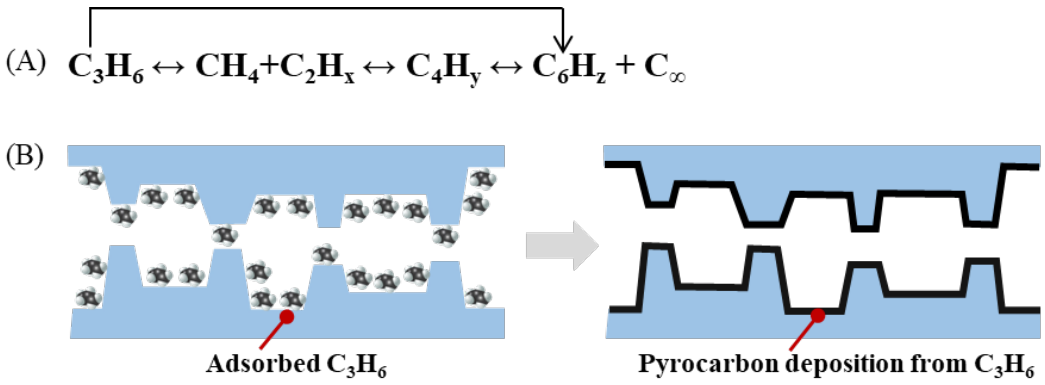

Figure 4.9. (A) Reaction scheme for pyrocarbon deposition from C_3H_6.[164] (B) Schematics showing hypothetical CMS pore structure changes as a result of C_3H_6-induced pyrocarbon deposition.

Table 4.1. DFT pore surface area and pore volume (pore width < 10.66 Å) of CMS films.

	Fresh CMS	C_3H_6-exposed CMS	H_2-exposed CMS
Pore surface area (m^2/g)	346.0	123.2	429.5
Pore volume (cm^3/g)	0.102	0.034	0.133

H_2 is known as a gasifying agent, which can remove carbonaceous deposits from coked catalysts via hydrogenation.[166] A recent report showed that mixing H_2 in pyrolysis purge gas can increase CMS pore sizes.[66] We hypothesize that adsorbed H_2 molecules cause hydrogenation and thinning of the graphene-sheets that constitute the CMS ultramicropores under high-temperature permeation (**Figure 4.10**), which increases CMS ultramicropore size. The enlarged CMS ultramicropores increase diffusivities and permeances while reducing the membrane diffusion selectivity and separation factor. The effect of H_2 on CMS membrane pore structure was investigated by exposing fresh CMS dense film to pure H_2 at 600 ^oC for 12 hours. Following H_2 exposure, the CMS dense film showed increased DFT pore surface area and pore volume (**Table 4.1**). Comparing the pore size distribution between fresh CMS dense film and H_2-exposed CMS dense film indicates that high-temperature H_2 exposure enlarged the CMS ultramicropores. Remarkably, the "fine" ultramicropores smaller than 5 Å disappeared following the high-temperature H_2 exposure (**Figure 4.11**). These results indicate that high-temperature H_2 exposure can be used as post-synthetic modification to tune the pore structure and separation performance of CMS membranes.

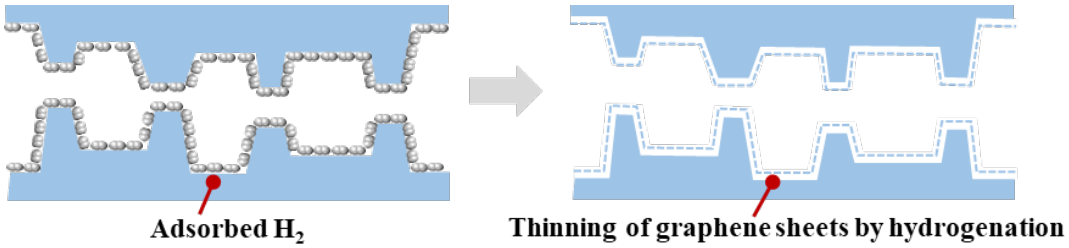

Figure 4.10. Schematics showing hypothetical CMS pore structure changes as a result of H_2-induced hydrogenation.

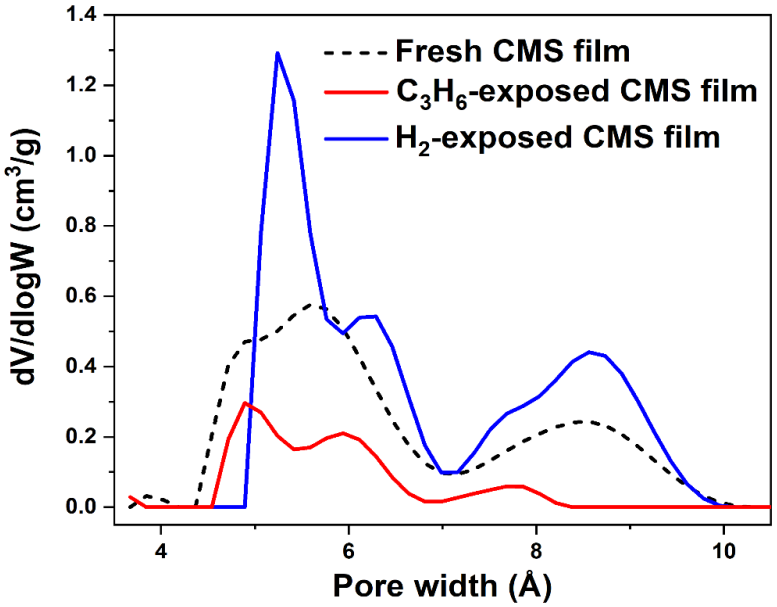

Figure 4.11. DFT pore size distribution of fresh CMS dense films and CMS dense films exposed to pure C_3H_6 and pure H_2, respectively.

The CMS membrane structural changes by C_3H_6-induced coke deposition and H_2-dehydrogenation are not known to take place under room-temperature permeation. They are possibly unique to high-temperature permeation, in which both the membrane and the penetrants are more reactive. Notably, the asymmetric CMS hollow fiber membrane can provide stable high-temperature H_2/C_3H_8 separation performance under a comfortably wide feed composition window of 25-60% H_2 (i.e., feed B, C, and D, **Figure 4.5 B-D**). It should be noted that hydrogenation by H_2 exposure will possibly

not be a concern for PDH membrane reactors because H_2 concentration in the membrane reactor will likely be low due to continuous H_2 removal. While pyrocarbon deposition by C_3H_6 exposure causes membrane separation factor to increase over time, the influence on CMS membrane reactor will likely be minor because H_2 permeance showed negligible drop over time (**Figure 4.7 A**).

4.5 Stability of CMS hollow fiber membrane under high-temperature permeation

A CMS hollow fiber membrane module (675 ºC pyrolysis) was constructed to study the membrane's long-term stability under high-temperature H_2/C_3H_8 permeation. The permeation test was performed at 600 ºC under 50%/50% H_2/C_3H_8 feed. Once steady state permeation was reached (~10 hours), the membrane showed outstanding stability (**Figure 4.12**) under continuous permeation for ~130 hours with average H_2 permeance of 430 GPU and average H_2/C_3H_8 separation factor of 511. Only a slight drop in average H_2 permeance (~4.7 %) and increase in average H_2/C_3H_8 separation factor (~3 %) were observed during the course of the permeation test, which may be attributed to physical aging of the CMS membrane. Indeed, Qiu and co-workers showed that physical aging can occur even as CMS membranes are exposed to high temperatures.[167] Compared with microporous oxide membranes (e.g., zeolite, [19, 168, 169] microporous silica [40, 170]), the CMS hollow fiber membranes can provide ~2-100 folds higher H_2/C_3H_8 separation factors (**Figure 4.13**) and competitive H_2 permeances under similar permeation conditions at 600 ºC.

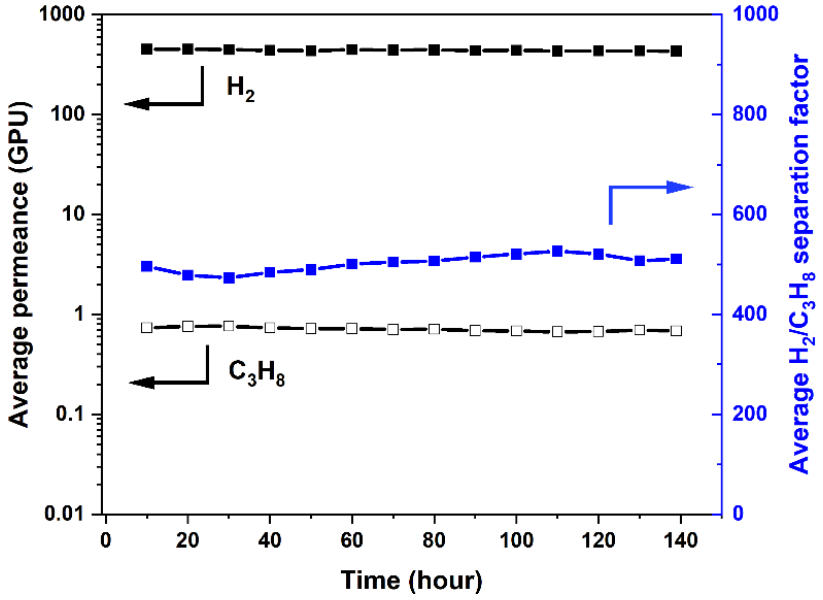

Figure 4.12. CMS hollow fiber membrane stability under a long-term (130 hours) high-temperature (600 °C) permeation test. The test was carried out using a CMS hollow fiber membrane pyrolyzed at 675 °C under a 50%H_2/50%C_3H_8 feed mixture (1 bar).

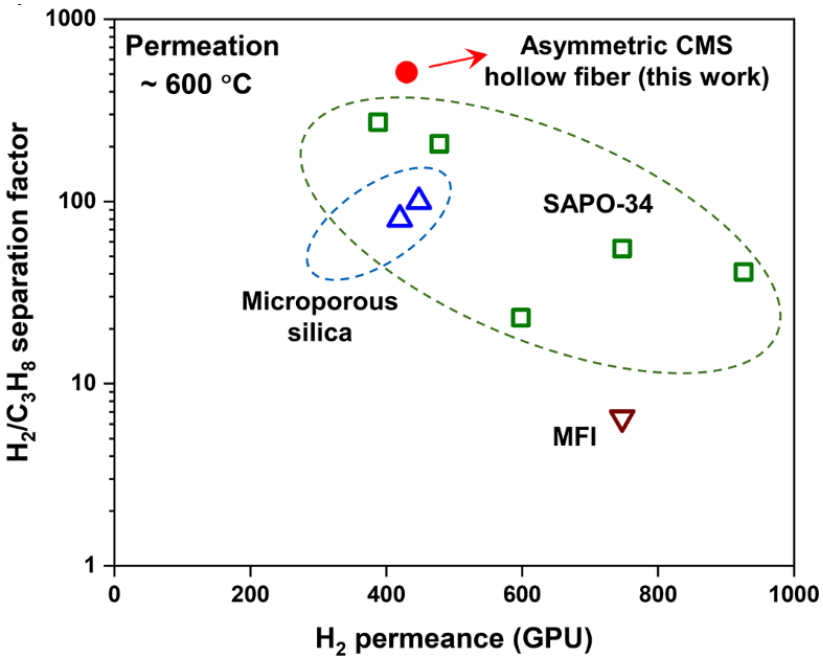

Figure 4.13. Comparing high-temperature (600 °C) H_2/C_3H_8 separation performance of the CMS hollow fiber membrane studied in this PhD work and microporous oxide membranes reported in literature.[19, 40, 168-170]

4.6 Ternary $H_2/C_3H_6/C_3H_8$ separation performance of CMS hollow fiber membranes

The high-temperature $H_2/C_3H_6/C_3H_8$ permeation test was carried out in the CMS hollow fiber membrane at 350-500 ^oC (**Figure 4.14**). The feed mixture ($5\%H_2/5\%C_3H_6/40\%C_3H_8$ balanced with Ar) comprised of both reactant C_3H_8 and products H_2/C_3H_6 to simulate PDH reaction conditions. As the permeation temperature increased, H_2 permeance almost stayed constant while C_3H_6 and C_3H_8 permeances dropped. This gave enhanced H_2/C_3H_6 and H_2/C_3H_8 separation factors at higher permeation temperatures. As discussed in Section 4.3, CMS membrane showed reduced pore size after high-temperature C_3H_6 exposure since the adsorbed C_3H_6 molecules induce pyrocarbon deposition in the CMS membrane pore network. Therefore, the enhanced separation factor observed here was due to the existence of C_3H_6 at high temperature, leading to the shrinkage of CMS pore structure and thus the rejection of large hydrocarbon molecules by the ultramicropores in CMS. Notably, the CMS hollow fiber membrane showed simultaneously attractive H_2 permeance (229 GPU) and high H_2/C_3H_8 separation factor (293) under 500 ^oC permeation. The attractive separation performance indicates the effectiveness of applying CMS hollow fiber membranes into membrane reactor to enhance conversion by removing H_2.

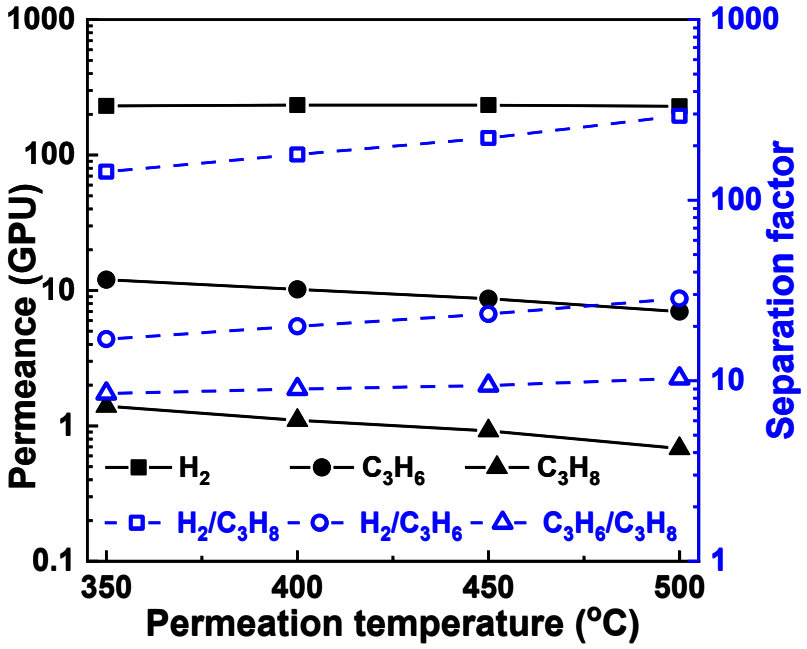

Figure 4.14. High-temperature (350-500 °C) separation performance of the CMS hollow fiber membrane. Testing conditions: Feed=20 mL/min 5%H_2/5%C_3H_6/4%C_3H_8 balanced with Ar, 1 bar; Sweep=20 mL/min Ar, 1 bar.

4.7 Summary and conclusions

For the first time, high-temperature permeation (up to 600 °C) in asymmetric CMS hollow fiber membranes with thin (~5 μm) separation layers was systematically investigated. As the CMS hollow fiber membrane pyrolysis temperature increased, the average H_2 permeance decreased with increasing average H_2/C_3H_8 separation factors. We also found that CMS hollow fiber membrane permeances increase with increasing permeation temperature, suggesting high-temperature H_2/C_3H_8 permeation in CMS membranes is diffusion-controlled. The Arrhenius equation was used to calculate H_2 and C_3H_8 apparent permeation activation energies, which allowed us to estimate membrane intrinsic H_2/C_3H_8 permeation properties at given temperatures. The feed composition was found to affect the stability of high-temperature H_2/C_3H_8 permeation

in CMS hollow fiber membranes, which was not seen for room-temperature permeation. A stable feed composition window of 25-60% H_2 was identified under the studied conditions, outside of which time-dependent permeation was observed presumably due to CMS membrane pore structure change as a result of hydrogenation or coking. Finally, under a continuous permeation test (~130 hours) using a 50%/50% H_2/C_3H_8 feed mixture at 600 ºC, the CMS hollow fiber membranes pyrolyzed at 675 °C showed average H_2 permeance of 430 GPU and H_2/C_3H_8 separation factor of 511 exceeding those of microporous oxide membranes under similar permeation conditions. Overall, the results suggest asymmetric CMS hollow fiber membranes can provide attractive high-temperature H_2/C_3H_8 separation performance and hence are promising for propane dehydrogenation membrane reactor applications.

Chapter 5: Evaluation of CMS hollow fiber membrane reactors for propane dehydrogenation

5.1 Overview

Non-oxidative propane dehydrogenation (PDH) can fill the supply-demand gap of propylene. However, commercial moving or fixed-bed PDH reactors are challenged by limited conversion due to thermodynamics and rapid catalyst deactivation. While membrane reactors can overcome the thermodynamic limit by in situ H_2 removal, their commercial practice has been limited by costly fabrication of inorganic or metallic membranes and quick catalyst deactivation due to H_2 depletion. The materials of PDH membrane reactor (i.e., membrane and catalyst) are hence crucial to overcome these challenges.

In this chapter, carbon molecular sieve (CMS) membrane reactor, which integrates scalable H_2-permeable asymmetric CMS hollow fine fiber membranes with siliceous zeolite supported metal catalysts, was first time developed for PDH reaction. With rapid H_2 removal by CMS membranes and low-temperature propane activation, the novel CMS membrane reactor achieved an unprecedented synergy of four-fold propane conversion enhancements, high propylene selectivity, and record-high stability at low reaction temperature.

Section 5.2 describes the silicalite-1 supported platinum-zinc catalyst performance under PDH reaction conditions. Section 5.3 discusses the role of CMS hollow fibers on membrane reactor performance. A comparison was performed

between CMS membrane reactors and literature reported membrane reactors in terms of conversion enhancement and operation temperature for PDH reaction. Section 5.4 studies the impact of operating conditions on PDH membrane reactor performance including reaction temperature, feed space velocity, propane feed partial pressure, and sweep gas flow rate. Section 5.5 investigates long-term stability of propane conversion and propylene selectivity of the CMS membrane reactor. The deactivation rate of CMS membrane reactor was calculated and compared with previously reported membrane reactors for PDH. The regeneration on spent catalyst was performed and the activity of regenerated catalyst was compared to fresh catalyst performance. Section 5.6 summarizes the main findings of the work on PDH membrane reactors using asymmetric CMS hollow fine fiber membranes and siliceous zeolite confined metal catalysts.

5.2 Pt-Zn/S1 catalyst performance

The catalytic performance of platinum-zinc/silicalite-1 (Pt-Zn/S1) catalyst was studied prior to assembly of the CMS hollow fiber membrane reactor. The Pt-Zn/S1 catalysts (**Figure 5.1**) have the particle size in the range of 3-6 μm, where the bimetal Pt-Zn clusters have an average size of ~1.17 nm.[171] The absence of Lewis and Brønsted acidic centers in the siliceous zeolite eliminates acid-catalyzed side reactions such as cracking and oligomerization that lead to low propylene selectivity and catalyst deactivation due to coke deposition. The small metal clusters are effective for propane activation and suppression of side-reactions involving hydrogenolysis (C-C cleavage) and/or coke formation (C-C coupling) occurred on geometrically complex and large

ensembles of metal atoms.[12, 161, 172] The confinement of zeolite micropores prevents metal site sintering and the consequent deactivation.[173, 174]

The catalysts were first tested in a packed-bed reactor (PBR) from 275 ºC to 500 ºC (**Figure 5.2**). With increasing of reaction temperature, C_3H_8 conversion increased with slightly dropped C_3H_6 selectivity (still above 80% at 500 ºC). Remarkably, the catalyst showed low threshold activation temperature, where the PDH over Pt-Zn/S1 catalyst attained equilibrium conversion at reaction temperature as low as 275 ºC. The Pt-Zn/S1 catalyst exhibited high activity and attractive selectivity, which is suitable for PDH reaction.

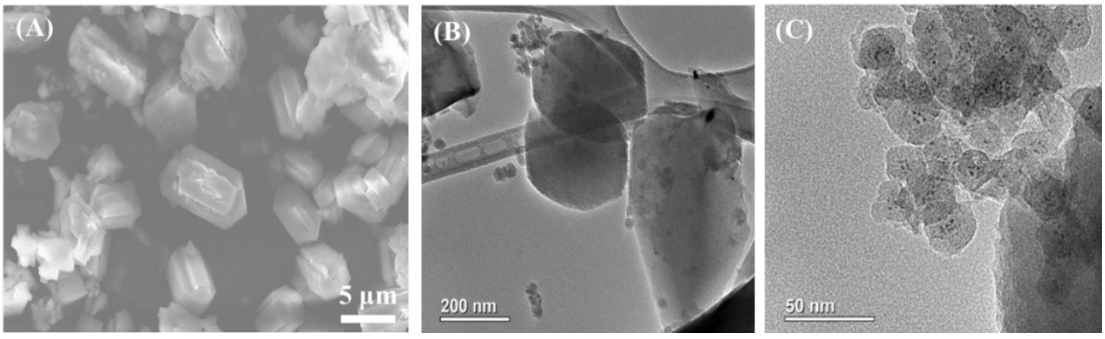

Figure 5.1. (A) SEM image of the Pt-Zn/S1 catalyst. (B-C) TEM images of the Pt-Zn/S1 catalyst under different magnifications.[171]

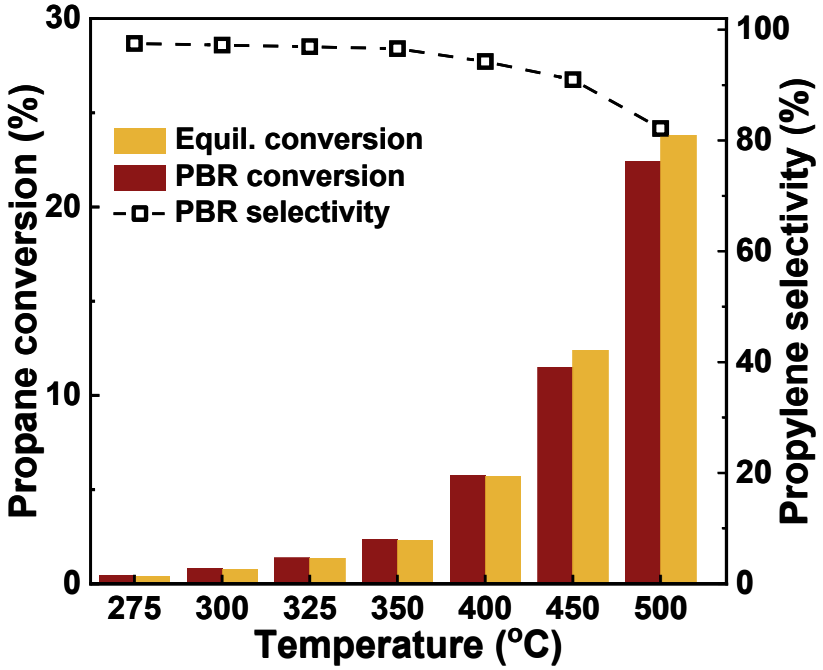

Figure 5.2. Conversion and selectivity of a packed bed reactor (PBR) consisting of the Pt-Zn/S1 catalyst with respect to reaction temperature. Equilibrium conversion at each temperature is shown for reference. Testing conditions: Feed=2.5 mL/min C_3H_8 + 2.5 mL/min Ar (WHSV=1.73 h^{-1}); Catalyst mass=0.3 g.

5.3 Effects of CMS membrane on PDH membrane reactor performance

The CMS hollow fiber membrane reactor was assembled by packing Pt-Zn/S1 catalyst particles on the shell side (outside) of CMS hollow fiber membranes (**Figure 5.3**). The PDH reaction was carried out by flowing a C_3H_8/Ar mixture at the hollow fiber shell side. An inert sweep gas (Ar) was introduced at the hollow fiber bore side (inside) to create a transmembrane H_2 partial pressure difference. The H_2 partial pressure difference provides H_2 permeation driving force through the CMS membrane, which allows H_2 in the reaction mixture to be continuously and selectively removed from the reaction mixture.

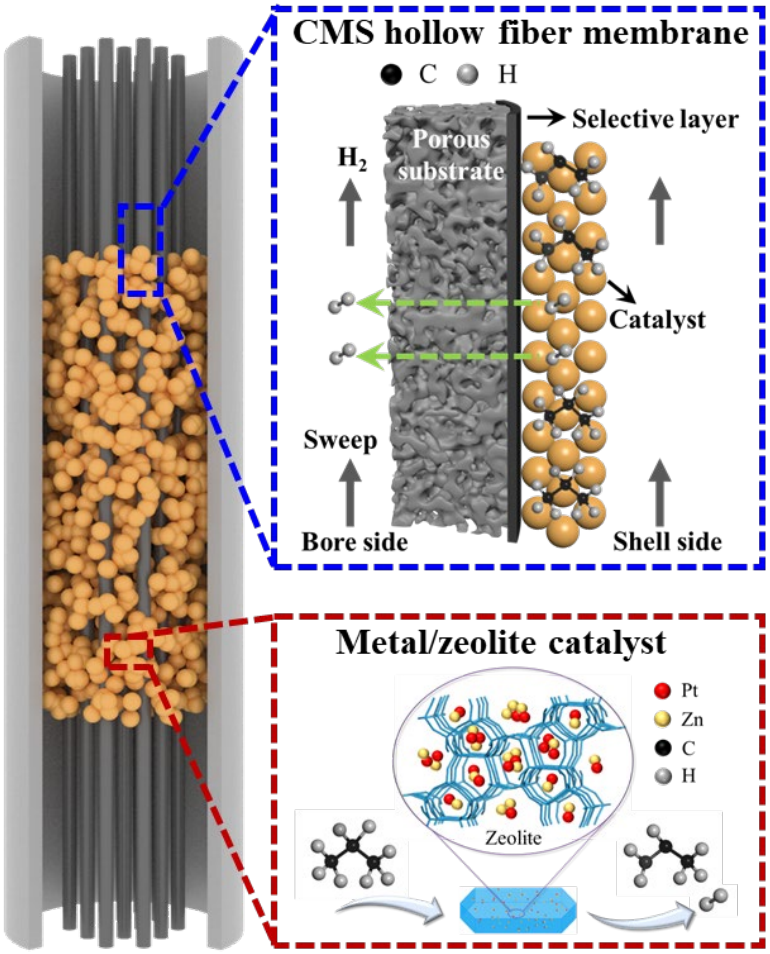

Figure 5.3. Schematic illustrating the CMS hollow fiber membrane reactor for propane dehydrogenation.

The benefit of CMS hollow fiber membranes for reactor conversion enhancement was clearly demonstrated in **Figure 5.4**. As the number of CMS hollow fibers increased from 0 (i.e., PBR) to 19, the C_3H_8 conversion significantly increased from 12.4% to 46.8%, almost quadrupling the thermodynamic equilibrium conversion. This was because a larger number of CMS hollow fibers increase the membrane permeation area and hence the H_2 permeation flow rate. The higher H_2 permeation flow rate reduces H_2 partial pressure in the reaction side, which drives the reversible PDH reaction forward and enhanced conversion according to the Le Chatelier's principle.

Notably, all CMS membrane reactors showed higher C_3H_6 selectivity (94-97%) than the packed-bed reactor (89%). Lower H_2 partial pressure in the reaction side suppresses side reactions such as hydrogenolysis and therefore increases the C_3H_6 selectivity in membrane reactor.

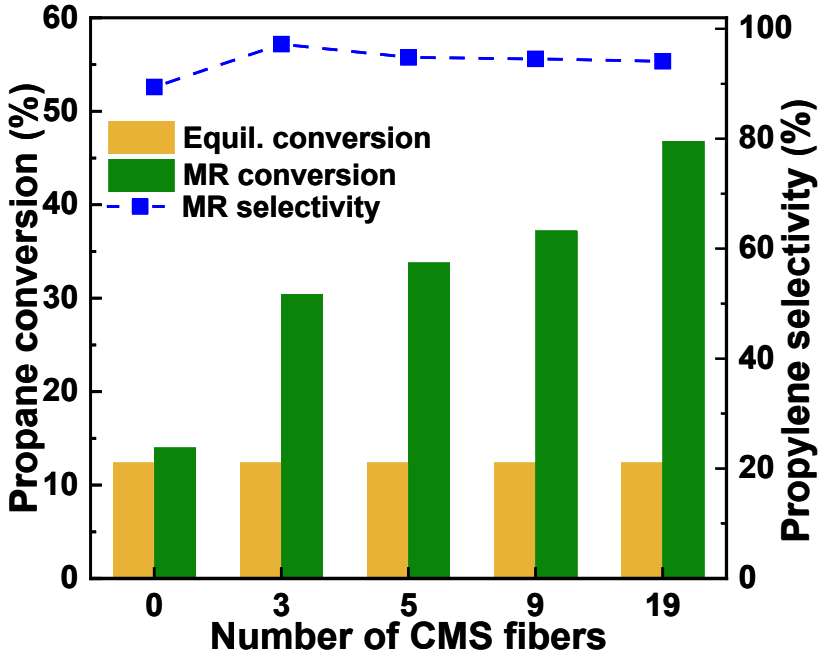

Figure 5.4. The effect of the number of CMS hollow fiber membrane on enhancing membrane reactor (MR) conversion. Testing conditions: Feed=0.5 mL/min C_3H_8 + 0.5 mL/min Ar (WHSV=0.35 h^{-1}); Sweep=100 mL/min Ar; Reaction temperature=450 ºC; Catalyst mass=0.3 g.

The conversion enhancement of the CMS membrane reactor was compared with a number of PDH membrane reactors reported in literature, which were made with different types of membranes (e.g., palladium, zeolite, silica, alumina) (**Figure 5.5**) and catalysts (**Figure 5.6**) (e.g., Pt cluster, Pt-Sn/silica, Pt-Sn/Al_2O_3, Cr_2O_3/Al_2O_3). The CMS membrane reactor reported in this work shows one of the highest conversion enhancements, almost four times as high as equilibrium conversion. Besides, the CMS membrane reactor was operated at a relatively low temperature (450 ºC) while the

reaction temperature of most reported PDH membrane reactors is in the range of 500-600 °C. Only a Pd-based membrane reactor showed conversion enhancement higher than the CMS membrane reactor.[60] It should be noted that the Pd-based membrane reactor had rapid conversion drop with time and will likely have limited use in practical applications.

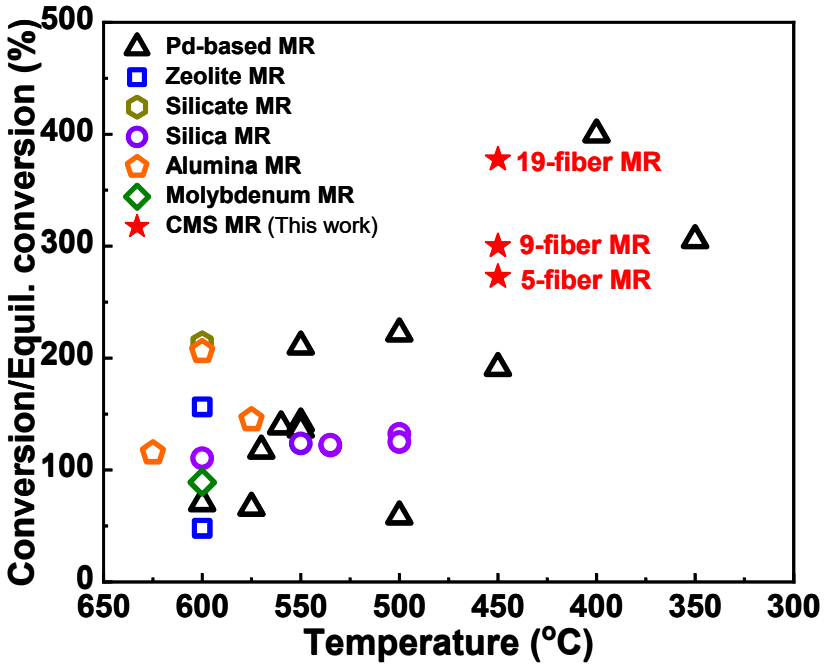

Figure 5.5. Comparing the conversion enhancement of CMS membrane reactor with membrane reactors reported in literature made by different membranes.

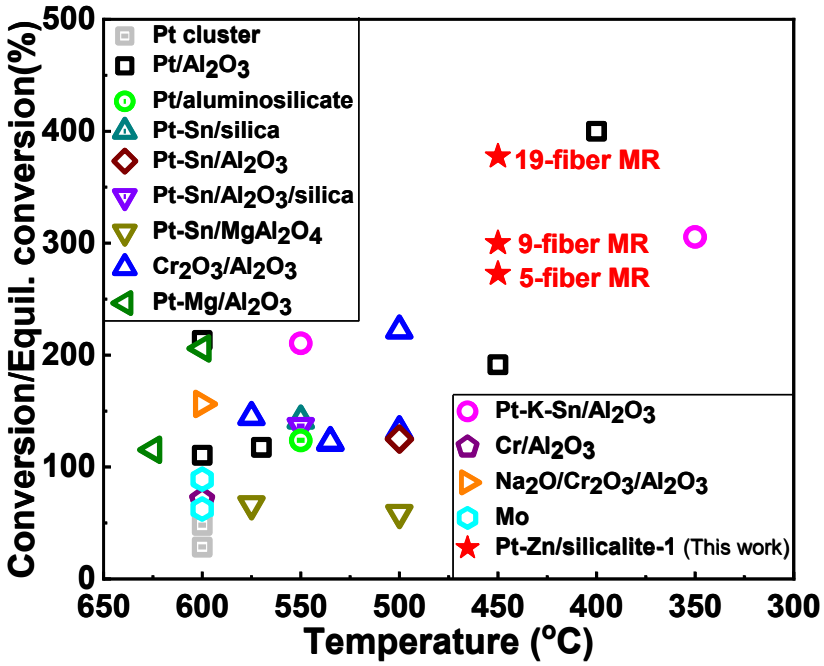

Figure 5.6. Comparing the conversion enhancement of CMS membrane reactor with membrane reactors reported in literature made by different catalysts.

5.4 Effects of operation conditions on PDH membrane reactor performance

5.4.1 Reaction temperature

The roles of reaction conditions (reaction temperature, weight hourly space velocity (WHSV), reactant partial pressure, and sweep gas flow rate) on C_3H_8 conversion and C_3H_6 selectivity of the CMS membrane reactor were systematically studied. As the reaction temperature increased from 350 to 500 °C, the C_3H_8 conversion increased from 3.2 to 36.0% (**Figure 5.7**), which can be explained by the endothermic nature of the PDH reaction. Increasing the reaction temperature also caused the C_3H_6 selectivity to drop from almost 100.0% to 92.8%, likely because side reactions such as cracking and cyclization occurred at higher reaction temperatures.

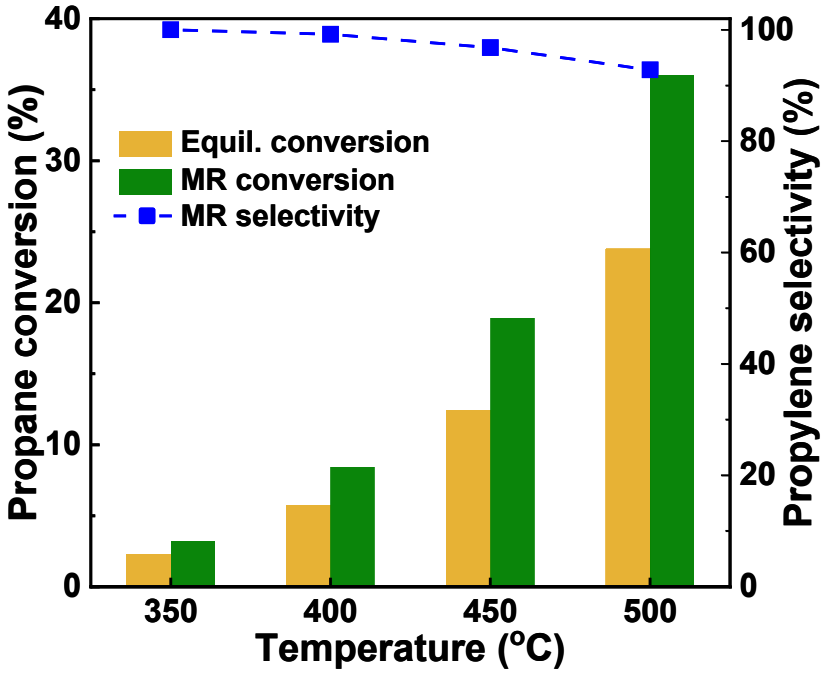

Figure 5.7. The effects of reaction temperature on propane conversion and propylene selectivity of the CMS membrane reactor. Testing conditions: Feed=2.5 mL/min C_3H_8 + 2.5 mL/min Ar (WHSV=1.73 h^{-1}); Sweep=100 mL/min Ar; Catalyst mass=0.3 g; Number of CMS fibers=5. Thermodynamic equilibrium conversions are shown for reference.

5.4.2 Feed space velocity

The feed space velocity was varied by keeping the feed composition constant (50%C_3H_8/50%Ar) while changing the total feed flow rate. As the WHSV of the feed decreased from 3.46 to 0.35 h^{-1}, C_3H_8 conversion increased from 14.9% to 33.8% and C_3H_6 selectivity decreased from 98.6% to 94.8% in the 5-fiber CMS membrane reactor at 450 °C (**Figure 5.8**). At lower WHSV, the gas residence time is longer in the reaction zone, allowing more H_2 permeation through the membrane and thus shifting the equilibrium toward the product side. By increasing the reaction temperature and the number of incorporated CMS fibers, a 19-fiber CMS membrane reactor can achieve commercially attractive C_3H_8 conversion (36.5%) with high C_3H_6 selectivity (97.9%) under high WHSV (3.46 h^{-1}) at 500 °C.

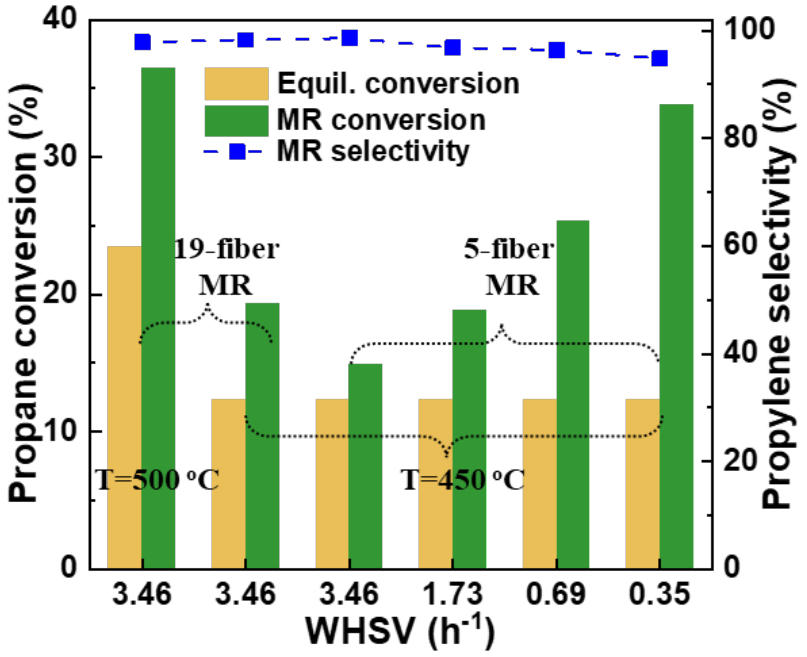

Figure 5.8. The effects of feed space velocity on propane conversion and propylene selectivity of the CMS membrane reactor. Testing conditions: Feed=50%C_3H_8/50%Ar; Sweep=100 mL/min Ar; Reaction temperature=450 °C; Catalyst mass=0.3 g; Number of CMS fibers=5. Thermodynamic equilibrium conversions are shown for reference.

5.4.3 Propane feed partial pressure

The C_3H_8 feed partial pressure was controlled by varying the C_3H_8 feed flow rate in a constant total feed flow. As the C_3H_8 feed partial pressure decreased from 80 to 10 kPa, C_3H_8 conversion increased from 14.9% to 35.7% with almost constant C_3H_6 selectivity ~ 97% (**Figure 5.9**). This is because PDH is a volume expansion reaction, and reducing reactant partial pressure drives the reaction forward according to the Le Chatelier's principle.

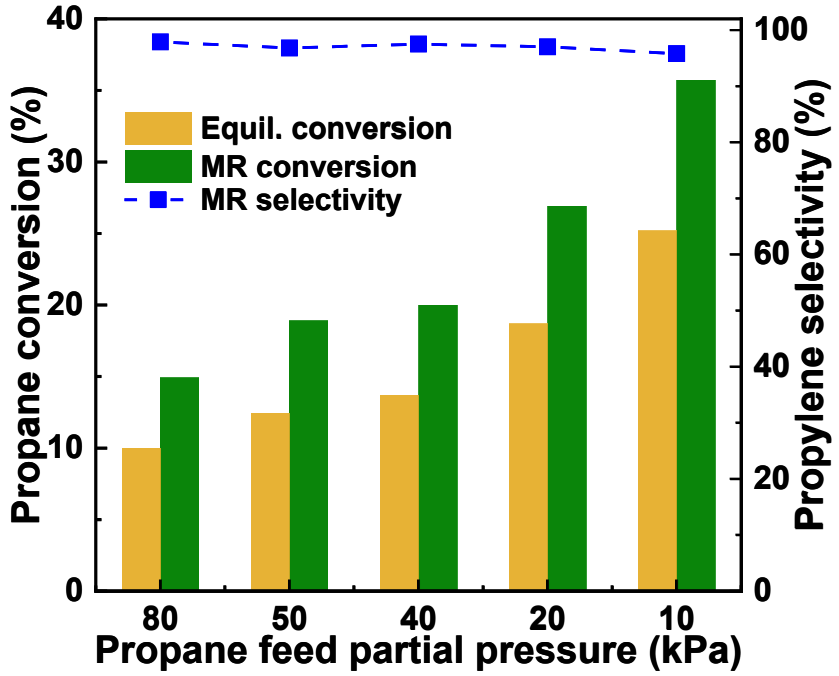

Figure 5.9. The effects of propane feed partial pressure on propane conversion and propylene selectivity of the CMS membrane reactor. Testing conditions: Feed=5 mL/min C_3H_8/Ar; Sweep=100 mL/min Ar; Reaction temperature=450 °C; Catalyst mass=0.3 g; Number of CMS fibers=5. Thermodynamic equilibrium conversions are shown for reference.

5.4.4 Sweep gas flow rate

As the sweep gas flow rate increased from 10 to 200 mL/min, C_3H_8 conversion slightly increased from 17.7% to 19.6% with almost constant C_3H_6 selectivity ~96% (**Figure 5.10**). Increasing the sweep gas flow rate reduces H_2 partial pressure in the permeate side, thereby enhancing the H_2 permeation driving force and allowing higher H_2 permeation flux, which in turn reduces H_2 partial pressure in the reaction side and leads to higher C_3H_8 conversion. It should be noted that the conversion almost levels off at large sweep flow rates since the sweep side H_2 partial pressure is almost to zero and the impact on H_2 permeation driving force is negligible.

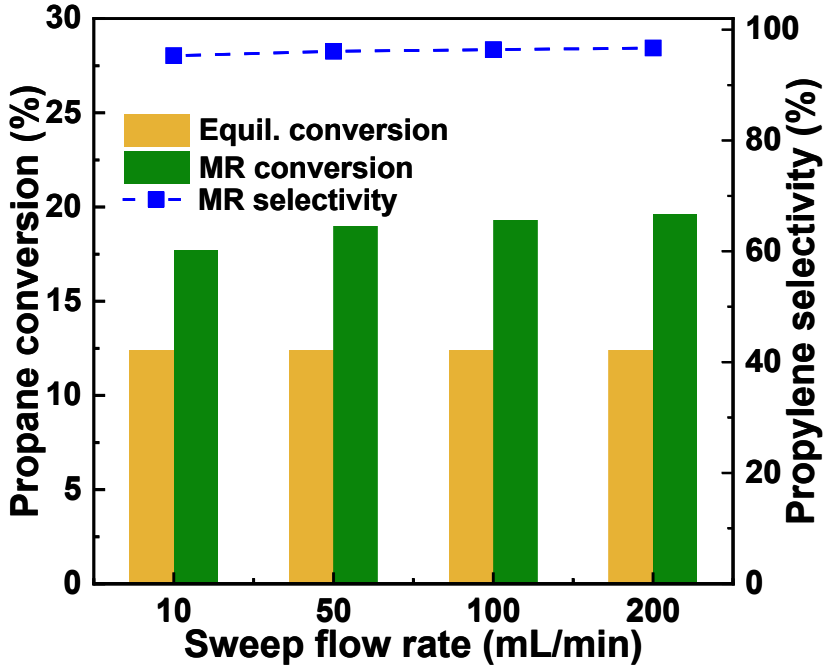

Figure 5.10. The effects of sweep flow rate on propane conversion and propylene selectivity of the CMS membrane reactor. Testing conditions: Feed=2.5 mL/min C_3H_8 + 2.5 mL/min Ar (WHSV=1.73 h^{-1}); Reaction temperature=450 ºC; Catalyst mass=0.3 g; Number of CMS fibers=5. Thermodynamic equilibrium conversions are shown for reference.

5.5 Stability of PDH membrane reactor

To further demonstrate the attractiveness of the CMS membrane reactor, we investigated the long-term stability (**Figure 5.11**) of propane conversion and propylene selectivity of the CMS membrane reactor. At 450 ºC, after time-on-stream of ~5 h (i.e., catalyst induction period), the membrane reactor achieved 34.1% C_3H_8 conversion, 2.4 times as high as the packed-bed reactor (14.0%). The membrane reactor also showed higher C_3H_6 selectivity (~97.1%) than the packed-bed reactor (~89.4%). The enhanced conversion and selectivity allowed the CMS membrane reactor to improve C_3H_6 yield (i.e., 2.7 times as high as the packed-bed reactor).

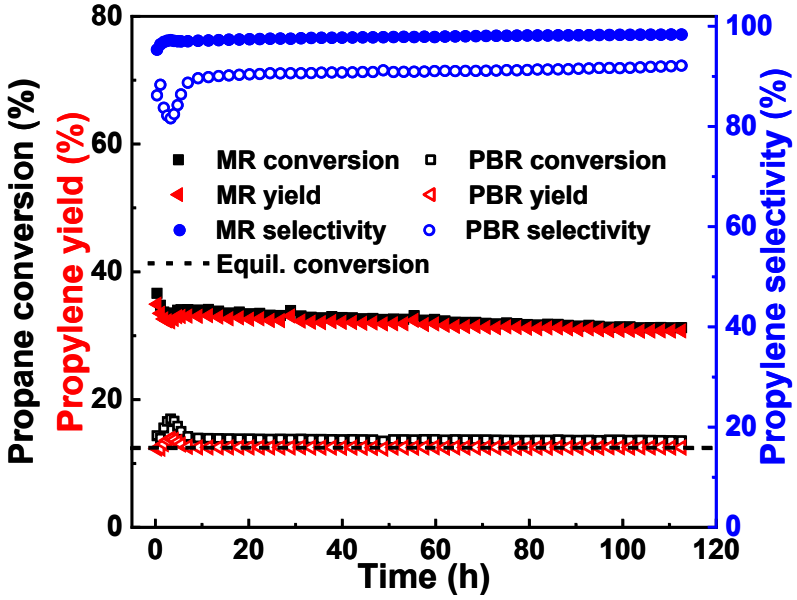

Figure 5.11. Conversion, yield, and selectivity in the CMS membrane reactor and packed-bed reactor (PBR) in long-term stability tests. Thermodynamic equilibrium conversion is shown for reference. PBR conditions: Feed=0.5 mL/min C_3H_8 + 0.5 mL/min Ar (WHSV=0.35 h^{-1}); Reaction temperature=450 °C; Catalyst mass=0.3 g. Membrane reactor conditions: same as PBR with sweep =100 mL/min Ar and number of CMS hollow fiber=5.

Remarkably, the CMS membrane reactor had excellent stability for at least 112 h with a slight drop of C_3H_8 conversion (34.1% to 31.3%) and slightly increased C_3H_6 selectivity (97.1% to 98.3%). The increase in C_3H_6 selectivity was possibly due to the suppression of cracking reactions by absence of catalyst acidity and lowering of H_2 pressure in the shell side.[175] This phenomenon was also reported by groups using zeolite based PDH membrane reactor, where C_3H_6 selectivity in membrane reactor was higher than that in PBR.[19, 20, 30] The slight decrease in C_3H_8 conversions could be due to catalyst coking. According to the thermogravimetric analysis results (**Figure 5.12)**, the weight loss difference (1.9%) between the pre-reduced Pt-Zn/S1 catalyst and spent catalyst in the membrane reactor was the deposited coke on the catalyst after 112 hours reaction. Notably, the catalyst weight loss in the membrane reactor is larger than

that in PBR, indicating higher catalyst coking rate due to the depletion of H_2 in the membrane reactor. Indeed, the C_3H_8 conversion in PBR performance was stable for 112 hours (**Figure 5.11**) with slightly higher conversion than equilibrium conversion due to side reactions, showing the excellent activity and stability of Pt-Zn/S1 catalyst. The analysis on the spent membrane reactor did not show obvious particle sintering in catalyst[171] (**Figure 5.13**) or morphology change in the CMS hollow fiber membrane (**Figure 5.14**). In comparison to literature reported PDH membrane reactors, CMS membrane reactors had the lowest deactivation rate ~ 2.1×10^{-3} h^{-1} (**Figure 5.15**). The reaction performance of PDH membrane reactors found in literature was summarized in **Appendix A**.

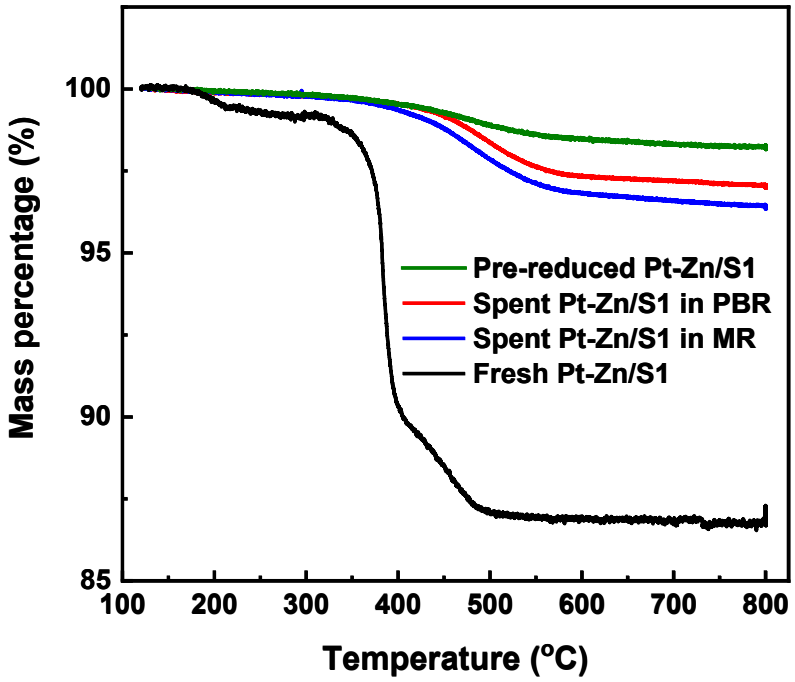

Figure 5.12. Thermo-gravimetric analysis (TGA) profiles on various Pt-Zn/S1 catalyst samples. (50 mL/min air used in TGA. The weight loss in the fresh catalyst was due to organic template decomposition under high temperature.)

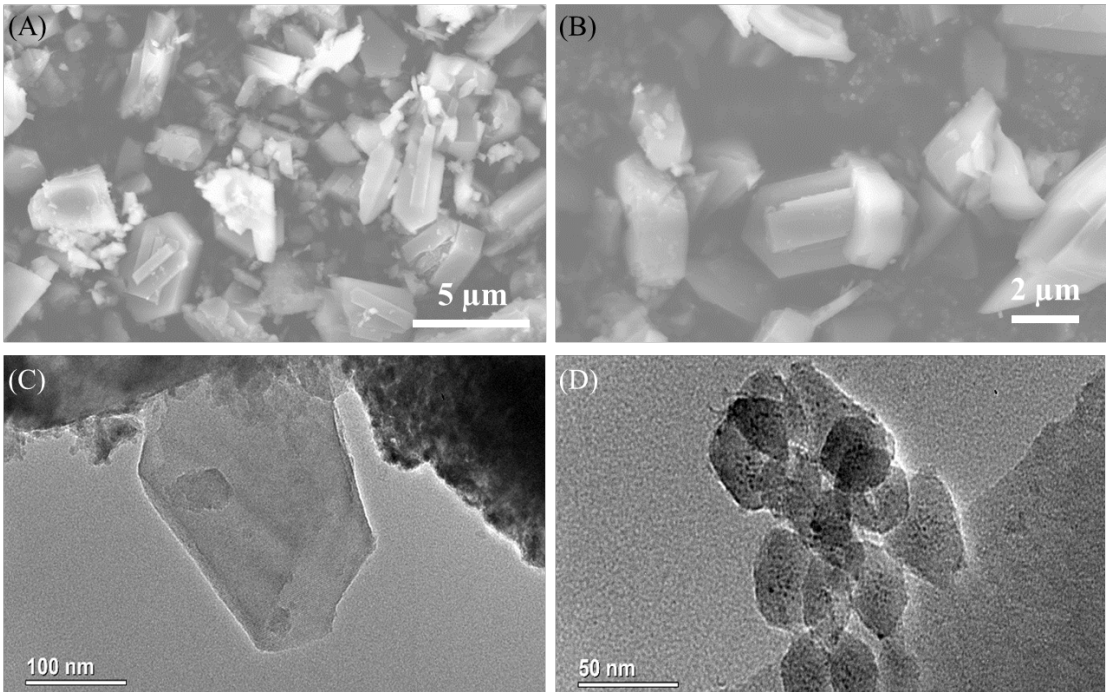

Figure 5.13. Morphology of spent Pt-Zn/S1 catalyst in the membrane reactor after 112 hours PDH reaction. (A)-(B) SEM images and (C)-(D) TEM images.[171]

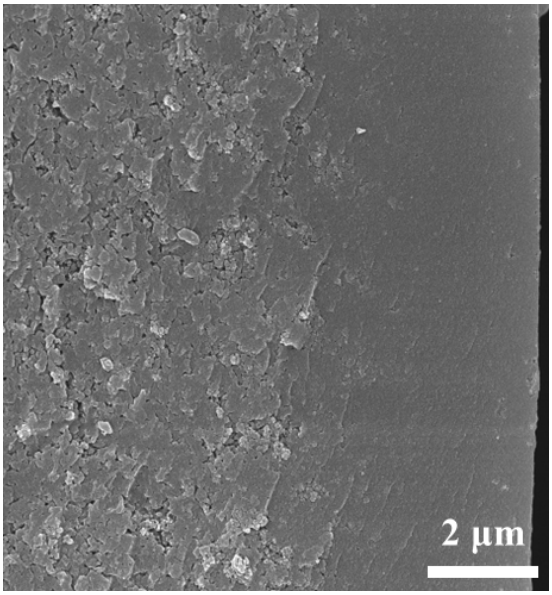

Figure 5.14. SEM image of spent CMS hollow fiber in the membrane reactor after 112 hours PDH reaction.

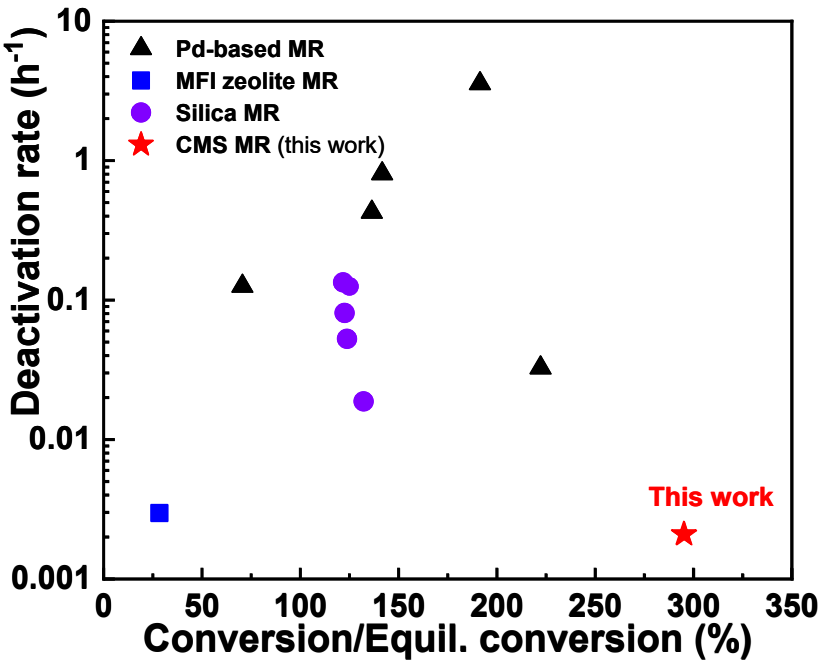

Figure 5.15. Comparing the deactivation rate of the CMS membrane reactor with PDH membrane reactors reported in literature.

The spent Pt-Zn/S1 catalysts in the membrane reactor after the long-term (i.e., 112 h) test of PDH were regenerated under H_2 gas flow at 500°C for 1 hour.[171] The propane reaction rates over spent and regenerated catalysts were measured and compared to fresh Pt-Zn/S1 catalyst performance (**Figure. 5.16**). While the spent catalyst showed a decreased propane reaction rate due to catalyst deactivation caused by coke deposition, the regenerated catalyst showed comparable propane reaction rate as compared to fresh Pt-Zn/S1 catalyst. The results suggested that the activity of the Pt-Zn/S1 catalyst can be recovered by the removal of carbon deposits under a H_2 gas stream. Alternatively, a dual-zone fluidized bed membrane reactor design can be used to counteract the catalyst deactivation/regeneration in continuous PDH operation.[176]

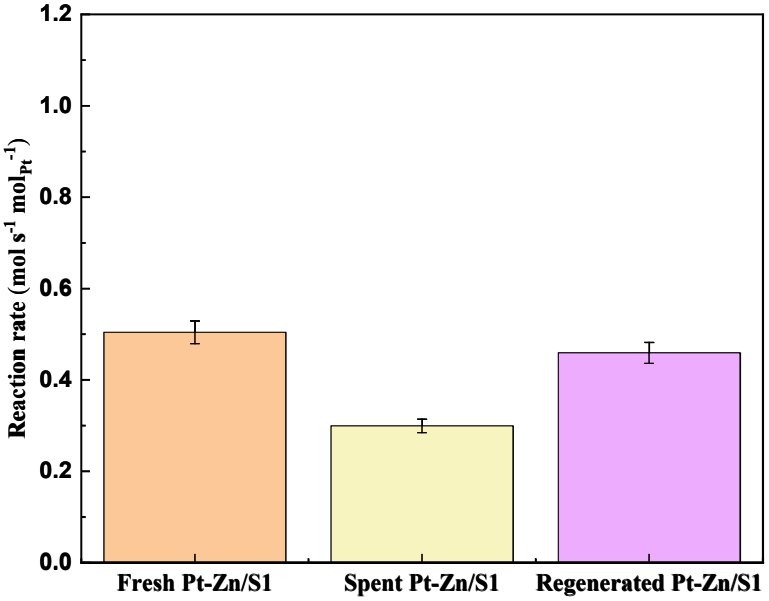

Figure 5.16. Reaction rates of fresh, spent (after 112 hours test in MR) and regenerated Pt-Zn/S1 catalysts. (Reaction condition: temperature: 450 ºC, WSHV= 51.53 h^{-1}, 50% C_3H_8/50% Ar).[171]

5.6 Summary and conclusions

In this chapter, we demonstrated a scalable carbon molecular sieve membrane reactor for non-oxidative propane dehydrogenation by integrating active and stable zeolite confined metal catalysts for low-temperature propane activation with H_2-permselective asymmetric CMS hollow fine fiber membranes for fast H_2 removal. The impacts of membrane separation area and operation conditions (i.e., reaction temperature, feed space velocity, propane feed partial pressure, and sweep gas flow rate) on the CMS membrane reactor performance were systematically investigated. The synergy between the Pt-Zn/S1 catalyst and CMS membrane significantly improved C_3H_8 conversion (e.g., almost 4 times as high as equilibrium conversion) with high C_3H_6 selectivity. Notably, the attractive performance was obtained at reaction temperature at least 150 °C below commercial PDH reactors, which suppressed coking

and therefore allowed the CMS membrane reactor to show outstanding stability far exceeding any known membrane reactors reported in PDH literature. The present work paves the road for sustainable on-purpose propylene production, and more broadly equilibrium-limited chemical manufacturing process.

Chapter 6: Modeling of carbon molecular sieve hollow fiber membrane reactor for propane dehydrogenation

6.1 Overview

Modeling can provide an understanding of the cooperative reaction and separation in the carbon molecular sieve hollow fiber membrane reactor, which will guide the membrane and catalyst development, experimental design of the membrane reactor, and selection of reaction conditions. In Chapter 6, we developed one-dimensional (1D) isothermal models for the carbon molecular sieve hollow fiber membrane reactor for propane dehydrogenation. Section 6.2 describes the governing equations of the 1D isothermal model. The PDH catalyst reaction rate equation was obtained by kinetic rate measurements of the catalyst. The CMS membrane permeation properties were obtained from high-temperature permeation tests in Chapter 4. Section 6.3 shows the modeling results of H_2-permeable PBMR. The impacts of reactor operating conditions and membrane properties on PBMR performance were predicted and compared with experimental membrane reactor results obtained in Chapter 5. Section 6.4 presents the modeling results of C_3H_6-permeable PBMR for PDH. The concept and advantages of C_3H_6-permeable PBMR are illustrated. The roles of sweep gas composition, membrane permeance, and C_3H_6/C_3H_8 selectivity on the C_3H_6-permeable PBMR performance are investigated. Section 6.5 discusses the modeling results of catalytic carbon molecular sieve membrane reactor (CMR) for PDH using a revised 1D isothermal model. The effects of catalyst loading, the number of catalytic

CMS fibers, and membrane permeance on performance were modeled. Section 6.6 summarizes the main findings of the modeling work.

6.2 Development of the 1D isothermal PBMR model

6.2.1 Material balance equations

The PBMR model includes the addition of membrane permeation flux compared to conventional packed bed reactor (PBR) model. Several assumptions were made for this 1D isothermal PBMR model: isothermal operation, plug flow inside the reactor, no axial dispersion, no radial diffusion, no mass transfer resistance, and no pressure drop along the packed catalyst bed. The material balance equations for gas component on the feed side and sweep side of PBMR are given below

Feed side $$\frac{dF_{f,i}}{dz} = \rho_c \pi \left({R_2}^2 - n{R_1}^2 \right) r_i - 2\pi n R_1 Q_i \left(P_{f,i} - P_{s,i} \right) \quad (6.1)$$

Sweep side $$\frac{dF_{s,i}}{dz} = 2\pi n R_1 Q_i \left(P_{f,i} - P_{s,i} \right) \quad (6.2)$$

where F_i (mol/s) is the molar flow rate of component i, z (m) is the packed catalyst bed length, ρ_c (g/m^3) is the catalyst packing density, R_1 (m) is the outer radius of hollow fiber, R_2 (m) is the inner radius of the quartz tube, n is the number of CMS hollow fibers, r_i (mol/s/g_{cat}) is the rate of reaction, Q_i (mol/s/m^2/atm) is the gas permeance, P_i (atm) is the partial pressure of component i. The subscripts f and s denote the feed and sweep side, respectively.

The pressure of the feed and sweep side was considered constant, typically 1 atm. At each step along the reactor catalyst bed length, the partial pressures of gas components were calculated from the component molar flow rate ratio multiplying total

pressure for feed and sweep side. The differential equations were solved using the Runge-Kutta method in MATLAB. The propane conversion in the PBMR is defined as

$$\chi_{C_3H_8}(\%) = \frac{F^{in}_{C_3H_8} - \left(F^{out}_{C_3H_{8,feed}} + F^{out}_{C_3H_{8,sweep}}\right)}{F^{in}_{C_3H_8}} \times 100\% \quad (6.3)$$

where $F^{out}_{C_3H_{8,feed}}$ and $F^{out}_{C_3H_{8,sweep}}$ are the propane flow rates at the outlet of the feed and sweep sides of the reactor, respectively.

6.2.2 Reaction kinetics of propane dehydrogenation

Langmuir-Hinshelwood (L-H) mechanism was proposed for propane activation over the platinum-zinc/silicalite-1 (Pt-Zn/S1) catalyst. This mechanism has been applied to the Pt-based catalysts for PDH in literature.[177-179] The elementary reaction steps in the L-H mechanism are shown below

$$C_3H_8 + 2* \overset{K_1}{\leftrightarrow} C_3H_7{}^* + H^* \quad \text{(Step 1, RLS)}$$

$$C_3H_7{}^* + * \overset{K_2}{\leftrightarrow} C_3H_6{}^* + H^* \quad \text{(Step 2)}$$

$$C_3H_6{}^* \overset{K_3}{\leftrightarrow} C_3H_6 + * \quad \text{(Step 3)}$$

$$2H^* \overset{K_4}{\leftrightarrow} H_2 + 2* \quad \text{(Step 4)}$$

The reaction starts from dissociative adsorption of propane on the active site (*) of the catalyst, producing C_3H_7* and H* species (Step 1). Activated C_3H_7* species undergoes a surface dehydrogenation reaction to form C_3H_6* and H* species (Step 2). Then C_3H_6* desorbs from the active site to produce propylene and release the active site (Step 3). The adsorbed hydrogen species desorbs to produce hydrogen gas co-product and release the active sites (Step 4). The propane activation is assumed to be

the rate limiting step (RLS) in the reaction mechanism scheme. Based on reaction mechanism Step 1, the C_3H_8 reaction rate ($r_{C_3H_8}$) is

$$r_{C_3H_8} = r_1 = k_1^+ p_{C_3H_8} \theta_*^2 - k_1^- \theta_{C_3H_7} \theta_H \tag{6.4}$$

where k_1^+ is the rate constant of forward reaction, $p_{C_3H_8}$ is the C_3H_8 partial pressure in the feed, θ_* is the fraction of free active sites, k_1^- is the rate constant of backward reaction, $\theta_{C_3H_7}$ is the fraction of active sites occupied by C_3H_7 species, and θ_H is the fraction of active sites occupied by H species, respectively. The equilibrium constant K_1 is defined by $K_1 = k_1^+/k_1^-$ in the Step 1. Then the quasi-equilibrium approximation is applied to Step 2-4

$$r_2 = k_2^+ \theta_{C_3H_7} \theta_* - k_2^- \theta_{C_3H_6} \theta_H \approx 0 \tag{6.5}$$

$$r_3 = k_3^+ \theta_{C_3H_6} - k_3^- p_{C_3H_6} \theta_* \approx 0 \tag{6.6}$$

$$r_4 = k_4^+ \theta_H^2 - k_4^- p_{H_2} \theta_*^2 \approx 0 \tag{6.7}$$

where k_2^+ and k_2^-, k_3^+ and k_3^-, and k_4^+ and k_4^-, are the forward and backward rate constants for Step 2-4, respectively. The $p_{C_3H_6}$ and p_{H_2} are partial pressures of C_3H_6 and H_2 in the reaction. The expressions for $\theta_{C_3H_7}$, $\theta_{C_3H_6}$(i.e., fraction of active sites occupied by C_3H_6 species), and θ_H were obtained below

$$\theta_{C_3H_6} = \frac{p_{C_3H_6} \theta_*}{K_3} \tag{6.8}$$

$$\theta_H = \frac{\sqrt{p_{H_2}}\, \theta_*}{\sqrt{K_4}} \tag{6.9}$$

$$\theta_{C_3H_7} = \frac{p_{C_3H_6} \sqrt{p_{H_2}}\, \theta_*}{K_2 K_3 \sqrt{K_4}} \tag{6.10}$$

where K_2, K_3, and K_4 are defined by the ratios of k_2^+/k_2^-, k_3^+/k_3^-, and k_4^+/k_4^- in Step 2-4, respectively. From the site balance equation (i.e., $\theta_* + \theta_{C_3H_7} + \theta_{C_3H_6} + \theta_H = 1$) of active sites in the catalyst, the expression for θ_* was obtained

$$\theta^* = \frac{1}{1 + \frac{p_{C_3H_6}}{K_3} + \frac{\sqrt{p_{H_2}}}{\sqrt{K_4}} + \frac{p_{C_3H_6}\sqrt{p_{H_2}}}{K_2K_3\sqrt{K_4}}} \quad (6.11)$$

After substituting $\theta_{C_3H_7}$, θ_H and θ^* into Eqn. 6.4, the rate equation for C_3H_8 consumption is

$$r_{C_3H_8} = \frac{k_1^+ p_{C_3H_8} - \frac{p_{C_3H_6}p_{H_2}}{K}}{\left(1 + \frac{p_{C_3H_6}}{K_3} + \frac{\sqrt{p_{H_2}}}{\sqrt{K_4}} + \frac{p_{C_3H_6}\sqrt{p_{H_2}}}{K_2K_3\sqrt{K_4}}\right)^2} \quad (6.12)$$

in which K is defined as, $K = \frac{K_2K_3K_4}{k_1^-}$.

The experiments for kinetic parameters measurements were summarized in **Table 6.1** and were conducted by Antara Bhowmick from Prof. Dongxia Liu's group. The obtained reaction rate constants (k_1^+ or k_1^-) for PDH over the Pt-Zn/S1 catalyst at different temperatures are used to calculate the activation energies E_a and pre-exponential factors k_0 using Arrhenius equation (Eqn. 6.13). By plotting the natural logarithm of rate constant versus the inverse temperature (Eqn. 6.14), k_0 and Ea can be calculated from the intercept and slope of the plot, respectively. Similarly, the obtained equilibrium constants at different temperatures are used to determine the adsorption energies ΔH and pre-exponential factors K_0 using van't Hoff equation (Eqn. 6.15). By plotting the natural logarithm of equilibrium constant versus the inverse temperature (Eqn. 6.16), K_0 and ΔH can be calculated from the intercept and slope of the plot, respectively. The final reaction kinetics values were kindly provided by Antara

Bhowmick and were summarized in **Table 6.2**. Using Eqn. 6.13 and Eqn. 6.15, the rate equation developed for Pt-Zn/S1 catalyst in this study can be broadly applied to different PDH reaction conditions.

$$\mathrm{k} = \mathrm{k_0 e}^{\left(-\frac{\mathrm{E_a}}{\mathrm{RT}}\right)} \tag{6.13}$$

$$\ln(\mathrm{k}) = \ln(\mathrm{k_0}) + \left(-\frac{E_a}{R}\right)\frac{1}{T} \tag{6.14}$$

$$\mathrm{K} = \mathrm{K_0 e}^{\left(-\frac{\Delta \mathrm{H}}{\mathrm{RT}}\right)} \tag{6.15}$$

$$\ln(\mathrm{K}) = \ln(\mathrm{K_0}) + \left(-\frac{\Delta H}{R}\right)\frac{1}{T} \tag{6.16}$$

Table 6.1. Experiments for Pt-Zn/S1 catalyst kinetics parameters determination in the PDH reaction rate equation. (Provided by Antara Bhowmick)[171]

Experiments	**Reaction conditions**			
Forward reaction	T (°C)	$p_{C_3H_8}$ (kPa)	p_{H_2} (kPa)	$p_{C_3H_6}$ (kPa)
Exp. 1	350-400	25-75	0	0
Exp. 2	350-400	50	0-20	0
Exp. 3	400-435	25-45	0	2.5
Backward reaction	T (°C)	$p_{C_3H_8}$ (kPa)	p_{H_2} (kPa)	$p_{C_3H_6}$ (kPa)
Exp. 4	90-125	0	2.5	1.25-7.5

Table 6.2. Summary of k_0 and E_a for reaction rate constants and K_0 and ΔH for equilibrium constants for PDH over the Pt-Zn/S1 catalyst. (Provided by Antara Bhowmick)[171]

Kinetic parameters		**Values**	
Reaction rate constant	**Unit**	**k_0**	**E_a** (kJ/mol)
k_1^+	$mol \cdot s^{-1} \cdot g_{cat}^{-1} \cdot kPa^{-1}$	0.9192	89.3
k_1^-	$mol \cdot s^{-1} \cdot g_{cat}^{-1}$	1.392	35.3
Equilibrium constant	**Unit**	**K_0**	**ΔH** (kJ/mol)
K_2	dimensionless	158.6	16.6
K_3	kPa	257.5	9.1
K_4	kPa	1.076×10^6	66.2

6.2.3 CMS hollow fiber membrane separation performance under PDH conditions

High-temperature mixed-gas permeation tests were performed on CMS hollow fiber membranes to study membrane separation performance under PDH conditions. The feed mixture includes both reactant and products, i.e., $5\%H_2/5\%C_3H_6/40\%C_3H_8/50\%Ar$ (20 mL/min), to simulate the PDH reaction gas atmosphere. The permeation temperature varied from 350 to 500 ºC, corresponding to the reaction temperature used for the membrane reactor. The testing CMS membrane was pyrolyzed at 550 ºC and a hollow fiber membrane module was constructed for permeation tests. The sweep gas was 20 mL/min Ar flowing through the hollow fiber bore side to carry away the permeated gas molecules. **Table 6.3** presented CMS membrane gas permeances and separation factors at each permeation temperature, which were directly applied to the modeling equations.

Table 6.3. Summary of high-temperature $H_2/C_3H_6/C_3H_8$ separation performance in CMS hollow fiber membranes.

Permeation T (°C)	P(H_2) (GPU)	P(C_3H_6) (GPU)	P(C_3H_8) (GPU)	α (H_2/C_3H_8)	α (H_2/C_3H_6)	α (C_3H_6/C_3H_8)
350	231	12.0	1.4	144	16.9	8.5
400	234	10.2	1.1	179	19.9	9.0
450	234	8.7	0.92	221	23.4	9.4
500	229	7.0	0.68	293	28.5	10.3

6.3 Modeling of H_2-permeable membrane reactor

6.3.1 Comparing molar flow rate profiles in the PBR and PBMR

In H_2-permeable PBMR, H_2 permeation from reaction side to permeate side breaks PDH thermodynamic equilibrium, thereby increasing the conversion. The molar flow rate profiles in PBR and PBMR during PDH reaction are shown in **Figure 6.1**. In PBR, the C_3H_8, C_3H_6, and H_2 molar flow rates remain constant after reaching equilibrium. In PBMR, the reaction side C_3H_8 molar flow rate keeps decreasing along the reactor length with increasing C_3H_6 molar flow rate. The H_2 molar flow rate first increased due to PDH reaction and then decreased over the catalyst bed length because of continuous permeation to the sweep side (**Figure 6.1 D**). The conversion obtained in PBMR is highly dependent on the operating conditions and membrane properties. **Table 6.4** summarizes the investigated parameters in the modeling of H_2-permeable membrane reactor. The interplay between reactor operating conditions and membrane properties is studied.

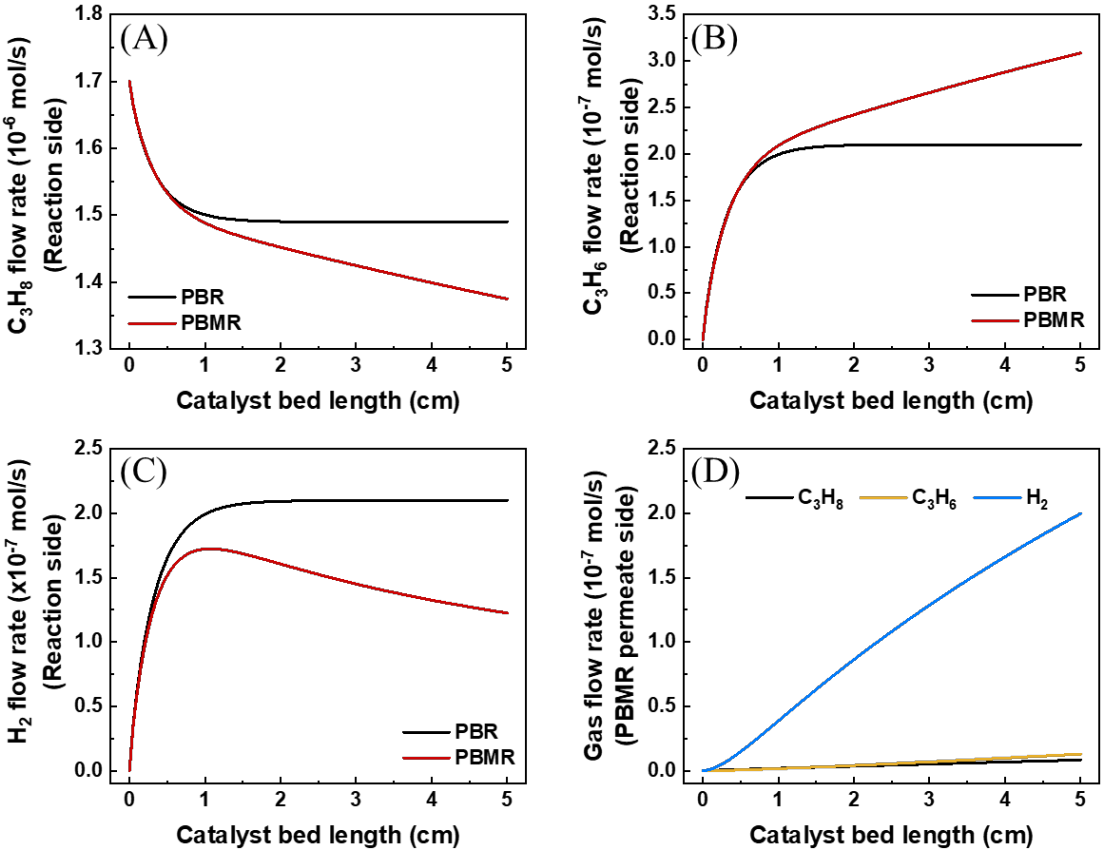

Figure 6.1. Modeling gas molar flow rate profiles in the PBR and PBMR. (A) C_3H_8, (B) C_3H_6, and (C) H_2 in PBR and PBMR reaction (feed) side. (D) H_2 in PBMR permeate (sweep) side. PBR modeling conditions: feed 1.73 h^{-1} (50%C_3H_8/50%Ar), reaction temperature 450 ºC, catalyst mass 0.3g. PBMR modeling conditions: same as PBR with addition of 5 CMS hollow fibers, sweep 100 mL/min Ar, gas permeances at 450 ºC were taken from **Table 6.3**.

Table 6.4. Summary of operating parameters in H_2-permeable PBMR for PDH.

Operating conditions	**Unit**	**Experimental**	**Modeling**
Reaction temperature	^oC	350-500	350-650
WHSV[a]	h^{-1}	0.35-3.75	0.175-6.92
Sweep flow rate	mL/min	10-200	1-200
C_3H_8 feed partial pressure[b]	kPa	10-80	1-100
Feed side pressure	atm	1	1-5
Number of CMS fiber	-	0-9	0-9
Constant parameters	**unit**	**Value**	
Pt-Zn/S1 catalyst mass	g	0.3	
Catalyst packing density	g/m^3	4.039×10^5	
Sweep side pressure	atm	1	
CMS fiber outer radius	mm	0.168	
Quartz reactor inner radius	mm	2.175	

[a] feed composition 50%C_3H_8/50%Ar, [b] C_3H_8 feed balanced with Ar.

6.3.2 Effect of reaction temperature

The impact of reaction temperature on PDH conversions in PBMR was investigated in the range of 350-650 ^oC (**Figure 6.2**). With an increase in temperature, both C_3H_8 conversion in PBMR and equilibrium conversion increased due to endothermic nature of PDH. The 1D isothermal PBMR model accurately predicted the C_3H_8 conversion from 350-500 ^oC as compared to the experimental results, suggesting the validity of the model. Based on the trend of measured gas permeances at 350-500 ^oC, H_2 permeance was assumed 230 GPU at 550-650 ^oC while the C_3H_6 and C_3H_8

permeances were assumed to decrease by 20% with every 50 °C increase of temperature. With the reaction temperature of 650 °C, the simulated C_3H_8 conversion in PBMR reached 92%. In commercial PDH processes, Catofin® for example, the conversion is 40~45% at temperatures 560-650 °C, feed pressure 0.2-0.5 bar and WHSV <1 h^{-1}.[11] The modeling results showed the great advantages of PBMR in terms of conversion enhancements.

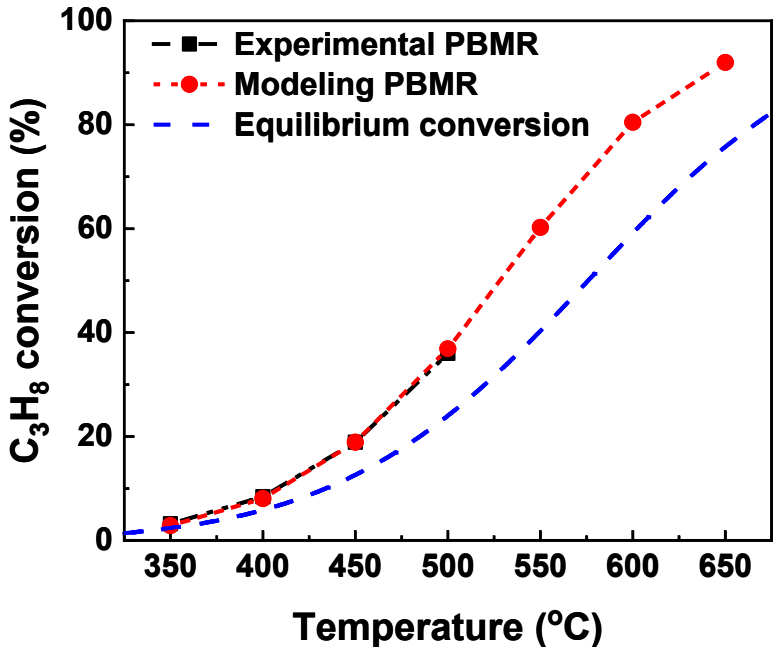

Figure 6.2. Impact of reaction temperature on PDH conversion in PBMR. The modeling data were compared to experimental results at 350-500 °C and then predicted the C_3H_8 conversion at 550-650 °C. The equilibrium line was presented to illustrate conversion enhancement in PBMR. Modeling conditions: feed 1.73 h^{-1} (50%C_3H_8/50%Ar), sweep 100 mL/min Ar, catalyst mass 0.3 g, 5 CMS hollow fibers, gas permeances were taken from **Table 6.3**.

6.3.3 Effect of feed weight hourly space velocity (WHSV)

Operation at high weight hourly space velocity (WHSV) is desirable as it increases the reactor's processing capability. The impact of feed WHSV on PDH conversions in PBMR was modeled in the range of 0.175-6.92 h^{-1} (**Figure 6.3**). The

model shows that the PBMR has outstanding C_3H_8 enhancement at low WHSV of 0.175 h^{-1}. As the WHSV increases, the C_3H_8 conversion drops and eventually approaches the equilibrium conversion at high WHSV of 6.92 h^{-1}. The model has good agreement with experimental results at WHSV of 0.35-3.46 h^{-1}. The model slightly overestimated the C_3H_8 conversion at lower WHSV. This may be due to the inaccurate output of the mass flow controller as the flow rate set point approaches the lower limit of the instrument.

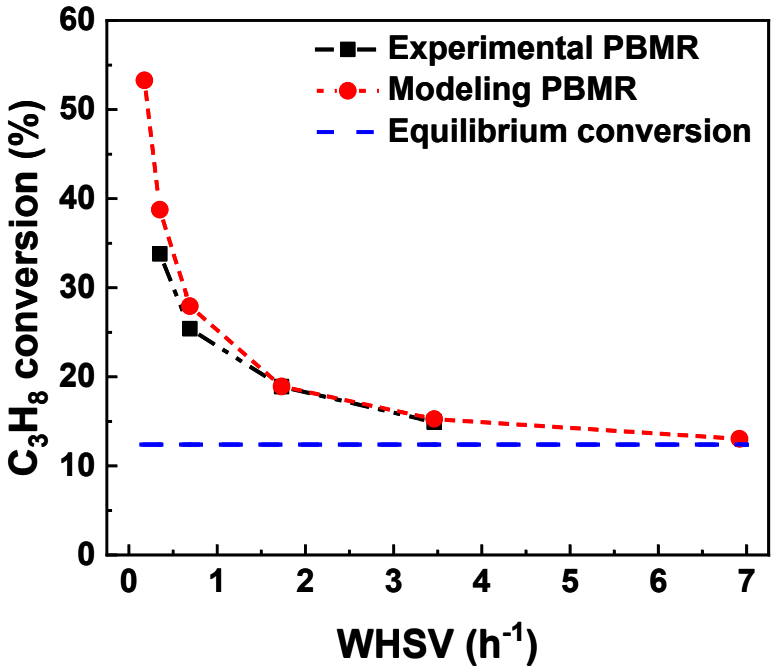

Figure 6.3. Impact of WHSV on PDH conversion in PBMR. The modeling data were compared to experimental results at 0.35-3.46 h^{-1} and then predicted the C_3H_8 conversion at 0.175 h^{-1} and 6.92 h^{-1}. The equilibrium line was drawn to show conversion enhancement in PBMR. Modeling conditions: feed 50%C_3H_8/50%Ar, reaction temperature 450 °C, sweep 100 mL/min Ar, catalyst mass 0.3 g, 5 CMS hollow fibers, gas permeances at 450 °C were taken from **Table 6.3**.

6.3.4 Effect of sweep flow rate

The impact of sweeping gas flow rate on PDH conversions in PBMR was simulated using 1-200 mL/min Ar sweep (**Figure 6.4**). The model predicts that the

C_3H_8 conversion increased with increasing sweep flow rate in PBMR, which was in excellent consistency with experimental results (**Figure 6.4A**). With an increase in sweep flow rate, the H_2 partial pressure in the sweep side decreases (**Figure 6.4B**). The increased H_2 partial pressure difference across the membrane provides a larger driving force for H_2 permeation, leading to higher H_2 removal rate from the feed side to the permeate side. The model suggests that the conversion of the PBMR can be negatively affected if the sweep flow rate is smaller than 10 mL/min. It also suggests negligible increase in conversion can be obtained by increasing the sweep flow rate beyond 50 mL/min because the H_2 partial pressure in the sweep side is already close to zero (**Figure 6.4 B**).

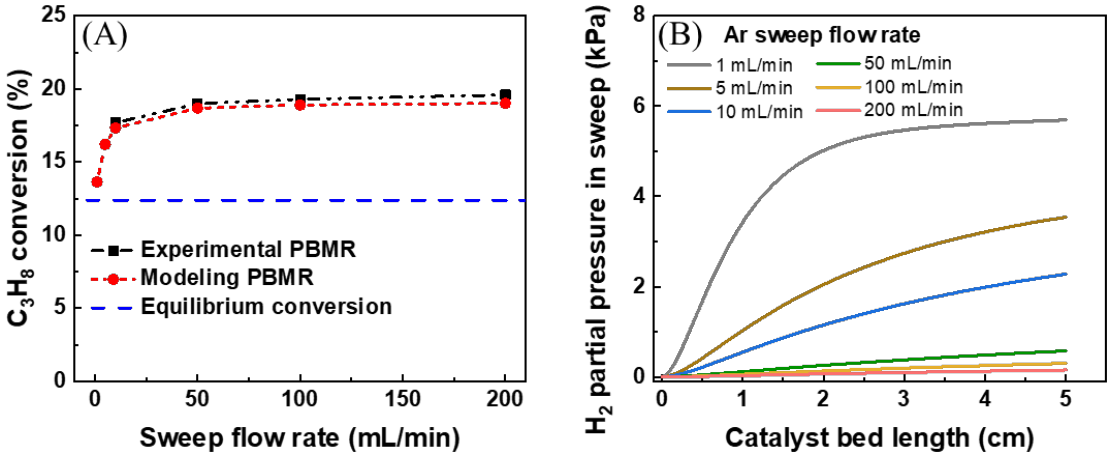

Figure 6.4. (A) Impact of sweep flow rate (1-200 mL/min) on PDH conversion in PBMR. The equilibrium line was drawn to show conversion enhancement in PBMR. (B) H_2 partial pressure along the catalyst bed in the PBMR sweep side. Modeling conditions: feed 1.73 h^{-1} (50%C_3H_8/50%Ar), reaction temperature 450 ºC, catalyst mass 0.3 g, 5 CMS hollow fibers, gas permeances at 450 ºC were taken from **Table 6.3**.

6.3.5 Effect of feed reactant partial pressure

The role of C_3H_8 feed partial pressure on PDH conversions in PBMR was investigated in the range of 1-100 kPa. With decreasing C_3H_8 feed partial pressure, both

the PBMR conversion and equilibrium conversion increased (**Figure 6.5**). Since the feed is C_3H_8 balanced with Ar, the partial pressures of both C_3H_8 and products (H_2 and C_3H_6) decrease with increasing Ar percentage in the feed, leading to the equilibrium shift to the product side according to Le Chatelier's principle. The modeling results have excellent consistency with the experimental PBMR results.

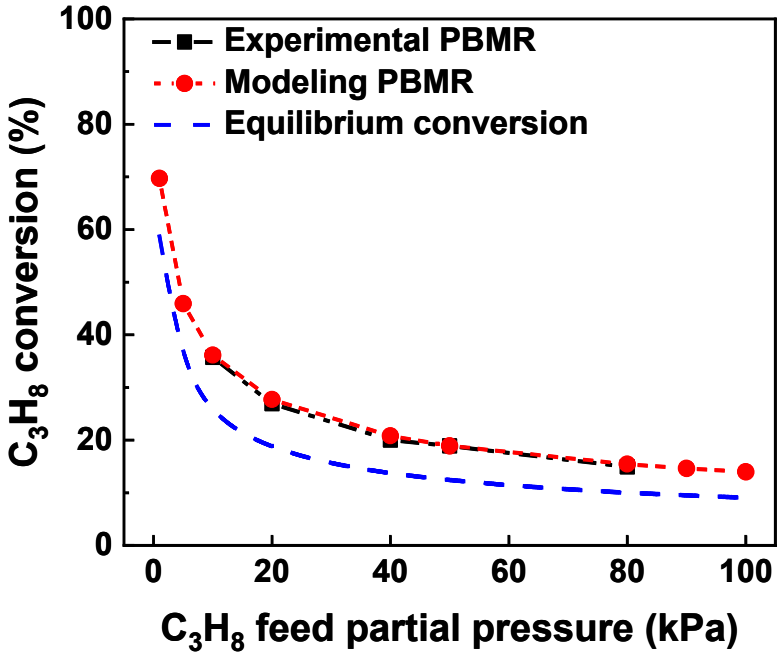

Figure 6.5. Impact of C_3H_8 feed partial pressure on PDH conversion in PBMR. The modeling data were compared to experimental results at 10-80 kPa C_3H_8 feed and then predicted the C_3H_8 conversion at 1-10 kPa and 80-100 kPa C_3H_8 feed. The equilibrium line was drawn to show conversion enhancement in PBMR. Modeling conditions: total feed flow rate 5 mL/min, reaction temperature 450 ºC, sweep 100 mL/min Ar, catalyst mass 0.3 g, 5 CMS hollow fibers, gas permeances at 450 ºC were taken from **Table 6.3**.

6.3.6 Effect of feed total pressure

The PBMR was simulated in the range of 1-5 atm feed total pressure at constant feed reactant molar concentration of 50%. The model suggests that the C_3H_8 conversion of the PBMR reactor almost remains constant as the feed total pressure increased from 1 to 5 atm (**Figure 6.6**). Because PDH is a volume expanse reaction, larger feed total

pressure shifts the equilibrium to the reactant side. However, larger feed total pressure also increases the permeation driving force, thereby offsetting the thermodynamic effects.

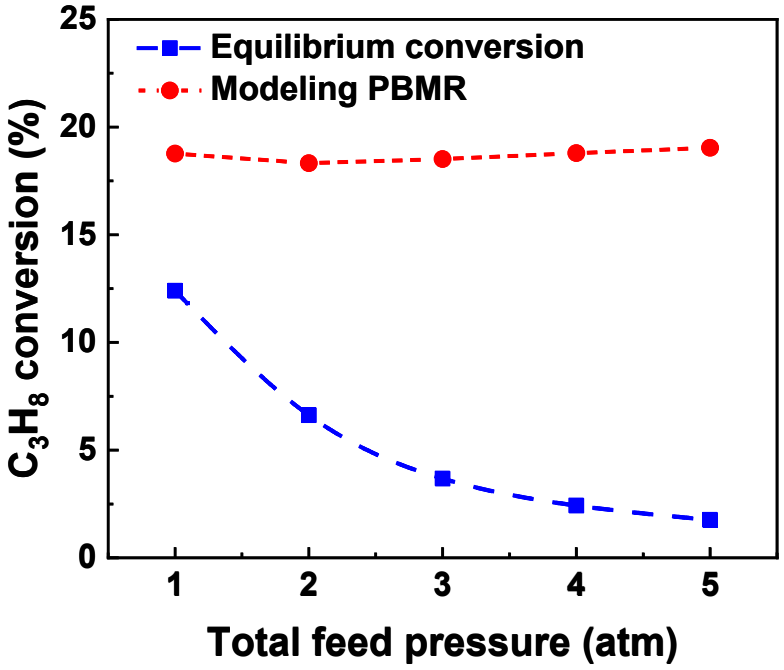

Figure 6.6. Modeling results of PDH conversion in PBMR with respect to feed pressure. The equilibrium line was drawn to show conversion enhancement in PBMR. Modeling conditions: feed 1.73 h^{-1} (50%C_3H_8/50%Ar), reaction temperature 450 ºC, sweep 100 mL/min Ar, catalyst mass 0.3 g, 5 CMS hollow fibers, gas permeances at 450 ºC were taken from **Table 6.3**.

6.3.7 Effect of membrane separation area

The model suggests that larger membrane area (controlled by the number of CMS hollow fiber membranes) leads to higher C_3H_8 conversion (**Figure 6.7**). A larger membrane area allows more H_2 to permeate from the reaction side to the sweep side, thereby shifting the equilibrium to the product side to increase C_3H_8 conversion. The model successfully predicted C_3H_8 conversion in the 3-fiber PBMR. However, the 5-fiber PBMR, 9-fiber PBMR and 19-fiber PBMR showed lower C_3H_8 conversion than the model prediction. The lower C_3H_8 conversion was likely because the membrane H_2

permeance reduces as an increasing number of fibers are pyrolyzed. This indicates that scaling up of CMS hollow fiber membrane formation must be optimized to give consistent H_2 permeance.

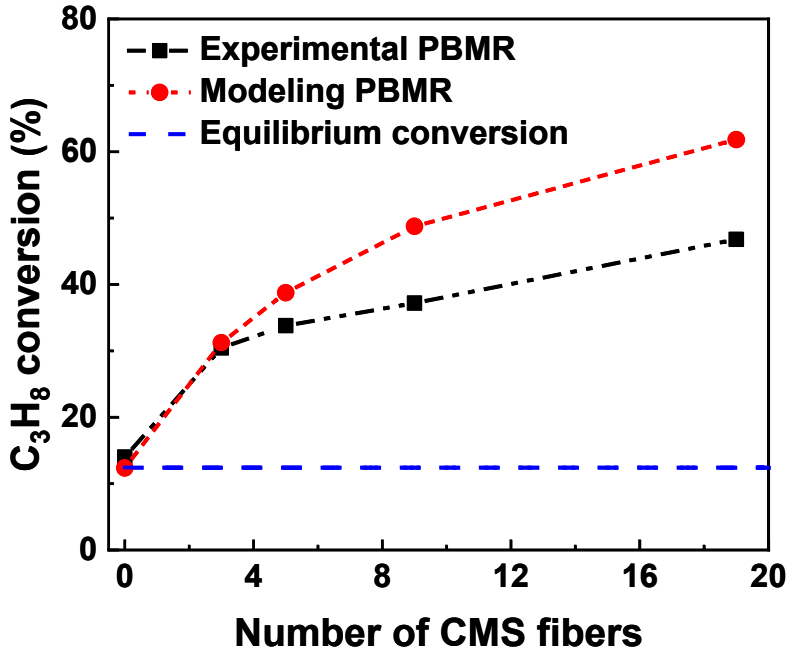

Figure 6.7. Impact of number of CMS fibers on PDH conversion in PBMR. The modeling data were compared to experimental results at 0-9 CMS hollow fibers. The equilibrium line was drawn to show conversion enhancement in PBMR. Modeling conditions: feed 1.73 h^{-1} (50%C_3H_8/50%Ar), reaction temperature 450 ºC, sweep 100 mL/min Ar, catalyst mass 0.3 g, gas permeances at 450 ºC were taken from **Table 6.3**.

6.3.8 Effect of H_2 permeance

The impact of H_2 permeance on PDH conversions in PBMR was simulated in the range of 234-2000 GPU (**Figure 6.8**). The model shows that higher C_3H_8 conversion can be obtained as the membrane H_2 permeance is increased. Higher H_2 permeance leads to faster H_2 permeation through the membrane, thereby allowing more effective H_2 removal from the reaction side. In addition, applying high H_2 permeance membranes helps reduce the number of incorporated CMS fibers in the PBMR. For example, a membrane with 2000 GPU H_2 permeance plays the same role as 10 CMS

fibers with 200 GPU H_2 permeance. The results suggest that it will be highly attractive to enhance the PBMR performance by enhancing the membrane H_2 permeance, which can be achieved by reducing the membrane separation layer thickness.

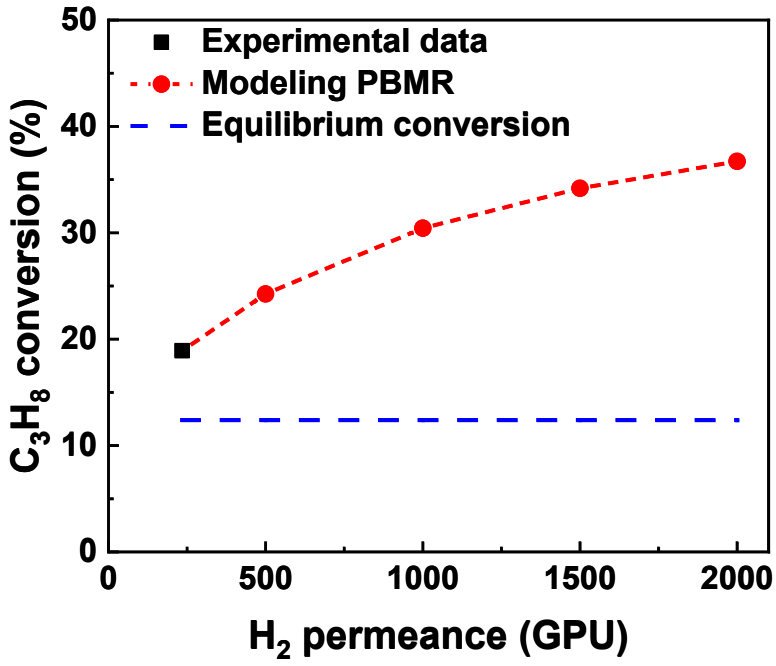

Figure 6.8. Impact of H_2 permeance on PDH conversion in PBMR. The equilibrium line was drawn to show conversion enhancement in PBMR. Modeling conditions: feed 1.73 h^{-1} (50%C_3H_8/50%Ar), reaction temperature 450 °C, sweep 100 mL/min Ar, 5 CMS hollow fibers, catalyst mass 0.3 g. The CMS membrane selectivity is fixed using the separation factor provided by **Table 6.3**.

6.3.9 Effect of H_2/C_3H_8 selectivity

The role of H_2/C_3H_8 selectivity on PDH conversions in PBMR was simulated in the range of 1-500 (**Figure 6.9**). According to the modeling results, the PBMR conversion increased as the H_2/C_3H_8 selectivity increased from 1 to 50. Low H_2/C_3H_8 selectivity can lead to reactant (C_3H_8) loss to the permeate side and therefore reduced C_3H_8 conversion. The model shows that increasing H_2/C_3H_8 selectivity beyond 50 has negligible effects on enhancing C_3H_8 conversion and using membranes with H_2/C_3H_8 selectivity significantly higher than 50 is not necessary. At constant membrane

separation layer thickness, there is often a trade-off in membrane permeance and selectivity. Hence, membranes with H_2/C_3H_8 selectivity~50 is optimal under the studied conditions.

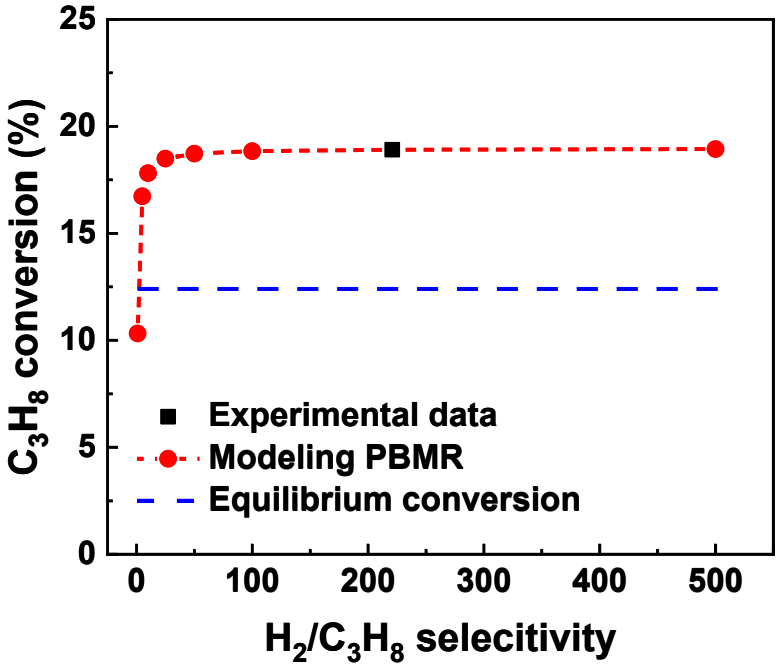

Figure 6.9. Impact of H_2/C_3H_8 selectivity on PDH conversion in PBMR. The equilibrium line was drawn to show conversion enhancement in PBMR. Modeling conditions: feed 1.73 h^{-1} (50%C_3H_8/50%Ar), reaction temperature 450 °C, sweep 100 mL/min Ar, 5 CMS hollow fibers, catalyst mass 0.3 g, H_2 and C_3H_6 permeances are fixed and are taken from **Table 6.3**.

6.4 Modeling of C_3H_6-permeable membrane reactor

The C_3H_8 conversion of PDH membrane reactor can be enhanced by either H_2 or C_3H_6 removal. So far, the C_3H_8 conversion enhancements in all reported PDH membrane reactors are driven by H_2 removal (i.e., H_2-permeable membrane reactor). To our best knowledge, there have not been reports on PDH membrane reactors that C_3H_8 conversion enhancements are driven by C_3H_6 removal (i.e., C_3H_6-permeable membrane reactor). This is possibly because most membranes have much higher H_2 permeance than C_3H_6 permeance. Also, few membranes can provide attractive

C_3H_6/C_3H_8 selectivity at PDH reaction conditions. In H_2-permeable PDH membrane reactors, both catalyst and membrane can suffer from deactivation due to coking caused by depletion of H_2.[22, 23, 180, 181] The kinetics of coking on Pt-based PDH catalysts were investigated on butane dehydrogenation. The coke formation rate of Pt/Al_2O_3 catalysts (Eqn 6.17) is inversely proportional to H_2 partial pressure.[182] The mechanistic study indicates that the removal of H_2 from the membrane reactor deactivates catalyst while removing alkene from the reactor could suppress coke formation and hence improve membrane reactor stability.

$$r_c = \frac{k_c p_{C_4H_8}}{1 + k_1' p_{H_2}^{0.5}} \tag{6.17}$$

where k_c and k_1' are kinetic parameters derived from experiments.[182]

6.4.1 Effects of sweep H_2 concentration

H_2 permeation must be restricted to enable the C_3H_6-permeable membrane reactor concept. Restricting H_2 permeation can be realized by mixing H_2 in the permeate side sweep gas. Mixing H_2 in the sweep gas can reduce the H_2 partial pressure difference across the membrane and hence the driving force for H_2 permeation. The C_3H_6-permeable membrane reactor was modeled with 0-6% H_2 in sweep. The model used a hypothetical CMS hollow fiber membrane that has identical $H_2/C_3H_6/C_3H_8$ selectivity with the membrane shown in **Table 6.3** but a much thinner separation layer of 100 nm. The membrane thus provides C_3H_6 permeance of 435 GPU at 450 ºC. Considering the high gas permeance, larger sweep flow rate (1L/min) is applied in the modeling to effectively remove permeated molecules and provide sufficient gas permeation driving forces.

The model shows that the reaction side H_2 partial pressure can be controlled by H_2 concentration in the sweep, i.e., reaction side H_2 partial pressure increases with higher H_2 concentration in the sweep (**Figure 6.10**). Therefore, as the H_2 concentration in the sweep increased, less H_2 permeation occurs and the PDH membrane reactor becomes less driven by H_2 permeation and more driven by C_3H_6 permeation. At 0% H_2 in sweep, C_3H_8 conversion enhancement is the highest and it is driven by co-removal of H_2 and C_3H_6. As the H_2 concentration in the sweep increased, higher H_2 partial pressure in the reaction side reduced the overall reaction rate and hence the conversion enhancement dropped (**Figure 6.11**). Although less conversion enhancement is obtained by C_3H_6-permeable membrane reactor, it has the potential to provide better stability with more H_2 and less C_3H_6 retained in the reaction side. The modeling results suggest that sweep H_2 concentration is a powerful tool to control H_2 concentration in the reaction side to achieve a balance between conversion enhancement and membrane reactor stability.

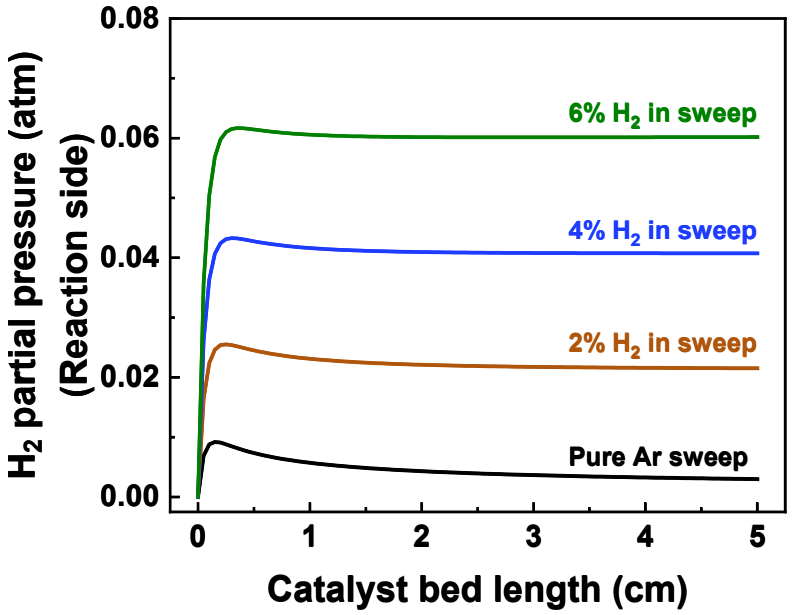

Figure 6.10. Modeling results of reaction side H_2 partial pressure along catalyst bed in C_3H_6-permeable PBMR. Modeling conditions: feed 1.73 h^{-1} (50%C_3H_8/50%Ar), reaction temperature 450 °C, sweep 1 L/min, 5 CMS hollow fibers, catalyst mass 0.3 g, gas permeances were 50 times as high as the values in **Table 6.3**.

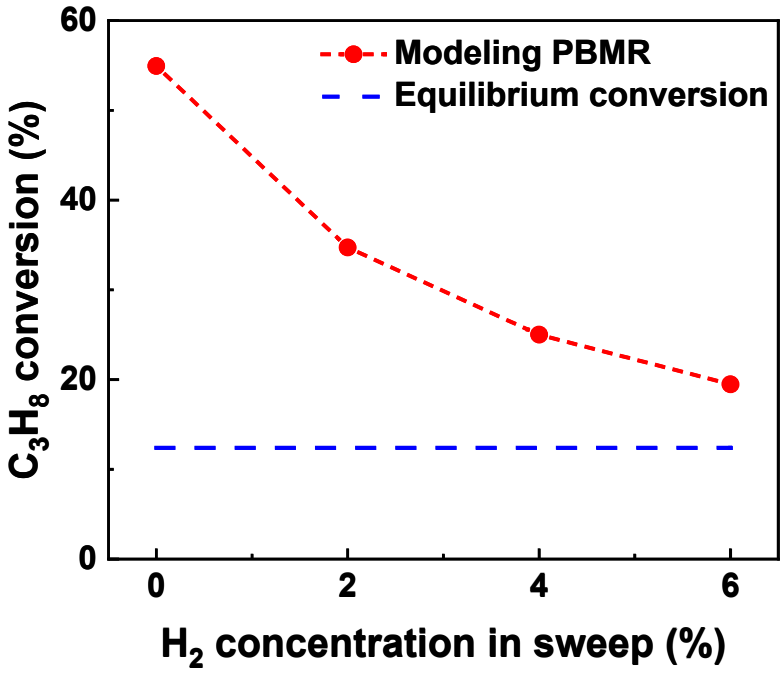

Figure 6.11. Impact of H_2 concentration in sweep on PDH conversion in C_3H_6-permeable PBMR. The equilibrium line was drawn to show conversion enhancement in membrane reactor. Modeling conditions: feed 1.73 h^{-1} (50%C_3H_8/50%Ar), reaction temperature 450 °C, sweep 1 L/min, catalyst mass 0.3 g, 5 CMS hollow fibers, gas permeances were 50 times as high as the values in **Table 6.3**.

6.4.2 Effects of C_3H_6 permeance

The effects of C_3H_6 permeance on C_3H_6-permeable PBMR performance were modeled in the range of 8.7-435 GPU (**Figure 6.12**). The C_3H_6 permeance range assumed the membrane separation layer thickness decreased from 5 μm to 100 nm with constant $H_2/C_3H_6/C_3H_8$ selectivity as provided in **Table 3**. The model shows that the C_3H_8 conversion increases with increasing C_3H_6 permeance due to faster gas removal rates during reaction. The results suggest that higher C_3H_6 permeance is preferred for the C_3H_6-permeable PBMR to obtain more attractive conversion enhancements, which

can be achieved by fabricating CMS hollow fiber membrane with ultrathin separation layers.

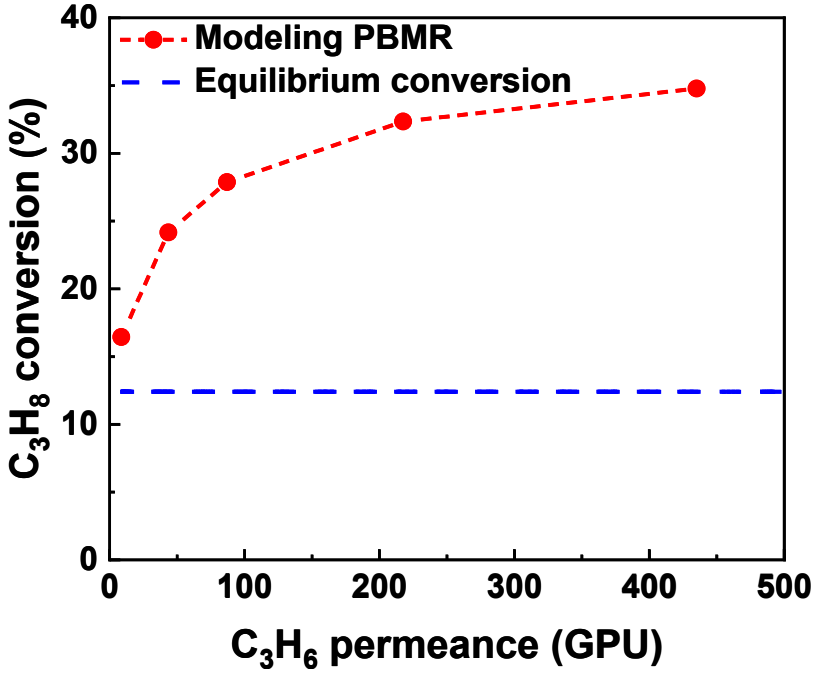

Figure 6.12. Impact of C_3H_6 permeance on PDH conversion in C_3H_6-permeable PBMR. The equilibrium line was drawn to show conversion enhancement in membrane reactor. Modeling conditions: feed 1.73 h^{-1} (50%C_3H_8/50%Ar), reaction temperature 450 °C, sweep 1 L/min 2%H_2/98%Ar, catalyst mass 0.3 g, 5 CMS hollow fibers.

6.4.3 Effects of C_3H_6/C_3H_8 selectivity

The impact of C_3H_6/C_3H_8 selectivity on PDH conversions in C_3H_6-permeable PBMR was modeled in the range of 1-50 (**Figure 6.13**). High C_3H_6/C_3H_8 selectivity is typically preferred to selectively remove C_3H_6 from the reaction side while minimizing the reactant C_3H_8 loss. As the C_3H_6/C_3H_8 selectivity increased from 1 to 10, the C_3H_8 conversion in the membrane reactor increased dramatically since more reactants are retained in the feed side for PDH reaction. Further C_3H_6/C_3H_8 selectivity increase from 10 to 50 gave negligible conversion improvement in the PBMR. The asymmetric CMS hollow fiber membranes showed C_3H_6/C_3H_8 separation factor ~8-10 under PDH

conditions (**Table 6.3**), suggesting that the C_3H_6-permeable CMS hollow fiber membrane reactor is feasible.

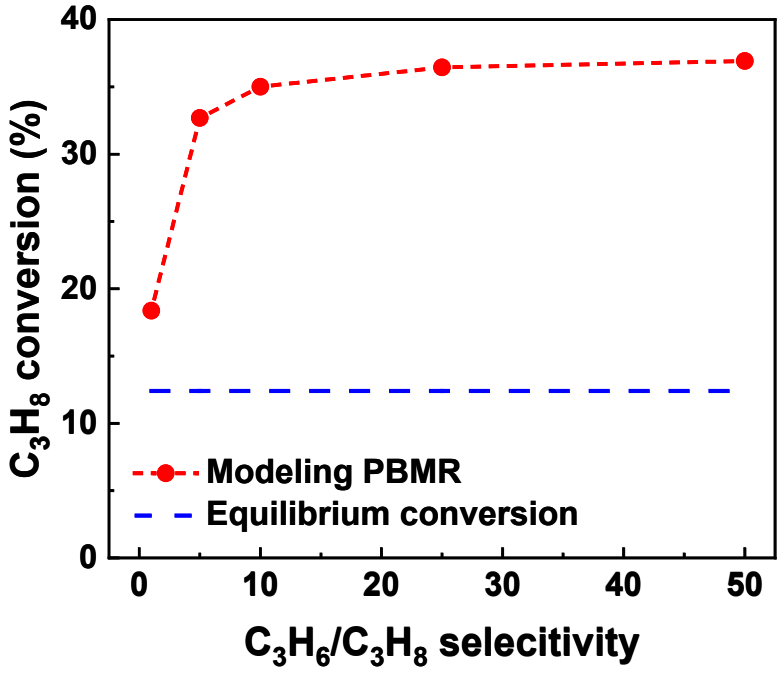

Figure 6.13. Impact of C_3H_6/C_3H_8 selectivity on PDH conversion in C_3H_6-permeable PBMR. The equilibrium line was drawn to show conversion enhancement in membrane reactor. Modeling conditions: feed 1.73 h^{-1} (50%C_3H_8/50%Ar), reaction temperature 450 °C, sweep 1 L/min 2%H_2/98%Ar, catalyst mass 0.3 g, 5 CMS hollow fibers, H_2 and C_3H_6 permeances are fixed and are 50 times as high as the values in **Table 6.3**.

6.5 Modeling of catalytic membrane reactor

A catalytic membrane reactor (CMR) integrates the reactor and separator in the same device.[183] A catalytic carbon molecular sieve hollow fiber membrane reactor is illustrated in **Figure 6.14**. The hollow fiber membrane reactor has a dense and permselective outside sheath layer free of catalysts and a meso-/macroporous inside core layer consisting of dispersed catalysts. As the reactant stream is introduced to one side of the inner bore, PDH reaction occurs on the dispersed catalysts in the core layer and the produced H_2 is selectively removed to the hollow fiber shell side by permeation through the dense sheath layer. The reaction conversion in conventional reactors is

often limited by the reactant diffusion to the catalyst pores. With catalyst particles dispersed inside the porous membrane substrate, the reactants have easier access to the catalyst due to the combination of membrane open pore path and transmembrane pressure.[184, 185] Previous studies showed that the activity of catalyst dispersed in membrane can be 10 times higher than catalyst in the form of pellet.[186] In addition, CMR fully utilizes the entire membrane separation area within the heating zone unlike PBMR where the effective membrane separation area is determined by the packed catalyst bed length.

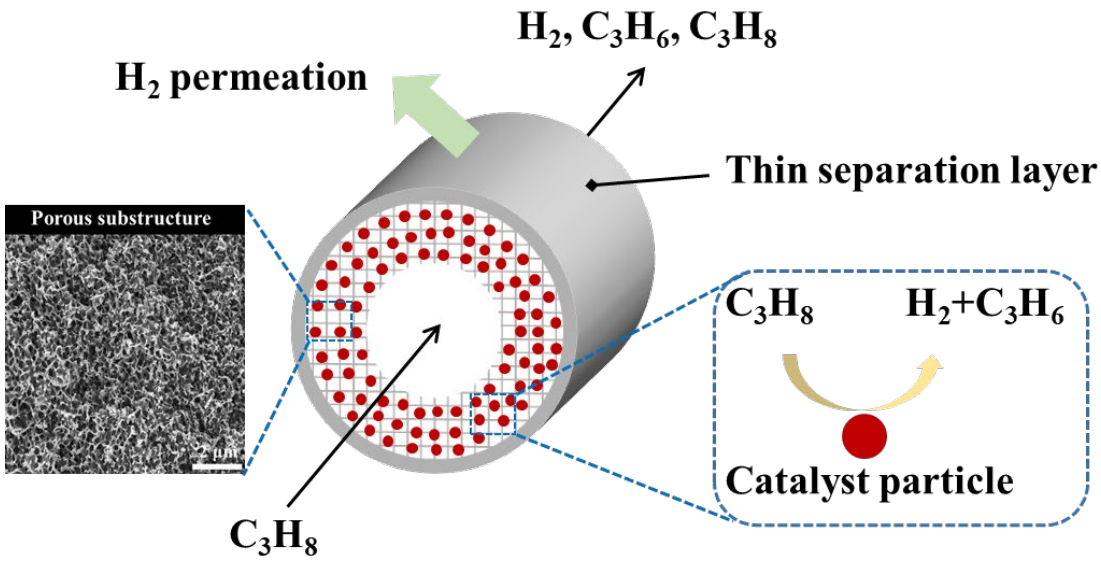

Figure 6.14. Schematic illustration of catalytic CMS hollow fiber membrane reactor for PDH.

A one-dimensional model is developed for the catalytic CMS hollow fiber membrane reactor

Feed side $$\frac{dF_{f,i}}{dz} = nm_c r_i - 2\pi n R_1 Q_i \left(P_{f,i} - P_{s,i}\right) \quad (6.18)$$

Sweep side $$\frac{dF_{s,i}}{dz} = 2\pi n R_1 Q_i \left(P_{f,i} - P_{s,i}\right) \quad (6.19)$$

where F_i (mol/s) is the molar flow rate of component i, z (m) is the reactor effective heating length, m_c (g_{cat}/m) is the catalyst mass per fiber length, R_1 (m) is the outer radius of hollow fiber, n is the number of catalytic CMS hollow fibers, r_i (mol/s/g_{cat}) is the rate of reaction, Q_i (mol/s/m^2/atm) is the gas permeance, P_i (atm) is the partial pressure of component i. The subscripts f and s denote the feed and sweep side, respectively.

Several assumptions were made for the 1D CMR model: isothermal operation, plug flow inside the reactor, no axial and radial dispersion in the core layer, no mass transfer resistance, and no pressure drop. Note that the hollow fiber bore side is the feed side and the hollow fiber shell side is the sweep side. The CMR model assumes that the catalytic membrane has the same permeances (separation layer ~5 μm) and selectivities as provided in **Table 6.3**. The current CMS hollow fiber (O.D. 315 μm) is 0.6 mg/cm. Taking 20 cm as the effective furnace heating length for PDH reaction, the mass of a single CMS fiber is 12 mg (fixed in this modeling work) within the heating zone. The catalyst loading determines the mass of the catalyst attending the PDH reaction.

6.5.1 Effects of catalyst loading

The catalyst loading percentage is defined as

$$W_{catalyst}(\%) = \frac{m_{catalyst}}{m_{catalyst} + m_{CMS\ fiber}} \times 100\% \qquad (6.20)$$

where $m_{catalyst}$ is the catalyst mass and $m_{CMS\ fiber}$ is the CMS fiber mass.

The impact of the catalyst loading in CMS fiber on the CMR performance was modeled in the range of 10-95 wt% (**Figure 6.15**). With increasing catalyst loading,

the C_3H_8 conversion in the 10-fiber CMR increases due to reduced WHSV. The conversion exceeded equilibrium conversion at catalyst loading above 30%, which demonstrates the viability of the CMR.

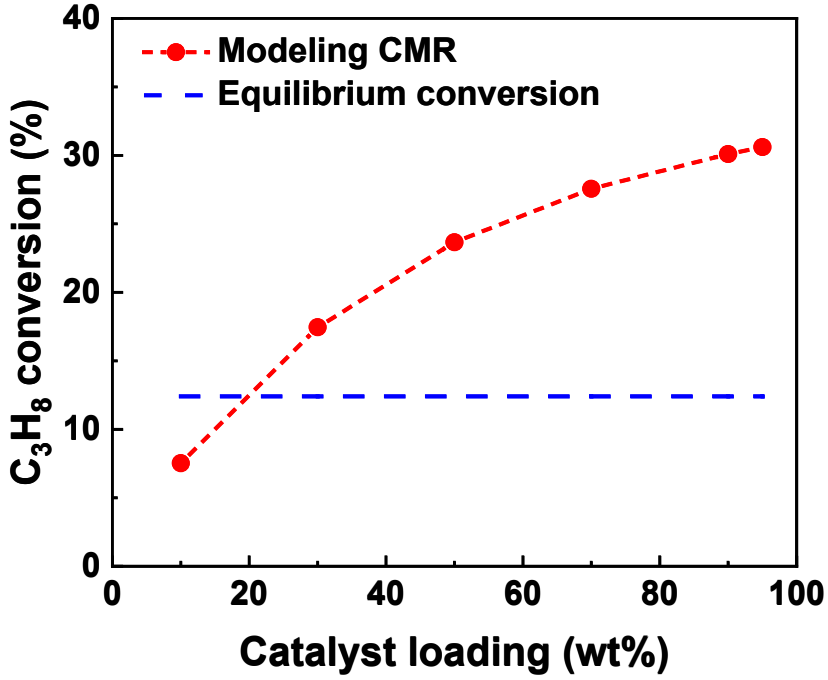

Figure 6.15. The effect of catalyst loading percentage on PDH conversion in CMR. The equilibrium line was drawn to show conversion enhancement in CMR. Modeling conditions: feed 1.73 h^{-1} (50%C_3H_8/50%Ar), reaction temperature 450 ºC, sweep 100 mL/min Ar, 10 catalytic CMS hollow fibers, gas permeances at 450 ºC were taken from **Table 6.3**

6.5.2 Effects of the number of catalytic fibers

Another key parameter in CMR is the number of catalytic CMS hollow fibers since it determines both catalyst mass and membrane separation area. The revised 1D isothermal model predicted the PDH conversions in CMR in the range of 5-50 catalytic CMS fibers (**Figure 6.16**). The C_3H_8 conversion in CMR increased with increasing CMS fibers. With 50 catalytic CMS fibers, the predicted conversion in CMR is 45% at 450 ºC, which is 263% higher than the equilibrium conversion. The 50-fiber H_2-

permeable PBMR with the same catalyst mass (0.6 g) showed predicted conversion ~ 40% under the same operation conditions. The results indicated that CMR can provide higher conversion enhancements than H_2-permeable PBMR. Notably, a large number of fibers is required in the CMR modeling to achieve attractive conversion because of the small amount of catalyst impregnated into a single fiber within the heating zone (12 mg catalyst/CMS fiber, 50 wt% catalyst loading).

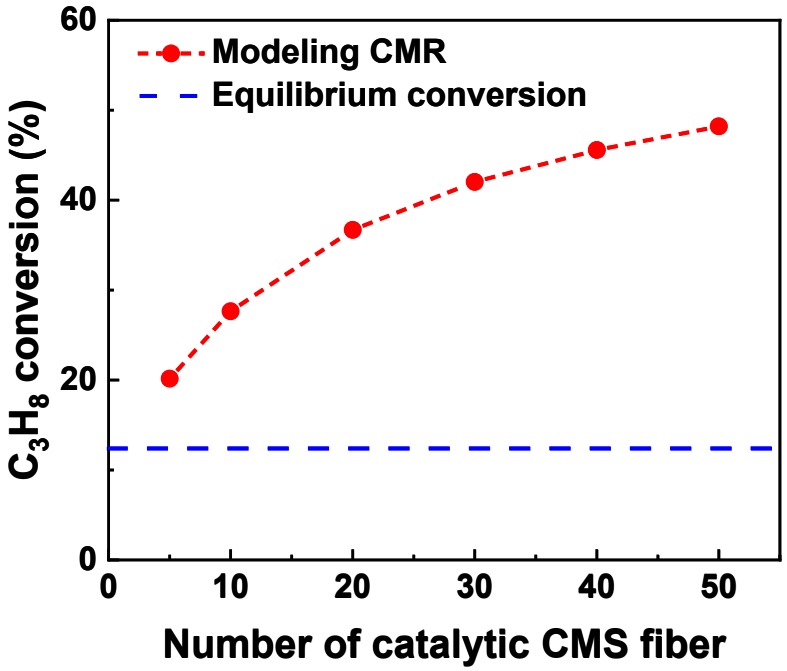

Figure 6.16. The role of number of catalytic CMS fibers on PDH conversion in CMR. The equilibrium line was drawn to show conversion enhancement in CMR. Modeling conditions: feed 1.73 h^{-1} (50%C_3H_8/50%Ar), reaction temperature 450 °C, sweep 100 mL/min Ar, gas permeances at 450 °C were taken from **Table 6.3**.

6.5.3 Effects of membrane permeance

The impact of membrane H_2 permeance on CMR performance was simulated in the range of 234-11700 GPU (**Figure 6.17**). The simulating H_2 permeance range assumed the membrane separation layer thickness decreased from 5 μm to 100 nm with constant $H_2/C_3H_6/C_3H_8$ selectivity as provided in **Table 3**. With increasing H_2

permeance from 234 to 2950 GPU (i.e., membrane separation layer thickness decreases from 5 μm to 400 nm), C_3H_8 conversion in the CMR increased due to the enhanced gas removal rates. However, further increase of membrane gas permeance (i.e., membrane separation layer thickness decreases from 400 nm to 100 nm) showed decreased C_3H_8 conversion in CMR. When the effect of reactant loss (i.e., high C_3H_8 permeance) is larger than the effect of product removal (high H_2 and C_3H_6 permeance), the C_3H_8 conversion would decrease. This could explain the CMR with skin layer less than 400 nm showed lower conversion in the modeling data. The potential solution is to increase the catalytic CMS membrane H_2/C_3H_8 selectivity to reduce the reactant loss as well as raise the catalyst loading to keep a high reaction rate. Indeed, when the H_2/C_3H_8 selectivity increases from 221 to 500 and the catalyst loading increases from 50 wt% to 70 wt%, the predicted C_3H_8 conversion in the CMR increased from 30% to 55% with the H_2 permeance of 11700 GPU. The modeling results suggest that membrane H_2/C_3H_8 selectivity and catalyst mass need to be adjusted in parallel with ultrathin membrane separation layer thickness to achieve attractive PDH performance in CMR.

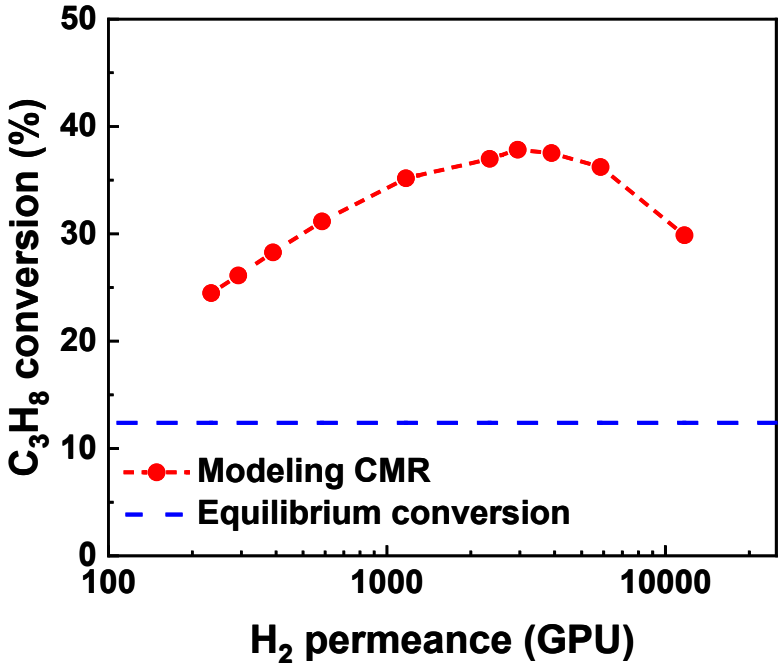

Figure 6.17. The impact of H_2 permeance on PDH conversion in CMR. The equilibrium line was drawn to show conversion enhancement in CMR. Modeling conditions: feed 1.73 h^{-1} (50%C_3H_8/50%Ar), reaction temperature 450 ºC, sweep 1 L/min Ar, 10 catalytic CMS fiber with catalyst loading of 50 wt%.

6.6 Summary and conclusions

A one-dimensional (1D) isothermal model was developed by material balance to predict PDH performance of CMS hollow fiber membrane reactors. Pt-Zn/S1 catalyst reaction rate equation for PDH was derived and the values of kinetic parameters were provided by kinetic rate measurements of the catalyst. CMS hollow fiber membrane $H_2/C_3H_6/C_3H_8$ separation performance was measured at 350-500 ºC. Applying the reaction kinetics and gas permeances, we predicted PDH conversions using the 1D isothermal model in three types of membrane reactors, i.e., H_2-permeable PBMR, C_3H_6-permeable PBMR, and catalytic membrane reactor (CMR). In the modeling of H_2-permeable PBMR, the effects of operating conditions and membrane properties on PDH conversions were investigated including reaction temperature,

WHSV, sweep flow rate, C_3H_8 feed partial pressure, feed total pressure, membrane separation area, gas permeance, and membrane H_2/C_3H_8 selectivity. The modeling and experimental PBMR results showed overall good agreement. This 1D isothermal model was also used to predict PBMR performance beyond the experimental conditions to provide insight for achieving further enhanced PDH performance.

We also used the 1D isothermal model to demonstrate the viability of C_3H_6-permeable PBMR, which is believed to have enhanced stability by being more resistant to catalyst deactivation. The model shows that C_3H_6-permeable PBMR can be enabled by restricting H_2 permeation via controlling sweep H_2 concentration. While attractive C_3H_8 conversion enhancement can be obtained, there is a trade-off between conversion enhancement and membrane reactor stability. Finally, the 1D isothermal PBMR model was revised to simulate CMR, in which the roles of catalyst loading, the number of catalytic fibers, and membrane permeance were investigated. The modeling results showed that the CMR can provide competitive C_3H_8 conversion enhancement with the H_2-permeable PBMR. It should be noted that the C_3H_6-permeable PBMR and CMR were not fabricated and thus a comparison of the model with experimental results was not made. This fact notwithstanding, the modeling results of these two novel reactors provide valuable insights on future development of CMS hollow fiber membrane reactors for PDH.

Chapter 7: Conclusions and recommendations

7.1 Summary and conclusions

The overarching goal of this work is to develop low-temperature and stable propane dehydrogenation (PDH) in packed bed membrane reactors (PBMR) comprising asymmetric CMS hollow fine fiber membranes. The objectives described in Chapter 1 are reviewed and the conclusions of each objective are summarized below.

Research objective 1: Investigate high-temperature H_2/C_3H_8 separation in asymmetric CMS hollow fiber membranes (Chapter 4).

The high-temperature H_2/C_3H_8 separation performance (up to 600 ^oC) of asymmetric CMS hollow fiber membranes was systematically investigated for the first time. As the CMS hollow fiber membrane pyrolysis temperature increased, the average H_2 permeance decreased with increasing average H_2/C_3H_8 separation factors. With increasing permeation temperature, CMS hollow fiber membrane showed increased gas permeances with decreased H_2/C_3H_8 separation factors. The positive H_2 and C_3H_8 apparent permeation activation energies suggested that high-temperature H_2/C_3H_8 permeation in CMS membranes is dominated by diffusion. It was found that CMS membrane pore structure and separation performance may be modulated by hydrogenation and pyrocarbon deposition by the H_2/C_3H_8 mixture under high-temperature permeation. A trade-off between these two potential reactions is achieved by controlling H_2/C_3H_8 compositions, leading to stable CMS under high-temperature conditions. CMS hollow fiber membranes showed outstanding stability under

continuous 130-hour permeation using H_2/C_3H_8 feed mixture at 600 ºC. Additionally, CMS hollow fiber membrane was tested using $H_2/C_3H_6/C_3H_8$ feed mixture to evaluate membrane separation performance under PDH conditions. With increasing permeation temperature, the CMS membrane showed almost constant H_2 permeance and improved separation factors. Overall, the results suggested that asymmetric CMS hollow fiber membranes can provide attractive high-temperature H_2/C_3H_8 separation performance and are promising for PDH membrane reactor applications.

Research objective 2: Investigate low-temperature and stable propane dehydrogenation in H_2-permeable CMS hollow fiber membrane reactors (Chapter 5).

For the first time, the CMS membrane reactors were developed for PDH, which integrates scalable H_2-permeable asymmetric CMS hollow fine fiber membranes and platinum-zinc/silicalite-1 (Pt-Zn/S1) catalysts. With 19 CMS fibers incorporated into the reactor, the C_3H_8 conversion was enhanced almost 4 times as high as equilibrium conversion, showing the great benefits of CMS hollow fiber membranes for PDH reactor conversion improvements. The roles of operating conditions on CMS membrane reactor performance were systematically investigated. With increasing of reaction temperature, the C_3H_8 conversion increased with slightly dropped C_3H_6 selectivity in CMS membrane reactor. By reducing the feed space velocity, the C_3H_8 conversion increased with constantly high C_3H_6 selectivity in the CMS membrane reactor. By reducing the feed C_3H_8 partial pressure, the CMS membrane reactor showed increased C_3H_8 conversion with almost constant C_3H_6 selectivity. The C_3H_8 conversion in the CMS membrane reactor increased very slightly with increasing sweep flow rate.

The CMS membrane reactor showed outstanding stability under continuous 112-hour reaction. The regeneration of spent Pt-Zn/S1 catalyst under H_2 flow was able to recover the catalyst activity by removing the coke deposition. The CMS hollow fiber membrane reactor developed in this work exceled literature reported PDH membrane reactors by operating at relatively low temperature, providing high conversion enhancements, and showing the lowest deactivation rate. These findings demonstrated the competitiveness of low temperature and stable H_2-permeable CMS hollow fiber membrane reactors for PDH, which paves the way for sustainable on-purpose C_3H_6 production.

Research objective 3: Modeling of CMS hollow fiber membrane reactors model for propane dehydrogenation (Chapter 6).

1D isothermal models were developed to predict PDH performance of three types of CMS hollow fiber membrane reactors, i.e., H_2-permeable PBMR, C_3H_6-permeable PBMR, and catalytic membrane reactor (CMR). The modeling of H_2-permeable PBMR showed good agreements with the experimental data obtained in Chapter 5. This model also predicted H_2-permeable PBMR performance under different membrane separation properties and various reaction pressures. The 1D isothermal model also demonstrated the viability of C_3H_6-permeable membrane reactor by restricting H_2 permeation via adding H_2 in sweep. With increasing H_2 concentration in the sweep, the H_2 partial pressure in the reaction side increased with decreased C_3H_6 partial pressure. Although the conversion enhancement decreased with H_2 flow in sweep, the C_3H_6-permeable membrane reactor could benefit from improved stability due to the reduced catalyst coking rate. The model indicated thinner membrane separation layer and moderate-to-high C_3H_6/C_3H_8 separation factor were favored to

improve the conversion of C_3H_6-permeable membrane reactor. The 1D isothermal PBMR model was revised to predict PDH performance in catalytic CMS hollow fiber membrane reactors. The modeling results demonstrated the importance of keeping high PDH reaction rate by having high catalyst loading concentration and larger number of catalytic fibers in the reactor. A thinner membrane separation layer was also preferred for higher conversion enhancements in catalytic membrane reactors. The modeling work provided guidelines for developing high performance PDH membrane reactors in terms of membrane properties and operation conditions.

7.2 Recommendations

Three research objectives of the PDH membrane reactor project were successfully achieved. This final section outlines recommendations for future work in this research area.

7.2.1 Fabricating ultra-thin CMS hollow fiber membranes for H_2-permeable PDH membrane reactors

Former studies showed that ultra-thin CMS hollow fiber membranes had attractive CO_2/CH_4 separation factors ~30 and outstanding CO_2 permeances up to ~2500 GPU.[91] Compared with traditional asymmetric CMS hollow fiber membranes with thicker separation layer (3-6 μm), the ultra-thin CMS hollow fiber membranes could provide ~ 1400% higher CO_2 permeance. Higher gas permeance is essential for achieving larger conversion enhancements in the PDH membrane reactor as suggested by the modeling results in Chapter 6 Section 6.3.1.7. The application of ultra-thin CMS

hollow fiber membranes in PDH membrane reactors is expected to provide more attractive C_3H_8 conversion enhancements.

The dual-layer polymer precursor hollow fibers can be fabricated using dry-jet/wet-quench spinning (**Figure 7.1**).[91] The precursor hollow fibers are formed by co-extruding two polymer solutions (sheath polymer solution and core polymer solution) from a multi-channel spinneret followed by phase separation in a water bath. By adjusting the sheath flow rate during hollow fiber spinning, the skin layer thickness of precursor fiber can be manipulated. It's critical that the ultrathin CMS hollow fibers consist of defect-free separation layers and porous substrates so that they can successfully provide attractive membrane selectivities as well as high gas permeances. The membrane reactor can be constructed using ultrathin CMS hollow fine fibers and PDH catalysts. The reaction tests need to be conducted to investigate the ultrathin CMS hollow membrane reactor performance under various operating conditions.

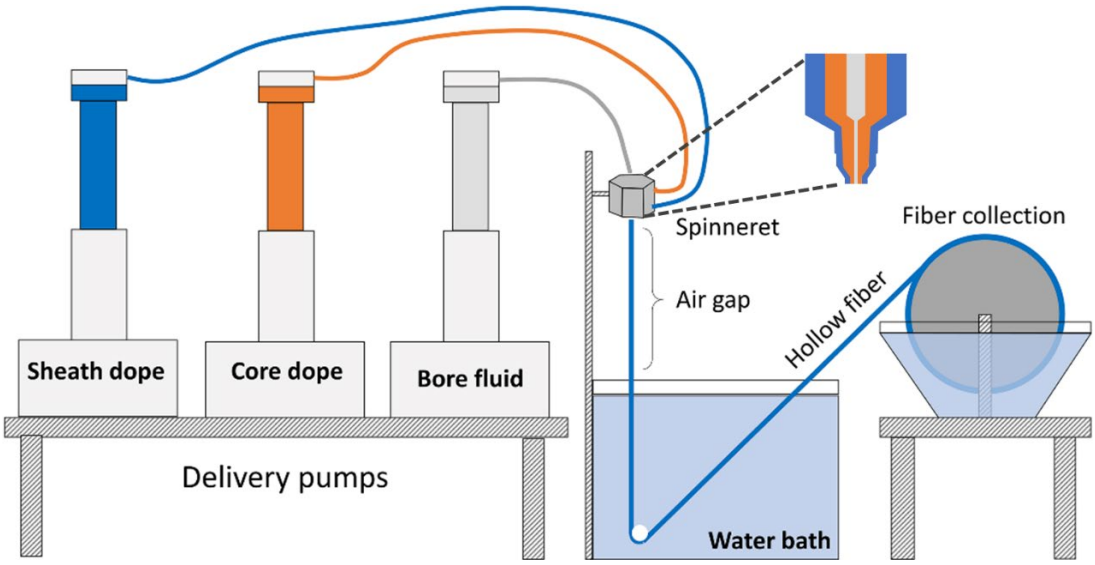

Figure 7.1. Fabrication of dual-layer precursor hollow fibers using dry-jet/wet-quench process.[91]

7.2.2 Investigating C_3H_6-permeable membrane reactor for PDH process

C_3H_8 conversion enhancements have been achieved in H_2-permeable PDH membrane reactors made of alumina, silica, zeolite, or Pd-based membranes in combination with commercial Cr_2O_3 or Pt-based catalysts. However, both catalyst and membrane suffer from accelerated coking and deactivation due to H_2 depletion. In contrast to H_2 removal, C_3H_6-permeable membrane reactors focus on removing C_3H_6 to shift the reaction equilibrium. Since C_3H_6 is known as coke precursor due to its high reactivity, the removal of C_3H_6 while maintaining H_2 in the reaction side could improve the durability of PDH membrane reactors.

The modeling results in Chapter 6 Section 6.4 demonstrated the viability of C_3H_6-permeable membrane reactors by restricting H_2 permeation via mixing H_2 in sweep. The CMS hollow fiber membranes with attractive C_3H_6/C_3H_8 selectivities at temperature 450 ^oC or higher need to be developed. Polyamides can be selected as precursor materials to provide high-rigidity and desirable C_3H_6/C_3H_8 membrane selectivity under PDH reaction conditions. The C_3H_6-selective CMS hollow fiber membranes with thin separation layers also need to be fabricated to allow high C_3H_6 permeance. Since the size-selective CMS membrane allows H_2 removal in addition to C_3H_6 permeation, adding H_2 in sweep is necessary to minimize the H_2 permeation from feed to sweep side. The effects of H_2 concentration in the sweep on the C_3H_6-permeable membrane reactor performance need to be investigated. The long-term stability of C_3H_6-permeable CMS hollow fiber membrane reactor for PDH needs to be evaluated.

7.2.3 Exploring catalytic CMS hollow fiber membrane reactor for PDH reaction

Highly compact catalytic membrane reactors can be developed by depositing catalyst particles into CMS hollow fiber membrane porous substructure, allowing simultaneous PDH reaction and product separation within CMS membrane. Previous work reported silica-loaded CMS hollow fiber membranes[90], where the hollow fiber membranes comprised an outside dense selective separation layer and a highly porous substrate with dispersed silica nanoparticles. The silica-loaded CMS hollow fiber membranes were studied for CO_2/CH_4 separation showing excellent separation factors. Remarkably, the silica-loaded CMS hollow fiber membranes had good mechanical flexibility with high loading of silica nanoparticles in the highly porous substrate and were stable in H_2 atmosphere at high temperatures. These results provided strong evidence that high-catalyst-loading catalytic CMS hollow fiber membrane reactors can be made with desirable separation performance and good mechanical/chemical properties.

The silica particles can be replaced by Pt-Zn/silicalite-1 catalysts on developing catalytic CMS membrane reactors. Dual-layer catalytic polymer precursor hollow fibers need to be fabricated, where the sheath dope is free of catalyst particles and the core dope comprises Pt-Zn/silicalite-1 catalysts. The sheath flow rate can be controlled to provide ultrathin catalytic CMS hollow fiber membranes, allowing high gas permeation rates during reaction. The reaction performance of catalytic CMS hollow fiber membranes needs to be investigated under various operating conditions. The long-term stability of catalytic CMS hollow fiber membrane reactor for PDH needs to be evaluated.

Appendix A: Summary of PDH membrane reactors

Membrane material (geometry)	Catalyst	Feed (vol%)	T (°C)	Equil. Conv. (%)	C_3H_8 Conv. (%)	C_3H_6 Sel. (%)	C_3H_6 Yield (%)	Conv./ Equil. Conv.	TOS (h)	Ref.
CMS (hollow fiber)	Pt-Zn/S1	50%C_3H_8/ 50%Ar	450	12.4	36.6	95.3	34.9	2.95	112.5	This work
Pd-Ag/vycor glass (tubular)	Pt/Al_2O_3	50%C_3H_8/ 50%N_2	400	5.3	21.0	-	-	4.00	-	[60]
Pd/Al_2O_3 (tubular)	Pt/Al_2O_3	50%C_3H_8/ 50%N_2	570	40.0	47.0	-	-	1.18	-	[60]
Pd-silica/ Al_2O_3 (tubular)	Pt/Al_2O_3	50%C_3H_8/ 50%N_2	437 - 463	-	11.0-19.0	-	-	-	-	[60]
Pd-Ag/Al_2O_3 (tubular)	Pt/Al_2O_3	50%C_3H_8/ 50%N_2	437 - 468	-	12.0-27.5	>97.0	17.9-39.8	-	-	[60]
Pd-Ag/ Al_2O_3 (tubular)	Cr_2O_3/ Al_2O_3	100% C_3H_8	500	18.0	-	85.0-95.0	36.0	2.10-2.35	7.0	[40]
Pd/Al_2O_3 (tubular)	-	C_3H_8, H_2, N_2 mixture	560	30.2	35.4	-	26.1	1.17	1.0-2.0	[187]
Pd stainless steel (tubular)	-	C_3H_8, H_2, N_2 mixture	560	30.2	42.0	-	-	1.39	1.0-2.0	[187]
Pd-Ag alloy (tubular)	Pt-Sn/ Al_2O_3/ silica	100% C_3H_8	550	24.0	34.0	79.0	26.9	1.42	1.7	[188]
Pd-Ag alloy (tubular)	Pt-Sn/ Al_2O_3/ silica	100% C_3H_8	550	23.0	30.0	94.0	10.2	1.30	16.7	[189]
Pd/Al_2O_3 (tubular)	Pt-K-Sn/ Al_2O_3	20%C_3H_8/ 80%N_2	350 - 550	3.6-34.2	11.0-72.0	94.5-72.0	10.4-52.8	2.10-3.06	-	[190]
Pd-Ag/Al_2O_3 (hollow fiber)	Pt/Al_2O_3	5%C_3H_8/ 4.5%H_2/ 90.5%N_2	450	22.0	42.1	-	-	1.91	0.8	[15]
Pd/Al_2O_3 (hollow fiber)	Pt/ SBA-15	5%C_3H_8/ 4.5%H_2/ 90.5%N_2	500	-	48.7	18.0	8.8	-	2.0	[36]
Pd-Ag foil (disk)	Cr_2O_3/ Al_2O_3	100% C_3H_8	520	-	35.0	-	-	-	2.0	[191]
Pd/Al_2O_3 (hollow fiber)	Pt-Sn/ $MgAl_2O_4$	100% C_3H_8	500	30.2	17.7	90.3	16.0	0.59	1.7	[176]
Pd-Ag/ stainless steel (tubular)	Pt-Sn/ $MgAl_2O_4$	50%C_3H_8/ 50%Ar	575	49.7	33.0	78.0	25.5	0.66	2.0	[192]
Pd-Ag alloy (tubular)	Supported Pt	100% C_3H_8	525	24.0	-	-	40.0	-	2.0	[17]

(Continued)

Membrane material (geometry)	Catalyst	Feed (vol%)	T (°C)	Equil. Conv. (%)	C_3H_8 Conv. (%)	C_3H_6 Sel. (%)	C_3H_6 Yield (%)	Conv./ Equil. Conv.	TOS (h)	Ref.
SAPO-34/ Al_2O_3 (tubular)	Na_2O-Cr_2O_3/ Al_2O_3	100% C_3H_8	600	48.0	75.0	77.0	58.0	1.56	16.0	[19]
LTA-coated Pd/Al_2O_3 (hollow fiber)	Cr/Al_2O_3	30%C_3H_8/ 70%N_2	600	66.6	47.0	93.0	43.7	0.71	0.3	[14]
Hybrid MFI-Pt/ Al_2O_3 (disk)	Pt cluster	100% C_3H_8	600	48.0	23.0	32.5	7.2	0.48	5.0	[20]
Silicate/ Al_2O_3 (disk)	Pt/Al_2O_3	100% C_3H_8	600, 5 atm	23.0	49.0	97.0	47.0	2.13	12.0	[30]
Silica/ Al_2O_3 (tubular)	Pt/ aluminosilicate	100% C_3H_8	550	32.0	40.8	>97.0	39.6	1.27	-	[21]
Silica/ Al_2O_3 (tubular)	Cr_2O_3/ Al_2O_3	100% C_3H_8	500	18.0	23.8	89.0	21.2	1.32	8.0	[28]
Silica/ Al_2O_3 (tubular)	Cr_2O_3/ Al_2O_3	100% C_3H_8	535	27.1	32.0-34.0	85.0-90.0	27.2-30.6	1.22	10.0	[193]
Silica/ Al_2O_3 (tubular)	Cr_2O_3/ Al_2O_3	33.3%C_3H_8/ 66.7%N_2	535	40.0	49.0	75.0	36.8	1.23	5.8	[27]
Silica/ Al_2O_3 (tubular)	Pt-Sn/ Al_2O_3	60%C_3H_8/ 40%N_2	500	22.0	27.5	80.0	22.0	1.25	4.2	[27]
Silica/ Al_2O_3 (tubular)	Pt/Al_2O_3	100% C_3H_8	600	48.0	53.0	68.5	40.8	1.10	4.2	[26]
Al_2O_3 (tubular)	Cr_2O_3/ Al_2O_3	100% C_3H_8	575	-	58.7	90.0	52.8	1.45	2.0	[18]
Al_2O_3 (tubular)	Pt-Mg/ Al_2O_3	66.6%C_3H_8/ 16.7%C_3H_6/ 16.7%H_2	520 - 600	1.8-34.0	3.5-70.0	95.0-73.0	3.5-52.2	1.94-2.06	-	[23]
Al_2O_3 (tubular)	Pt-Mg/ Al_2O_3	80%C_3H_8/ 20%N_2	480 - 625	8.0-78.0	10.0-90.0	99.0-68.0	9.9-61.2	1.15-1.25	-	[22]
Mo/Al_2O_3 (tubular)	Mo	80%C_3H_8/ 20%N_2	600	45.0	28.0	62.0	17.4	0.62	-	[194]
Mo/carbon (tubular)	Mo	80%C_3H_8/ 20%N_2	600	45.0	40.0	74.0	29.6	0.89	-	[194]
Ni/Al_2O_3 (tubular)	Pt/Al_2O_3	20%C_3H_8/ 20%H_2/ 60%N_2	500	-	40.8	63.7	26.0	-	1.0	[195]

Appendix B: GC sample data for permeation and reaction tests

High-temperature $H_2/C_3H_6/C_3H_8$ permeation

Testing conditions:

- Feed: 5%H_2/5%C_3H_6/40%C_3H_8/50%Ar, total flow rate 20 mL/min
- Sweep: 20 mL/min Ar
- Temperature: 450 ºC
- Membrane module: 1-fiber CMS membrane module (550 ºC pyrolysis)

Table B.1. GC peak area in membrane module permeate side.

Time/min	H_2 peak area	Ar peak area	C_3H_8 peak area	C_3H_6 peak area
0	285.9	7492	223.1	262.6
22	284.1	7493.1	220.4	261.2
44	291.4	7489.4	223.5	258.2
66	294.4	7489.6	222	247.8
88	294.9	7490.7	220.2	246
110	293.9	7486.9	216.4	244
132	293.1	7479.9	212	241.3
154	292.6	7481.7	208.9	239.9
176	291.5	7478	206	239.1
198	290.8	7481.1	202.3	237.9
220	287.4	7479.4	199.1	233.4
242	286.9	7481.8	196.9	231.2
308	284.6	7485.7	185.8	224.1
374	281.1	7490.2	176.6	217.7
440	276.1	7492.6	168.9	211.5
506	273.9	7492.3	162.7	208.3

Table B.2. Gas volume percentage in membrane module permeate side.

Time/min	H_2 (vol%)	Ar (vol%)	C_3H_8 (vol%)	C_3H_6 (vol%)
0	0.5079	0.02866	0.03399	99.4295
22	0.5047	0.02832	0.03381	99.4332
44	0.5176	0.02872	0.03342	99.4202
66	0.5230	0.02852	0.03208	99.4164
88	0.5238	0.02829	0.03184	99.4160
110	0.5221	0.02780	0.03158	99.4185
132	0.5206	0.02724	0.03123	99.4209
154	0.5198	0.02684	0.03105	99.4223
176	0.5178	0.02647	0.03095	99.4248
198	0.5166	0.02599	0.03079	99.4267
220	0.5105	0.02558	0.03021	99.4337
242	0.5096	0.02530	0.02993	99.4351
308	0.5056	0.02387	0.02901	99.4416
374	0.4993	0.02269	0.02818	99.4498
440	0.4905	0.02170	0.02738	99.4605
506	0.4865	0.02090	0.02696	99.4656

PDH membrane reactor

Testing conditions:

- Feed: 50%C_3H_8/50%Ar, total flow rate 5 mL/min
- Sweep: 50 mL/min Ar
- Temperature: 450 ^oC
- Membrane reactor: 5-fiber CMS membrane module + 0.3 g Pt-Zn/S1 catalyst

Table B.3. GC peak area in PDH membrane reactor (flame ionized detector).

Time/min	CH_4 peak area	C_2H_6 peak area	C_3H_8 peak area	C_3H_6 peak area
Retentate side				
0	532.4	1119.2	184414.9	39941
22	530.3	1112.9	184436.2	40218.7
44	538	1128.7	192585	41003.3
66	528.7	1111.5	191730.9	40750.2
88	521.3	1095.7	193154	41028.9
110	516.8	1086	194025	41044.4
132	517.2	1085.4	193665.3	41163.9
154	511.6	1074.3	179419.2	39338.1
176	517.9	1083.6	192559.2	41070.3
Permeate side				
198	4.7	2.7	375.4	113.7
220	4.6	2.5	366	111
242	4.4	2.7	364	110.5
308	4.5	2.5	359.2	108.6
374	4.6	2.6	356.7	107.2
440	4.5	2.6	354	106.5

Table B.4. Gas volume percentage[a] in PDH membrane reactor.

Time/min	CH_4 (vol%)	C_2H_6 (vol%)	C_3H_8 (vol%)	C_3H_6 (vol%)
Retentate side				
0	0.2307	0.2445	24.3911	5.5955
22	0.2297	0.2430	24.3939	5.6344
44	0.2331	0.2467	25.4636	5.7443
66	0.2290	0.2427	25.3514	5.7089
88	0.2258	0.2390	25.5383	5.7479
110	0.2238	0.2368	25.6526	5.7501
132	0.2240	0.2366	25.6054	5.7668
154	0.2215	0.2340	23.7353	5.5110
176	0.2243	0.2362	25.4602	5.7537
Permeate side[b]				
198	0	0	0.2319	0.0140
220	0	0	0.2307	0.0137
242	0	0	0.2304	0.0136
308	0	0	0.2298	0.0133
374	0	0	0.2295	0.0131
440	0	0	0.2291	0.0130

[a] balanced with Ar; b CH_4 and C_2H_6 volume percentage is below 0.01%.

Bibliography

1. Amghizar, I., et al., *New trends in olefin production.* Engineering, 2017. **3**(2): p. 171-178.
2. Maddah, H.A., *Polypropylene as a promising plastic: A review.* Am. J. Polym. Sci, 2016. **6**(1): p. 1-11.
3. Lavrenov, A., et al., *Propylene production technology: Today and tomorrow.* Catalysis in Industry, 2015. **7**: p. 175-187.
4. *Propylene Market*. 2023, Precedence Research.
5. *Market volume of polypropylene worldwide from 2015 to 2022, with a forecast for 2023 to 2030*. 2023, Statista Research Department.
6. Sumner, C., *Production of propylene from steam cracking of hydrocarbons, particularly ethane*. 2007, Google Patents.
7. Gholami, Z., et al., *A review on production of light olefins via fluid catalytic cracking.* Energies, 2021. **14**(4): p. 1089.
8. Marsh, M. and J. Wery, *Filling the Propylene Gap–Shaping the Future with On-Purpose Technologies.* Honeywell UOP, 2019.
9. Malakoff, D., *The gas surge*. 2014, American Association for the Advancement of Science. p. 1464-1467.
10. Stangland, E.E., *Shale gas implications for C2-C3 olefin production: incumbent and future technology.* Annual review of chemical and biomolecular engineering, 2018. **9**: p. 341-364.
11. Chen, S., et al., *Propane dehydrogenation: catalyst development, new chemistry, and emerging technologies.* Chemical SOCIETY reviews, 2021. **50**(5): p. 3315-3354.
12. Sattler, J.J., et al., *Catalytic dehydrogenation of light alkanes on metals and metal oxides.* Chemical reviews, 2014. **114**(20): p. 10613-10653.
13. Monai, M., et al., *Propane to olefins tandem catalysis: a selective route towards light olefins production.* Chemical Society Reviews, 2021. **50**(20): p. 11503-11529.
14. Pati, S., et al., *Nanoporous zeolite-A sheltered Pd-hollow fiber catalytic membrane reactor for propane dehydrogenation.* ACS Applied Nano Materials, 2020. **3**(7): p. 6675-6683.
15. Wu, Z., et al., *A novel inorganic hollow fiber membrane reactor for catalytic dehydrogenation of propane.* AIChE journal, 2009. **55**(9): p. 2389-2398.
16. Wang, Z., et al., *High H2 permeable SAPO‐34 hollow fiber membrane for high temperature propane dehydrogenation application.* AIChE Journal, 2020. **66**(9): p. e16278.
17. Sheintuch, M. and R.M. Dessau, *Observations, modeling and optimization of yield, selectivity and activity during dehydrogenation of isobutane and propane in a Pd membrane reactor.* Chemical Engineering Science, 1996. **51**(4): p. 535-547.
18. Bitter, J., *Process and apparatus for the dehydrogenation of organic compounds.* UK Patent Application, 1986(8629135).

19. Kim, S.-J., et al., *Thin hydrogen-selective SAPO-34 zeolite membranes for enhanced conversion and selectivity in propane dehydrogenation membrane reactors.* Chemistry of Materials, 2016. **28**(12): p. 4397-4402.
20. Kim, S.-J., et al., *One-step synthesis of zeolite membranes containing catalytic metal nanoclusters.* ACS Applied Materials & Interfaces, 2016. **8**(37): p. 24671-24681.
21. Collins, J.P., et al., *Catalytic dehydrogenation of propane in hydrogen permselective membrane reactors.* Industrial & engineering chemistry research, 1996. **35**(12): p. 4398-4405.
22. Ziaka, Z., R. Minet, and T. Tsotsis, *Propane dehydrogenation in a packed-bed membrane reactor.* AIChE Journal (American Institute of Chemical Engineers);(United States), 1993. **39**(3).
23. Ziaka, Z., R. Minet, and T. Tsotsis, *A high temperature catalytic membrane reactor for propane dehydrogenation.* Journal of membrane science, 1993. **77**(2-3): p. 221-232.
24. Hines, A.L. and R.N. Maddox, *Mass transfer: fundamentals and applications*. Vol. 434. 1985: Prentice-Hall Englewood Cliffs, NJ.
25. Collins, J.P., et al., *Catalytic dehydrogenation of propane and isobutane in hydrogen permselective membrane reactors*. 1996, Sandia National Lab.(SNL-NM), Albuquerque, NM (United States).
26. Ishii, K., et al., *Development of hydrogen permselective membranes for propylene production.* Journal of Chemical Engineering of Japan, 2021. **54**(5): p. 260-265.
27. Schäfer, R., et al., *Comparison of different catalysts in the membrane-supported dehydrogenation of propane.* Catalysis today, 2003. **82**(1-4): p. 15-23.
28. Weyten, H., et al., *Dehydrogenation of propane using a packed‐bed catalytic membrane reactor.* AIChE journal, 1997. **43**(7): p. 1819-1827.
29. Bui, V., et al., *Engineering silica membranes for separation performance, hydrothermal stability, and production scalability.* Advanced Membranes, 2023. **3**: p. 100064.
30. Dangwal, S., et al., *Propane Dehydrogenation Reaction in a High-Pressure Zeolite Membrane Reactor.* Energy & Fuels, 2021. **35**(23): p. 19362-19373.
31. http://www.iza-structure.org/databases/.
32. Caro, J., et al., *Zeolite membranes–state of their development and perspective.* Microporous and mesoporous materials, 2000. **38**(1): p. 3-24.
33. Varoon Agrawal, K., et al., *Dispersible exfoliated zeolite nanosheets and their application as a selective membrane.* Science, 2011. **334**(6052): p. 72-75.
34. Jeon, M.Y., et al., *Ultra-selective high-flux membranes from directly synthesized zeolite nanosheets.* Nature, 2017. **543**(7647): p. 690-694.
35. Yun, S. and S.T. Oyama, *Correlations in palladium membranes for hydrogen separation: A review.* Journal of membrane science, 2011. **375**(1-2): p. 28-45.
36. Gbenedio, E., et al., *A multifunctional Pd/alumina hollow fibre membrane reactor for propane dehydrogenation.* Catalysis Today, 2010. **156**(3-4): p. 93-99.

37. Dittmeyer, R., V. Höllein, and K. Daub, *Membrane reactors for hydrogenation and dehydrogenation processes based on supported palladium.* Journal of Molecular Catalysis A: Chemical, 2001. **173**(1-2): p. 135-184.
38. Didenko, L., et al., *Some peculiarities of dehydrogenation of propane and n-butane in a combined membrane reactor with the AOK-73-24 industrial alumina–chromia catalyst and a palladium membrane.* Petroleum Chemistry, 2016. **56**: p. 459-464.
39. Peters, T., et al., *Investigation of Pd-based membranes in propane dehydrogenation (PDH) processes.* Chemical Engineering Journal, 2016. **305**: p. 191-200.
40. Weyten, H., et al., *Membrane performance: the key issues for dehydrogenation reactions in a catalytic membrane reactor.* Catalysis today, 2000. **56**(1-3): p. 3-11.
41. Hurlbert, R. and J. Konecny, *Diffusion of hydrogen through palladium.* The Journal of Chemical Physics, 1961. **34**(2): p. 655-658.
42. Nakaya, Y. and S. Furukawa, *Tailoring Single‐Atom Platinum for Selective and Stable Catalysts in Propane Dehydrogenation.* ChemPlusChem, 2022. **87**(4): p. e202100560.
43. Zha, S., et al., *Identification of Pt-based catalysts for propane dehydrogenation via a probability analysis.* Chemical science, 2018. **9**(16): p. 3925-3931.
44. Zhao, Z.-J., C.-c. Chiu, and J. Gong, *Molecular understandings on the activation of light hydrocarbons over heterogeneous catalysts.* Chemical science, 2015. **6**(8): p. 4403-4425.
45. Kaylor, N. and R.J. Davis, *Propane dehydrogenation over supported Pt-Sn nanoparticles.* Journal of catalysis, 2018. **367**: p. 181-193.
46. Yang, M.-L., et al., *First-principles calculations of propane dehydrogenation over PtSn catalysts.* Acs Catalysis, 2012. **2**(6): p. 1247-1258.
47. Wang, H.-Z., et al., *Coke formation on Pt–Sn/Al2O3 catalyst for propane dehydrogenation.* Industrial & Engineering Chemistry Research, 2018. **57**(26): p. 8647-8654.
48. Deng, L., et al., *Elucidating strong metal-support interactions in Pt–Sn/SiO2 catalyst and its consequences for dehydrogenation of lower alkanes.* Journal of Catalysis, 2018. **365**: p. 277-291.
49. Sun, P., et al., *Novel Pt/Mg (In)(Al) O catalysts for ethane and propane dehydrogenation.* Journal of catalysis, 2011. **282**(1): p. 165-174.
50. Hill, J.M., R. Cortright, and J. Dumesic, *Silica-and L-zeolite-supported Pt, Pt/Sn and Pt/Sn/K catalysts for isobutane dehydrogenation.* Applied Catalysis A: General, 1998. **168**(1): p. 9-21.
51. Sun, X., et al., *Revealing nature of active site and reaction mechanism of supported chromium oxide catalyst in propane direct dehydrogenation.* Molecular Catalysis, 2021. **505**: p. 111520.
52. Sattler, J.J., A.M. Mens, and B.M. Weckhuysen, *Real‐Time Quantitative Operando Raman Spectroscopy of a CrOx/Al2O3 Propane Dehydrogenation Catalyst in a Pilot‐Scale Reactor.* ChemCatChem, 2014. **6**(11): p. 3139-3145.
53. Liu, G., et al., *Nature of the active sites of VOx/Al2O3 catalysts for propane dehydrogenation, ACS Catal, 6: 5207-5214*. 2016, DOI.

54. Sokolov, S., et al., *Effect of VOx species and support on coke formation and catalyst stability in nonoxidative propane dehydrogenation.* ChemCatChem, 2015. **7**(11): p. 1691-1700.
55. Zheng, B., et al., *Dehydrogenation of propane to propene over different polymorphs of gallium oxide.* Journal of Catalysis, 2005. **232**(1): p. 143-151.
56. Liu, Y., et al., *Periodic density functional theory study of propane dehydrogenation over perfect Ga2O3 (100) surface.* The Journal of Physical Chemistry C, 2008. **112**(51): p. 20382-20392.
57. Pidko, E.A. and R.A. van Santen, *Structure− reactivity relationship for catalytic activity of gallium oxide and sulfide clusters in zeolite.* The Journal of Physical Chemistry C, 2009. **113**(11): p. 4246-4249.
58. Kosinov, N., et al., *Recent developments in zeolite membranes for gas separation.* Journal of Membrane Science, 2016. **499**: p. 65-79.
59. Tomita, T., K. Nakayama, and H. Sakai, *Gas separation characteristics of DDR type zeolite membrane.* Microporous and Mesoporous Materials, 2004. **68**(1-3): p. 71-75.
60. Yildirim, Y., E. Gobina, and R. Hughes, *An experimental evaluation of high-temperature composite membrane systems for propane dehydrogenation.* Journal of membrane science, 1997. **135**(1): p. 107-115.
61. Ning, X. and W.J. Koros, *Carbon molecular sieve membranes derived from Matrimid® polyimide for nitrogen/methane separation.* Carbon, 2014. **66**: p. 511-522.
62. Rungta, M., et al., *Carbon molecular sieve structure development and membrane performance relationships.* Carbon, 2017. **115**: p. 237-248.
63. Ngamou, P.T., et al., *High-performance carbon molecular sieve membranes for hydrogen purification and pervaporation dehydration of organic solvents.* Journal of Materials Chemistry A, 2019. **7**(12): p. 7082-7091.
64. Fu, S.L., et al., *Carbon molecular sieve membrane structure-property relationships for four novel 6FDA based polyimide precursors.* Journal of Membrane Science, 2015. **487**: p. 60-73.
65. Zhang, C., et al., *Purification of aggressive supercritical natural gas using carbon molecular sieve hollow fiber membranes.* Industrial & Engineering Chemistry Research, 2017. **56**(37): p. 10482-10490.
66. Ma, Y., et al., *Creation of well‐defined "mid‐sized" micropores in carbon molecular sieve membranes.* Angewandte Chemie, 2019. **131**(38): p. 13393-13399.
67. Ma, X., et al., *Ultrathin carbon molecular sieve membrane for propylene/propane separation.* AIChE Journal, 2016. **62**(2): p. 491-499.
68. Koh, D.-Y., et al., *Reverse osmosis molecular differentiation of organic liquids using carbon molecular sieve membranes.* Science, 2016. **353**(6301): p. 804-807.
69. Tin, P.S., et al., *Separation of CO2/CH4 through carbon molecular sieve membranes derived from P84 polyimide.* Carbon, 2004. **42**(15): p. 3123-3131.
70. Liu, S., et al., *Carbon molecular sieve membranes derived from hydrogen-bonded organic frameworks for CO2/CH4 separation.* Journal of Membrane Science, 2023. **678**: p. 121674.

71. Zhang, C. and W.J. Koros, *Ultraselective carbon molecular sieve membranes with tailored synergistic sorption selective properties.* Advanced Materials, 2017. **29**(33): p. 1701631.
72. Rungta, M., L. Xu, and W.J. Koros, *Carbon molecular sieve dense film membranes derived from Matrimid® for ethylene/ethane separation.* Carbon, 2012. **50**(4): p. 1488-1502.
73. Kim, S.-J., et al., *A review on polymer precursors of carbon molecular sieve membranes for olefin/paraffin separation.* Membranes, 2021. **11**(7): p. 482.
74. Xu, L., *Carbon molecular sieve hollow fiber membranes for olefin/paraffin separations.* 2013.
75. Du, S., et al., *Probing sub-5 Ångstrom micropores in carbon for precise light olefin/paraffin separation.* Nature Communications, 2023. **14**(1): p. 1197.
76. Hazazi, K., et al., *Precise molecular sieving of ethylene from ethane using triptycene-derived submicroporous carbon membranes.* Nature Materials, 2023: p. 1-9.
77. Iyer, G.M. and C. Zhang, *Precise hydrogen sieving by carbon molecular sieve membranes derived from solution-processable aromatic polyamides.* ACS Materials Letters, 2022. **5**(1): p. 243-248.
78. Hu, L., et al., *Tailoring sub-3.3 Å ultramicropores in advanced carbon molecular sieve membranes for blue hydrogen production.* Science Advances, 2022. **8**(10): p. eabl8160.
79. Touma, S.L., et al. *Innovative Gas Treatment Solutions for Offshore Systems*. in *Offshore Technology Conference Brasil*. 2019.
80. Xu, L., M. Rungta, and W.J. Koros, *Matrimid® derived carbon molecular sieve hollow fiber membranes for ethylene/ethane separation.* Journal of membrane science, 2011. **380**(1-2): p. 138-147.
81. Sznejer, G.A., I. Efremenko, and M. Sheintuch, *Carbon membranes for high temperature gas separations: Experiment and theory.* AIChE Journal, 2004. **50**(3): p. 596-610.
82. Itoh, N. and K. Haraya, *A carbon membrane reactor.* Catalysis today, 2000. **56**(1-3): p. 103-111.
83. Sznejer, G. and M. Sheintuch, *Application of a carbon membrane reactor for dehydrogenation reactions.* Chemical Engineering Science, 2004. **59**(10): p. 2013-2021.
84. Hirota, Y., et al., *Pore size control of microporous carbon membranes by post-synthesis activation and their use in a membrane reactor for dehydrogenation of methylcyclohexane.* Journal of membrane science, 2013. **440**: p. 134-139.
85. Abdollahi, M., et al., *Hydrogen production from coal-derived syngas using a catalytic membrane reactor based process.* Journal of Membrane Science, 2010. **363**(1-2): p. 160-169.
86. Harale, A., et al., *Experimental studies of a hybrid adsorbent-membrane reactor (HAMR) system for hydrogen production.* Chemical engineering science, 2007. **62**(15): p. 4126-4137.
87. Sá, S., J.M. Sousa, and A. Mendes, *Steam reforming of methanol over a CuO/ZnO/Al2O3 catalyst part II: A carbon membrane reactor.* Chemical engineering science, 2011. **66**(22): p. 5523-5530.

88. Zhang, X., et al., *Methanol steam reforming to hydrogen in a carbon membrane reactor system.* Industrial & engineering chemistry research, 2006. **45**(24): p. 7997-8001.
89. Bhuwania, N., et al., *Engineering substructure morphology of asymmetric carbon molecular sieve hollow fiber membranes.* Carbon, 2014. **76**: p. 417-434.
90. Zhang, C., et al., *Composite carbon molecular sieve hollow fiber membranes: resisting support densification via silica particle stabilization.* Industrial & Engineering Chemistry Research, 2018. **57**(47): p. 16051-16058.
91. Zhang, C., R. Kumar, and W.J. Koros, *Ultra‐thin skin carbon hollow fiber membranes for sustainable molecular separations.* AIChE Journal, 2019. **65**(8): p. e16611.
92. Koros, W.J. and R.P. Lively, *Water and beyond: Expanding the spectrum of large‐scale energy efficient separation processes.* AIChE journal, 2012. **58**(9): p. 2624-2633.
93. Koros, W.J. and C. Zhang, *Materials for next-generation molecularly selective synthetic membranes.* Nature materials, 2017. **16**(3): p. 289-297.
94. Suda, H. and K. Haraya, *Gas permeation through micropores of carbon molecular sieve membranes derived from Kapton polyimide.* The Journal of Physical Chemistry B, 1997. **101**(20): p. 3988-3994.
95. Vu, D.Q., W.J. Koros, and S.J. Miller, *High pressure CO2/CH4 separation using carbon molecular sieve hollow fiber membranes.* Industrial & engineering chemistry research, 2002. **41**(3): p. 367-380.
96. Jenkins, G.M. and K. Kawamura, *Polymeric carbons: carbon fibre, glass and char*. 1976: Cambridge University Press.
97. Pierson, H.O., *Handbook of carbon, graphite, diamonds and fullerenes: processing, properties and applications*. 2012: William Andrew.
98. Steel, K.M. and W.J. Koros, *Investigation of porosity of carbon materials and related effects on gas separation properties.* Carbon, 2003. **41**(2): p. 253-266.
99. Xiao, Y., et al., *Structure and properties relationships for aromatic polyimides and their derived carbon membranes: experimental and simulation approaches.* The Journal of Physical Chemistry B, 2005. **109**(40): p. 18741-18748.
100. Fu, S., et al., *Carbon molecular sieve membrane structure–property relationships for four novel 6FDA based polyimide precursors.* Journal of Membrane Science, 2015. **487**: p. 60-73.
101. Ngamou, P.T., M. Ivanova, and O. Guillon, *High-performance carbon molecular sieve membranes for hydrogen purification and pervaporation dehydration of organic solvents.* Journal of Materials Chemistry A, 2019. **7**(12): p. 7082-7091.
102. Ma, X., et al., *Ultrathin carbon molecular sieve membrane for propylene/propane separation.* AIChE Journal, 2016. **62**(2): p. 491-499.
103. Ma, Y., et al., *Creation of well‐defined "mid‐sized" micropores in carbon molecular sieve membranes.* Angewandte Chemie International Edition, 2019. **58**(38): p. 13259-13265.
104. Bhuwania, N., *Engineering the morphology of carbon molecular sieve (CMS) hollow fiber membranes.* 2013.

105. Saufi, S. and A. Ismail, *Fabrication of carbon membranes for gas separation––a review.* Carbon, 2004. **42**(2): p. 241-259.
106. Edwards, I.A., H. Marsh, and R. Menendez, *Introduction to carbon science*. 2013: Butterworth-Heinemann.
107. Ehlers, G., K. Fisch, and W. Powell, *Thermal degradation of polymers with phenylene units in the chain. IV. Aromatic polyamides and polyimides.* Journal of Polymer Science Part A‐1: Polymer Chemistry, 1970. **8**(12): p. 3511-3527.
108. Hatori, H., et al., *The mechanism of polyimide pyrolysis in the early stage.* Carbon, 1996. **34**(2): p. 201-208.
109. Ismail, A.F. and L. David, *A review on the latest development of carbon membranes for gas separation.* Journal of membrane science, 2001. **193**(1): p. 1-18.
110. Fuertes, A., D. Nevskaia, and T. Centeno, *Carbon composite membranes from Matrimid® and Kapton® polyimides for gas separation.* Microporous and Mesoporous materials, 1999. **33**(1-3): p. 115-125.
111. David, L. and A. Ismail, *Influence of the thermastabilization process and soak time during pyrolysis process on the polyacrylonitrile carbon membranes for O2/N2 separation.* Journal of membrane science, 2003. **213**(1-2): p. 285-291.
112. Centeno, T.A. and A.B. Fuertes, *Supported carbon molecular sieve membranes based on a phenolic resin.* Journal of membrane science, 1999. **160**(2): p. 201-211.
113. Shusen, W., Z. Meiyun, and W. Zhizhong, *Asymmetric molecular sieve carbon membranes.* Journal of membrane science, 1996. **109**(2): p. 267-270.
114. Shiflett, M.B. and H.C. Foley, *Ultrasonic deposition of high-selectivity nanoporous carbon membranes.* Science, 1999. **285**(5435): p. 1902-1905.
115. Acharya, M. and H.C. Foley, *Spray-coating of nanoporous carbon membranes for air separation.* Journal of membrane science, 1999. **161**(1-2): p. 1-5.
116. Centeno, T.A. and A.B. Fuertes, *Carbon molecular sieve gas separation membranes based on poly (vinylidene chloride-co-vinyl chloride).* Carbon, 2000. **38**(7): p. 1067-1073.
117. Koresh, J.E. and A. Sofer, *Molecular sieve carbon permselective membrane. Part I. Presentation of a new device for gas mixture separation.* Separation Science and Technology, 1983. **18**(8): p. 723-734.
118. Seong, J.G., et al., *Polybenzimidazole-derived carbon molecular sieve hollow fiber membranes with tailored oxygen selective transport.* Carbon, 2022. **192**: p. 71-83.
119. Jones, C.W. and W.J. Koros, *Carbon molecular sieve gas separation membranes-I. Preparation and characterization based on polyimide precursors.* Carbon, 1994. **32**(8): p. 1419-1425.
120. Rahmani, M., et al., *Fabrication and characterization of brominated matrimid® 5218 membranes for CO2/CH4 separation: application of response surface methodology (RSM).* 2016. **16**(6): p. 481-492.
121. Plummer, C., et al., *Mild Halogenation of Polyolefins Using an N-Haloamide Reagent.* Polymer Chemistry, 2018. **9**.

122. Kim, Y.K., et al., *The gas separation properties of carbon molecular sieve membranes derived from polyimides having carboxylic acid groups.* Journal of membrane science, 2004. **235**(1-2): p. 139-146.
123. Park, H.B., et al., *Relationship between chemical structure of aromatic polyimides and gas permeation properties of their carbon molecular sieve membranes.* Journal of Membrane Science, 2004. **229**(1-2): p. 117-127.
124. Kiyono, M., P.J. Williams, and W.J. Koros, *Effect of polymer precursors on carbon molecular sieve structure and separation performance properties.* Carbon, 2010. **48**(15): p. 4432-4441.
125. Tin, P.S., et al., *Novel approaches to fabricate carbon molecular sieve membranes based on chemical modified and solvent treated polyimides.* Microporous and mesoporous materials, 2004. **73**(3): p. 151-160.
126. Tin, P.S., T.-S. Chung, and A.J. Hill, *Advanced fabrication of carbon molecular sieve membranes by nonsolvent pretreatment of precursor polymers.* Industrial & engineering chemistry research, 2004. **43**(20): p. 6476-6483.
127. Xiao, Y., et al., *Effects of brominating Matrimid polyimide on the physical and gas transport properties of derived carbon membranes.* Macromolecules, 2005. **38**(24): p. 10042-10049.
128. Kim, Y.K., H.B. Park, and Y.M. Lee, *Carbon molecular sieve membranes derived from metal-substituted sulfonated polyimide and their gas separation properties.* Journal of Membrane Science, 2003. **226**(1-2): p. 145-158.
129. Islam, M.N., et al., *Preparation and gas separation performance of flexible pyrolytic membranes by low-temperature pyrolysis of sulfonated polyimides.* Journal of membrane science, 2005. **261**(1-2): p. 17-26.
130. Geiszler, V.C. and W.J. Koros, *Effects of polyimide pyrolysis conditions on carbon molecular sieve membrane properties.* Industrial & engineering chemistry research, 1996. **35**(9): p. 2999-3003.
131. Tanihara, N., et al., *Gas permeation properties of asymmetric carbon hollow fiber membranes prepared from asymmetric polyimide hollow fiber.* Journal of membrane science, 1999. **160**(2): p. 179-186.
132. Rungta, M., L. Xu, and W.J. Koros, *Structure–performance characterization for carbon molecular sieve membranes using molecular scale gas probes.* Carbon, 2015. **85**: p. 429-442.
133. Steel, K.M. and W.J. Koros, *An investigation of the effects of pyrolysis parameters on gas separation properties of carbon materials.* Carbon, 2005. **43**(9): p. 1843-1856.
134. Petersen, J., M. Matsuda, and K. Haraya, *Capillary carbon molecular sieve membranes derived from Kapton for high temperature gas separation.* Journal of membrane science, 1997. **131**(1-2): p. 85-94.
135. Kiyono, M., P.J. Williams, and W.J. Koros, *Effect of pyrolysis atmosphere on separation performance of carbon molecular sieve membranes.* Journal of Membrane Science, 2010. **359**(1-2): p. 2-10.
136. Kiyono, M., P.J. Williams, and W.J. Koros, *Generalization of effect of oxygen exposure on formation and performance of carbon molecular sieve membranes.* Carbon, 2010. **48**(15): p. 4442-4449.

137. Soffer, A., et al., *Method of improving the selectivity of carbon membranes by chemical carbon vapor deposition*. 1997, Google Patents.
138. Abraham Soffer, J.E.K., Shlomo Saggy, *Separation device*, U.S. Patent, Editor. 1985.
139. Yoshimune, M. and K. Haraya, *Simple control of the pore structures and gas separation performances of carbon hollow fiber membranes by chemical vapor deposition of propylene.* Separation and Purification Technology, 2019. **223**: p. 162-167.
140. Jones, C.W. and W.J. Koros, *Carbon composite membranes: a solution to adverse humidity effects.* Industrial & engineering chemistry research, 1995. **34**(1): p. 164-167.
141. Koros, W.J. and G. Fleming, *Membrane-based gas separation.* Journal of membrane science, 1993. **83**(1): p. 1-80.
142. Sanyal, O., et al., *A Self‐Consistent Model for Sorption and Transport in Polyimide‐Derived Carbon Molecular Sieve Gas Separation Membranes.* Angewandte Chemie, 2020. **132**(46): p. 20523-20527.
143. Williams, P.J. and W.J. Koros, *Gas separation by carbon membranes.* Advanced membrane technology and applications, 2008: p. 599-631.
144. Rungta, M., *Carbon molecular sieve dense film membranes for ethylene/ethane separations*. 2012, Georgia Institute of Technology.
145. Haring, M.M., *The theory of rate processes (glasstone, samuel; laidler, Keith J.; Eyring, Henry)*. 1942, ACS Publications.
146. Singh-Ghosal, A. and W. Koros, *Energetic and entropic contributions to mobility selectivity in glassy polymers for gas separation membranes.* Industrial & engineering chemistry research, 1999. **38**(10): p. 3647-3654.
147. Clausi, D.T. and W.J. Koros, *Formation of defect-free polyimide hollow fiber membranes for gas separations.* Journal of Membrane Science, 2000. **167**(1): p. 79-89.
148. McKelvey, S.A., D.T. Clausi, and W.J. Koros, *A guide to establishing hollow fiber macroscopic properties for membrane applications.* Journal of membrane science, 1997. **124**(2): p. 223-232.
149. Liu, L., D. Liu, and C. Zhang, *High-temperature hydrogen/propane separations in asymmetric carbon molecular sieve hollow fiber membranes.* Journal of Membrane Science, 2022. **642**: p. 119978.
150. Omole, I.C., S.J. Miller, and W.J. Koros, *Increased molecular weight of a cross-linkable polyimide for spinning plasticization resistant hollow fiber membranes.* Macromolecules, 2008. **41**(17): p. 6367-6375.
151. Kosuri, M.R. and W.J. Koros, *Defect-free asymmetric hollow fiber membranes from Torlon®, a polyamide–imide polymer, for high-pressure CO2 separations.* Journal of Membrane Science, 2008. **320**(1-2): p. 65-72.
152. Chen, C.-C., *Thermally crosslinked polyimide hollow fiber membranes for natural gas purification*. Vol. 74. 2011.
153. Clausi, D.T., *Formation and characterization of asymmetric polyimide hollow fiber membranes for gas separations*. 1998: The University of Texas at Austin.
154. Hauner, I.M., et al., *The dynamic surface tension of water.* The journal of physical chemistry letters, 2017. **8**(7): p. 1599-1603.

155. Carruthers, S.B., G.L. Ramos, and W.J. Koros, *Morphology of integral‐skin layers in hollow‐fiber gas‐separation membranes.* Journal of applied polymer science, 2003. **90**(2): p. 399-411.
156. Clausi, D.T., S.A. McKelvey, and W.J. Koros, *Characterization of substructure resistance in asymmetric gas separation membranes.* Journal of membrane science, 1999. **160**(1): p. 51-64.
157. Burns, R.L. and W.J. Koros, *Defining the challenges for C3H6/C3H8 separation using polymeric membranes.* Journal of Membrane Science, 2003. **211**(2): p. 299-309.
158. Zhang, C., et al., *High performance ZIF-8/6FDA-DAM mixed matrix membrane for propylene/propane separations.* Journal of Membrane Science, 2012. **389**: p. 34-42.
159. Chen, C.-C., et al., *Plasticization-resistant hollow fiber membranes for CO2/CH4 separation based on a thermally crosslinkable polyimide.* Journal of membrane science, 2011. **382**(1-2): p. 212-221.
160. Xu, L., et al., *Formation of defect-free 6FDA-DAM asymmetric hollow fiber membranes for gas separations.* Journal of Membrane Science, 2014. **459**: p. 223-232.
161. Motagamwala, A.H., et al., *Stable and selective catalysts for propane dehydrogenation operating at thermodynamic limit.* Science, 2021. **373**(6551): p. 217-222.
162. Murphy, R., *Introduction to Chemical Processes*. 2022: McGraw-Hill US Higher Ed USE.
163. Rungta, M., *Ph.D. Dissertation*. 2012, Georgia Institute of Technology.
164. Lu, C.-y., et al., *Gas products and carbon deposition kinetics in chemical vapor deposition from propylene.* New Carbon Materials, 2010. **25**(1): p. 35-40.
165. Haider, S., et al., *CO2 separation with carbon membranes in high pressure and elevated temperature applications.* Separation and Purification Technology, 2018. **190**: p. 177-189.
166. Zhou, J., et al., *Regeneration of catalysts deactivated by coke deposition: A review.* Chinese Journal of Catalysis, 2020. **41**(7): p. 1048-1061.
167. Qiu, W., et al., *Hyperaging Tuning of a Carbon Molecular‐Sieve Hollow Fiber Membrane with Extraordinary Gas‐Separation Performance and Stability.* Angewandte Chemie International Edition, 2019. **58**(34): p. 11700-11703.
168. Kim, S.-J., et al., *One-Step Synthesis of Zeolite Membranes Containing Catalytic Metal Nanoclusters.* ACS Applied Materials & Interfaces, 2016. **8**(37): p. 24671-24681.
169. Wang, Z., et al., *High H2 permeable SAPO-34 hollow fiber membrane for high temperature propane dehydrogenation application.* AIChE Journal, 2020. **66**(9): p. e16278.
170. Ishii, K., et al., *Development of Silica Membranes to Improve Dehydration Reactions.* Journal of the Japan Petroleum Institute, 2019. **62**(5): p. 211-219.
171. Lu Liu, A.B., Sichao Cheng, Borja Hernandez Blazquez, Ying Pan, Yuying Shu, Dat T. Tran, Yuqing Luo, Marianthi Ierapetritou, Chen Zhang, Dongxia

Liu, *Propane Dehydrogenation in Scalable and Electrifiable Carbon Membrane Reactor. Under review.*
172. Pan, Y., et al., *Titanium silicalite-1 nanosheet-supported platinum for non-oxidative ethane dehydrogenation.* ACS Catalysis, 2021. **11**(15): p. 9970-9985.
173. Del Campo, P., C. Martínez, and A. Corma, *Activation and conversion of alkanes in the confined space of zeolite-type materials.* Chemical Society Reviews, 2021. **50**(15): p. 8511-8595.
174. Sun, Q., et al., *Subnanometer bimetallic platinum–zinc clusters in zeolites for propane dehydrogenation.* Angewandte Chemie, 2020. **132**(44): p. 19618-19627.
175. Rostami, R.B., et al., *Study of coke deposition phenomena on the SAPO_34 catalyst and its effects on light olefin selectivity during the methanol to olefin reaction.* RSC advances, 2015. **5**(100): p. 81965-81980.
176. Medrano, J., et al., *Two-zone fluidized bed reactor (TZFBR) with palladium membrane for catalytic propane dehydrogenation: Experimental performance assessment.* Industrial & Engineering Chemistry Research, 2013. **52**(10): p. 3723-3731.
177. Gómez-Quero, S., et al., *Kinetics of propane dehydrogenation over Pt–Sn/Al 2 O 3.* Catalysis Science & Technology, 2013. **3**(4): p. 962-971.
178. Li, Q., et al., *Kinetics of propane dehydrogenation over Pt–Sn/Al2O3 catalyst.* Applied Catalysis A: General, 2011. **398**(1-2): p. 18-26.
179. Sheintuch, M., et al., *Propane dehydrogenation kinetics on supported Pt catalyst.* Applied Catalysis A: General, 2016. **516**: p. 17-29.
180. Resasco, D.E. and G.L. Haller, *Catalytic dehydrogenation of lower alkanes.* 1994.
181. Rahimpour, M., et al., *Palladium membranes applications in reaction systems for hydrogen separation and purification: A review.* Chemical Engineering and Processing: Process Intensification, 2017. **121**: p. 24-49.
182. Second, C.R., et al., *Handbook of heterogeneous catalysis*. 2008.
183. Algieri, C., et al., *Catalytic membrane reactors: The industrial applications perspective.* Catalysts, 2021. **11**(6): p. 691.
184. Genti, G., et al., *Tubular inorganic catalytic membrane reactors: advantages and performance in multiphase hydrogenation reactions.* Catal. Today, 2003. **79**: p. 139.
185. Julbe, A., D. Farrusseng, and C. Guizard, *Porous ceramic membranes for catalytic reactors—overview and new ideas.* Journal of Membrane Science, 2001. **181**(1): p. 3-20.
186. Zaspalis, V., et al., *Reactions of methanol over catalytically active alumina membranes.* Applied catalysis, 1991. **74**(2): p. 205-222.
187. Quicker, P., V. Höllein, and R. Dittmeyer, *Catalytic dehydrogenation of hydrocarbons in palladium composite membrane reactors.* Catalysis today, 2000. **56**(1-3): p. 21-34.
188. Wolfrath, O., L. Kiwi-Minsker, and A. Renken, *Novel membrane reactor with filamentous catalytic bed for propane dehydrogenation.* Industrial & engineering chemistry research, 2001. **40**(23): p. 5234-5239.

189. Kiwi-Minsker, L., O. Wolfrath, and A. Renken, *Membrane reactor microstructured by filamentous catalyst.* Chemical engineering science, 2002. **57**(22-23): p. 4947-4953.
190. Chang, J.-S., et al., *Propane dehydrogenation over a hydrogen permselective membrane reactor.* Bulletin of the Korean Chemical Society, 2002. **23**(5): p. 674-678.
191. Didenko, L., et al., *Dehydrogenation of propane in a combined membrane reactor with hydrogen-permeable palladium module.* Petroleum Chemistry, 2013. **53**(1): p. 27-32.
192. Medrano, J.-A., et al., *Pd-Ag membrane coupled to a two-zone fluidized bed reactor (TZFBR) for propane dehydrogenation on a Pt-Sn/MgAl2O4 catalyst.* Membranes, 2013. **3**(2): p. 69-86.
193. Schäfer, R., et al., *Development of a H2-selective SiO2-membrane for the catalytic dehydrogenation of propane.* Separation and purification technology, 2001. **25**(1-3): p. 3-9.
194. Bobrov, V.S., N.G. Digurov, and V.V. Skudin, *Propane dehydrogenation using catalytic membrane.* Journal of membrane science, 2005. **253**(1-2): p. 233-242.
195. Amer, J., M. Burgard, and B. Ernst. *High resistance to coking of a hydrogen selective nickel membrane implemented in a membrane reactor for the catalytic dehydrogenation of propane*. in *ICCMR 9-9th international conference on catalysis in membrane reactors (Lyon, 28 June-2 July 2009, abstracts)*. 2009.